CROSSROADS AND TERMINATIONS IN TRANSURANIUM CHEMISTRY

Except where reference is made to the work of others, the work described in this dissertation is my own or was done in collaboration with my advisory committee. This dissertation does not include proprietary or classified information.

`

_____

Travis Henry Bray

Certificate of Approval:

_____	_____
Anne E. V. Gorden Assistant Professor Chemistry and Biochemistry	Thomas E. Albrecht-Schmitt, Chair Professor Chemistry and Biochemistry
_____	_____
Orlando E. Acevedo Assistant Professor Chemistry and Biochemistry	David M. Stanbury Professor Chemistry and Biochemistry

_____

George T. Flowers
Interim Dean
Graduate School

CROSSROADS AND TERMINATIONS IN TRANSURANIUM CHEMISTRY

Travis Henry Bray

A Dissertation

Submitted to

the Graduate Faculty of

Auburn University

in Partial Fulfillment of the

Requirements for the

Degree of

Doctor of Philosophy

Auburn, Alabama
August 9, 2008

CROSSROADS AND TERMINATIONS IN TRANSURANIUM CHEMISTRY

Travis Henry Bray

Permission is granted to Auburn University to make copies of this dissertation at its discretion, upon request of individuals or institutions and at their expense. The author reserves all publication rights.

_____
Signature of Author

_____
Date of Graduation

VITA

Travis Henry Bray, born Joseph Travis Brown, son of Wallace E. Brown and Wanda M. (Bray) Hall, was born September 6, 1977, in Valdosta, Georgia. He graduated from Lowndes High School in 1995 and then attended Valdosta State University for five and a half years, where he graduated with the Outstanding Chemistry Senior Award in December 2000. After a three and a half year scholastic break, wherein he taught general science at Valdosta High School for one year, he entered Graduate School at Auburn University pursuing a doctoral degree in Chemistry.

DISSERTATION ABSTRACT

CROSSROADS AND TERMINATIONS IN TRANSURANIUM CHEMISTRY

Travis Henry Bray

Doctor of Philosophy, August 9, 2008
(B.S., Valdosta State University, 2000)

165 Typed Pages

Directed by Thomas E. Albrecht-Schmitt

The focus of this dissertation is published results from my doctoral research at Auburn University, the scope of which is multifaceted. The first topic covers recent research devoted to developing a better understanding of the structural diversity and related physical properties of early actinide compounds containing either selenite or iodate. These studies are primarily driven by the presence of ^{79}Se ($t_{1/2}$ = 1.1 x 10^6) and ^{129}I ($t_{1/2}$ = 1.7 x 10^7), both of which are long-lived β^- emitting isotopes produced through the fission of ^{235}U, in spent nuclear fuels. From the redox chemistry of selenium one would predict that it will exist as either the selenate (SeO_4^{2-}) or the selenite (SeO_3^{2-})

anion, while iodine is expected to be present as either the iodide anion, I^-, or the iodate oxoanion (IO_3^-). The subject of my second research focus, phosphonates have been of special interest with regards to *f* – element chemistry as a result of their use in separations. Structural studies of these systems with transuranium elements have been limited due to the difficulties faced when working with these radioactive metals and their insolubility and tendency to form powders or microcrystalline precipitates. Topics include the structure-property relationships for the following published compounds or, in the case chapter 6, compound submitted for publication: $Na_2[UO_2(IO_3)_4(H_2O)]$ (Ch. 2: Bray, T. H.; et al., *Inorg. Chem.*, 2006, *45*, 8251-8257.), $An(IO_3)_4$ (An = Np, Pu) and $Np(IO_3)_4 \cdot nH_2O$ (Ch. 3: Bray, T. H.; et al., *Inorg. Chem.*, 2007, *46*, 3663-3668.), $Pu(SeO_3)_2$ (Ch. 4: Bray, T. H.; et al., *J. Solid State Chem.*, 2008, *181*, 493-498.), $NpFPO_4$ and $Cs_2Np_2F_7PO_4$ (Ch. 5: Bray, T. H.; et al., *J. Solid State Chem.*, 2007, *180*, 70-74.), $[C_6H_{14}N_2][(UO_2)_4(HPO_4)_2PO_4)_2(H_2O)] \cdot H_2O$ (Ch. 6: Bray, T. H.; et al., "Synthesis and Structure of $[C_6H_{14}N_2][(UO_2)_4(HPO_4)_2(PO_4)_2(H_2O)] \cdot H_2O$: An Expanded Open-Framework Amine-Bearing Uranyl Phosphate," In press: *Journal of Solid State Chemistry* April 24, 2008.), and $Np(CH_3PO_3)(CH_3PO_3H)(NO_3)(H_2O) \cdot H_2O$ (Ch. 7: Bray, T. H.; et al., *Inorg. Chem.*, 2007, *46*, 10959-10961.)

ACKNOWLEDGMENTS

There are many people that have been invaluable throughout my academic career, both undergraduate and graduate, and the time between. Mom, Dad, Granny, Grandad, without the faith you had in me, the encouragement you gave me, and the patience you maintained, I would have never made it to this point. Thanks to the friends I have made along the way helping me maintain a sense of sanity through the last four years. Dr. Gosnell, Dr. Manning, and Dr. Spencer, you knew early on that I would enjoy research and be successful in graduate school. Dr. Webb, your crystallography classes, as well as your seemingly endless chemistry knowledge in general, were a true asset. I'd like to thank the Departmental office and supply store staffs for making me feel welcome and always taking every extra effort to facilitate any task I had at hand. Jin, your great work ethic and devotion to your research was a source of inspiration. Shehee, your advice, mechanical expertise, and general guidance were nothing short of brotherly. And finally, to the person I owe the most to…Boss, I'm truly lucky to have had you, not only as my advisor, but as a friend. I appreciate everything you've done for me and my career.

I'd like to acknowledge the DOE, the NSF, and the Malone-Zallen and Merriwether Fellowships for their funding and contributions, as well as the long list of collaborators, Eun Sang Choi, James S. Brooks, James V. Beitz, Richard E. Sykora, Richard G. Haire, S. Skanthakumar, Lynne Soderholm, and Amanda C. Bean for their work and efforts.

Style manual or journal used:

American Chemical Society style

Computer software used:

Microsoft Office Word, Excel, and Powerpoint 2003, Atoms V6.2, SHELXTL PC,

Version 6.12

TABLE OF CONTENTS

LIST OF FIGURES xiv

LIST OF TABLES xviii

CHAPTER 1 INTRODUCTION 1

Phosphorus, Iodine, and Selenium in Actinide Chemistry 2

Solid State Chemistry of Phosphonates, Iodate, and Selenite 2

Uranium-Phosphorus Background.....5

Uranium-Selenium and Uranium-Iodine Background.....6

Redox and Structural Chemistry of Uranium, Neptunium, and Plutonium.....12

Hydrothermal Chemistry 14

Magnetic Susceptibility 16

CHAPTER 2 THE FIRST MOLECULAR URANYL IODATE, $Na_2[UO_2(IO_3)_4(H_2O)]$: STRUCTURAL POLARITY INDUCED BY COOPERATIVE HYDROGEN BONDING AND LONE-PAIR ALIGNMENT.....21

Abstract.....21

Introduction.....22

Experimental.....23

General Information.....23

$Na_2[UO_2(IO_3)_4(H_2O)]$ Synthesis (Method 1).....23

$Na_2[UO_2(IO_3)_4(H_2O)]$ Synthesis (Method 2).....24

Crystallographic Studies.....24

Nonlinear Optical Measurements.....26

Thermal Analysis.....28

Powder X-ray Diffraction.....28

Results and Discussion.....29

Structural Features of $Na_2[UO_2(IO_3)_4(H_2O)]$.....29

Structural-Property Relationships in $Na_2[UO_2(IO_3)_4(H_2O)]$.....36

Thermal Behavior.....39

References.....42

CHAPTER 3 CRITICAL ROLE OF WATER CONTENT IN THE FORMATION AND REACTIVITY OF URANIUM, NEPTUNIUM, AND PLUTONIUM IODATES UNDER HYDROTHERMAL CONDITIONS: IMPLICATIONS FOR THE OXIDATIVE DISSOLUTION OF SPENT NUCLEAR FUEL.....47

Abstract 47

Introduction.....48

Experimental.....49

General Information.....49

Actinide Iodate Synthesis.....49

Crystallographic Studies.....50

Magnetic Susceptibility Measurements.....50

Nonlinear Optical Measurements.....52

Results and Discussion.....52

Reactions.....52

Structure of $An(IO_3)_4$ (An = Np AND Pu).....57

Structure of $Np(IO_3)_4 \cdot nH_2O \cdot nHIO_3$.....57

Magnetic Properties of $Np(IO_3)_4$ 61

References....63

CHAPTER 4 HYDROTHERMAL SYNTHESIS, STRUCTURE, AND MAGNETIC PROPERTIES OF $Pu(SeO_3)_2$....66

Abstract....66

References....66

Experimental....68

General Information....68

$Pu(SeO_3)_2$ Synthesis....68

Crystallographic Studies....68

Magnetic Studies....69

Results and Discussion....72

Synthesis....72

Structural Features of $Pu(SeO_3)_2$....73

Magnetism....73

References....81

CHAPTER 5 PRODUCT EVOLUTION IN THE Np(IV) FLUOROPHOSPHATE SYSTEM....84

Abstract....84

Introduction....85

Experimental....86

General Information....86

$NpFPO_4$ and $Cs_2Np_2F_7PO_4$ Syntheses....86

Crystallographic Studies....87

UV-VIS-NIR Spectroscopy.....91
Results and Discussion.....91
Synthesis.....91
Structure of $NpFPO_4$.....92
Structure of $Cs_2Np_2F_7PO_4$.....96
References.....101
CHAPTER 6 SYNTHESIS AND STRUCTURE OF $[C_6H_{14}N_2][(UO_2)_4(HPO_4)_2PO_4)_2(H_2O)]\cdot H_2O$: AN EXPANDED OPEN-FRAMEWORK AMINE-BEARING URANYL PHOSPHATE.....104
Abstract.....104
Introduction.....105
Experimental.....106
General Information.....106
$[C_6H_{14}N_2][(UO_2)_4(HPO_4)_2PO_4)_2(H_2O)]\cdot H_2O$ (DUP-1) Synthesis.....106
Elemental Analysis.....107
Vibrational Spectroscopy.....107
Crystallographic Studies.....107
Thermal Synthesis.....108
Powder X-ray Diffraction.....108
Results and Discussion.....110
Structure of $[C_6H_{14}N_2][(UO_2)_4(HPO_4)_2PO_4)_2(H_2O)]\cdot H_2O$.....110
Thermal Behavior.....119
References.....120

CHAPTER 7 *IN SITU* HYDROTHERMAL REDUCTION OF Np(VI) AS A ROUTE TO Np(IV) PHOSPHONATES 123

Abstract 123

Introduction 123

Experimental 126

General Information 126

$Np(CH_3PO_3)(CH_3PO_3H)(NO_3)(H_2O)\cdot H_2O$ (NpMeP-1) Synthesis 126

$NpO_2(CH_3PO_3)$ (NpMeP-2) Synthesis 127

Crystallographic Studies 127

Magnetic Susceptibility Measurements 128

Results and Discussion 128

Structural Features of $Np(CH_3PO_3)(CH_3PO_3H)(NO_3)(H_2O)\cdot H_2O$ 128

Magnetic Properties of $Np(CH_3PO_3)(CH_3PO_3H)(NO_3)(H_2O)\cdot H_2O$ 135

References 139

CHAPTER 8 SUMMARY 140

LIST OF FIGURES

Figure 1.1 Congruent local pseudo-tetrahedral geometries of phosphonates, iodate, and selenite.....3

Figure 1.2 Potential binding modes of SeO_3^{2-}, IO_3^-, and RPO_3^{2-} to metal centers.....4

Figure 1.3 Pictures of selected uranyl phosphate minerals.....4

Figure 1.4 Fission yields for the fission of ^{235}Uranium by neutrons of various energies: —, thermal neutrons, - - - -, neutrons produced by fission, · · · ·, 14 MeV neutrons.....7

Figure 1.5 Pictures of uranyl selenite minerals.....8

Figure 1.6 Latimer diagram of neptunium.....13

Figure 1.7 Latimer diagram of plutonium.....13

Figure 1.8 Components of autoclave used for hydrothermal synthesis shown as (a) components, (b) a cartoon depiction, and (c) an assembled unit.....15

Figure 2.1 View of the structure of the $[UO_2(IO_3)_4(H_2O)]^{2-}$ anion in $Na_2[UO_2(IO_3)_4(H_2O)]$, which has imposed 2-fold symmetry. 50% probability ellipsoids are depicted.....31

Figure 2.2. Illustration of $[UO_2(IO_3)_4(H_2O)]$ units found in $UO_2(IO_3)_2(H_2O)$.....33

Figure 2.3. Depiction of the one-dimensional chains of $[UO_2(IO_3)_4(H_2O)]^{2-}$ anions formed through intermolecular hydrogen bonds between the coordinating water molecule and oxo atoms of iodate from adjacent anions. The dashed lines between iodate anions within individual $[UO_2(IO_3)_4(H_2O)]^{2-}$ anions indicate iodate···iodate interactions that orient the iodate anions along the *b* axis. Cooperative interactions are present for aligning different groups the structure of $Na_2[UO_2(IO_3)_4(H_2O)]$, where the hydrogen bonding, intermolecular iodate···iodate interactions, and the lone-pair alignment contribute to the short-range and long-range polarity.....34

Figure 2.4. (a) View of the distorted dodecahedral environment around Na(1) and (b) the distorted octahedral environment around Na(2) in $Na_2[UO_2(IO_3)_4(H_2O)]$. The environments around the Na^+ cations are consistent with a polar structure 36

Figure 2.5. Packing diagram for $Na_2[UO_2(IO_3)_4(H_2O)]$.....38

Figure 2.6 DSC and TGA thermograms of $Na_2[UO_2(IO_3)_4(H_2O)]$ 41

Figure 3.1. Photograph showing the hydrothermal reduction of the neptunium(VI) iodate $NpO_2(IO_3)_2(H_2O)$ to the neptunium(IV) iodates $Np(IO_3)_4$ and $Np(IO_3)_4{\cdot}nH_2O{\cdot}nHIO_3$ 55

Figure 3.2. (a) View of the one-dimensional chains in $An(IO_3)_4$ (An = Np, Pu) consisting of eight-coordinate, dodecahedral An(IV) centers bridged by iodate. (b) Depiction of the pinwheel packing of the $An(IO_3)_4$ chains.....58

Figure 3.3. Depiction of the structure of $Np(IO_3)_4{\cdot}nH_2O{\cdot}nHIO_3$. This structure consists of a three-dimensional network constructed from nine coordinate tricapped trigonal prismatic Np(IV) that are bridged by iodate anions to create the channels that extend along the *c* axis. The channels are partially filled by iodate anions or water molecules 59

Figure 3.4. Temperature dependence of the inverse magnetic susceptibility of a $Np(IO_3)_4$ single crystal. The Curie-Weiss fitting curve is shown as a solid line.....63

Figure 4.1. View of the one-dimensional chains of edge-sharing PuO_8 dodecahedra that extend down the *a* axis in the structure of $Pu(SeO_3)_2$. 75

Figure 4.2. Depiction of the three-dimensional structure of $Pu(SeO_3)_2$ formed from the interconnection of one-dimensional chains of edge-sharing PuO_8 dodecahedra by selenite anions.....75

Figure 4.3. The magnetic susceptibility of $Pu(SeO_3)_2$ as a function of temperature obtained by subtracting the magnetization measured under an applied field of 2000 Oe from the contribution under a field of 5000 Oe (see text). Temperature dependence at low temperature is not consistent with simple magnetic ordering. Inset shows the same data plotted assuming Curie-Weiss behavior. The solid line, extending over the temperature range of 35 – 300 K, represents the best fit to the data (see text). Low temperature deviation from linearity is consistent with the influence of magnetic correlations.....78

Figure 5.1. View of the fundamental building units in $NpFPO_4$ that consist of Np(IV) centers bound by both fluoride and phosphate to yield $[NpF_2O_6]$ distorted dodecahedra. [50% probability ellipsoids are depicted.] 94

Figure 5.2. Depiction of the tightly-packed structure of $NpFPO_4$. $[NpF_2O_6]$ distorted dodecahedra are shown in blue, phosphate anions in yellow, oxygen atoms are red, and fluoride anions in green.....95

Figure 5.3. View of the fundamental building units in $Cs_2Np_2F_7PO_4$. Np(1) is present in a distorted dodecahedral environment, and Np(2) in tricapped trigonal prismatic environment. [50% probability ellipsoids are depicted].....98

Figure 5.4. Illustration of the $[NpO_2F_6]$ distorted dodecahedra (dark blue) and $[NpO_2F_7]$ tricapped trigonal prisms (light blue), PO_4^{3-} (yellow), and F^- anions (green) that form the structure of $Cs_2Np_2F_7PO_4$. 99

Figure 6.1a. ORTEP of the local environment around U(1). 50% probabilities shown.....112

Figure 6.1b. ORTEP of the local environment around U(2). 50% probabilities shown.....112

Figure 6.1c. ORTEP of the local environment around U(3). 50% probabilities shown.....113

Figure 6.1d. ORTEP of the local environment around the face-sharing U(4) and U(5) metal centers. 50% probabilities shown.....113

Figure 6.2. View of the (a) β-uranophane sheet topology found in $Ca(H_3O)_2(UO_2)_2(SiO_4)_2(H_2O)_3$ as compared to (b) the delaminated sheets of similar construction found in $[C_6H_{12}N_2H_2][(UO_2)_4(HPO_4)_2(PO_4)_2(H_2O)]\cdot H_2O$ ..114

Figure 6.3. Packing diagram of the 3-dimension channels and occluded $DABCOH_2$ and water molecules found in $[C_6H_{12}N_2H_2][(UO_2)_4(HPO_4)_2(PO_4)_2(H_2O)]\cdot H_2O$ 115

Figure 6.4. TGA and DSC thermograms of $[C_6H_{12}N_2H_2][(UO_2)_4(HPO_4)_2(PO_4)_2(H_2O)]\cdot H_2O$ 120

Figure 7.1. Views down the *b* and *a* axes of the polar, lamellar structure of NpMeP-1. Color code: NpO_8, pink; P, yellow; O, red; N, blue; H, white 135

Figure 7.2. View down the *c* axis of the layered structure of the neptunium (VI) methyl-phosphonate NpMeP-2. Color code: NpO7 pentagonal bipyramids,orange; P, yellow; O, red; H, white 137

Figure 7.3. Temperature dependence of the reciprocal molar magnetic susceptibility for NpMeP-1 under an applied magnetic field of 0.1 T between 5 and 300 K. The straight line represents the fit to the Curie-Weiss law in the range of 5-100 K 138

LIST OF TABLES

Table 1.1 Listing of Uranyl Iodates and Uranyl Selenites with Published Structures and their Dimensionality.....10

Table 1.2 Listing of Transuranium and Transplutonium Iodates and Transuranium Selenites with Characterized Structures and their Dimensionality (D) 11

Table 2.1. IR Vibrational Modes for $Na_2[UO_2(IO_3)_4(H_2O)]$ (KBr, cm^{-1}).....25

Table 2.2. Crystallographic Data for $Na_2[UO_2(IO_3)_4(H_2O)]$.....27

Table 2.3. Selected Bond Distances (Å) and Angles (^{o}) for $Na_2[UO_2(IO_3)_4(H_2O)]$ ...34

Table 3.1. Crystallographic Data for $Np(IO_3)_4$, $Pu(IO_3)_4$, and $Np(IO_3)_4{\cdot}nH_2O{\cdot}nHIO_3$.....51

Table 4.1. Crystallographic Data for $Pu(SeO_3)_2$.....71

Table 4.2. Atomic Coordinates and Equivalent Isotopic Displacement Parameters for $Pu(SeO_3)_2$ 71

Table 4.3. Selected Bond Distances (Å) and Angles (^{o}) for $Pu(SeO_3)_2$.....76

Table 5.1. Crystallographic Data for $NpFPO_4$ and $Cs_2Np_2F_7PO_4$.....89

Table 5.2. Atomic Coordinates and Equivalent Isotropic Displacement Parameters for $NpFPO_4$ 90

Table 5.3. Atomic Coordinates and Equivalent Isotropic Displacement Parameters for $Cs_2Np_2F_7PO_4$ 91

Table 5.4. Selected Bond Distances (Å) for $NpFPO_4$.....96

Table 5.5. Selected Bond Distances (Å) for $Cs_2Np_2F_7PO_4$.....101

Table 6.1. Crystallographic Data for $[C_6H_{12}N_2H_2][(UO_2)_4(HPO_4)_2(PO_4)_2(H_2O)]{\cdot}H_2O$ (DUP).....110

Table 6.2. Selected Bond Distances (Å) and Angles (^{o}) for $[C_6H_{12}N_2H_2][(UO_2)_4(HPO_4)_2(PO_4)_2(H_2O)]\cdot H_2O$ (DUP) 117

Table 7.1. Crystallographic Data for $Np(CH_3PO_3)(CH_3PO_3H)(NO_3)(H_2O)\cdot H_2O$ and $NpO_2(CH_3PO_3)$ 130

Table 7.2 Atomic Coordinates and Equivalent Isotropic Displacement Parameters for $Np(CH_3PO_3)(CH_3PO_3H)(NO_3)(H_2O)\cdot H_2O$ 131

CHAPTER 1

INTRODUCTION

With the advent of the nuclear age, essentially two topics have guided researchers in their chemical studies of the actinides. Initially, once the transuranium elements were produced, it was necessary to separate or partition them, and subsequently purify and enrich iueither the uranium or the plutonium in effort to prepare nuclear fuels for military and commercial nuclear energy. One concern resulted from the waste generated during nuclear fuel cycles and the problems faced in dealing with the long-term storage of this waste (regardless if this waste is reprocessed and reused in a subsequent fuel cycle).[1] In this regard, a fundamental understanding of the chemistry inherent to these waste systems, and the geological conditions around the eventual repositories built to house spent nuclear fuel becomes of great concern because little is know about how the actinides and fission products will interact with the waste matrices. This doctoral research has focused on a small area of this latter issue and finds application *via* the study of the solid state chemistry of actinide compounds containing iodate (IO_3^-), selenite (SeO_3^{2-}), phosphate (PO_3^{4-}), and, more recently, phosphonate (RPO_3^{2-}) anions, and the relationship their structure has to the physical properties of these compounds. The remainder of this introduction will serve to provide some background to the significance of this research and include general information about the systems studied.

PHOSPHORUS, IODINE, AND SELENIUM IN ACTINIDE CHEMISTRY

Solid State Chemistry of Phosphonates, Iodate, and Selenite. Phosphonates, iodate, and selenite all share the same basic local geometry, in which the central atom resides in a pseudo-tetrahedron with three bonding oxygen atoms around the base and one apical unit that is generally nonbonding (Figure 1.1).[2] In the case of iodate and selenite, a stereochemically active non-bonding pair of electrons caps the tetrahedron, while in phosphonates, the fourth coordination site is occupied by an alkyl group. Compounds containing selenite or iodate have been structurally studied on account of the possibility that these non-innocent electrons aligning in the solid state might yield polar compounds exhibiting non-linear optical properties. Phosphonates have the same potential to crystallize in polar space groups, but also have the ability to exchange the organic group. Although little single crystal data exists for phosphonates containing actinides, it has been shown that altering the organic group can result in a variety of structures, including 1-D tubules.[3]

The possible binding modes of these anions can be used predict the possibility of rich structural diversity and are shown in Figure 1.2. Each anion can use one, two, or all three bonding oxygens either to bridge between a metal and the central atom or as a μ^3-bridging oxygen between the central atom and two different metals. In addition, these anions can effectively chelate a metal or combine these different binding modes. As a result, complexes containing these anions can yield molecular compounds, 1-D chains or tubules, 2-D layers, or 3-D compounds.[3,4]

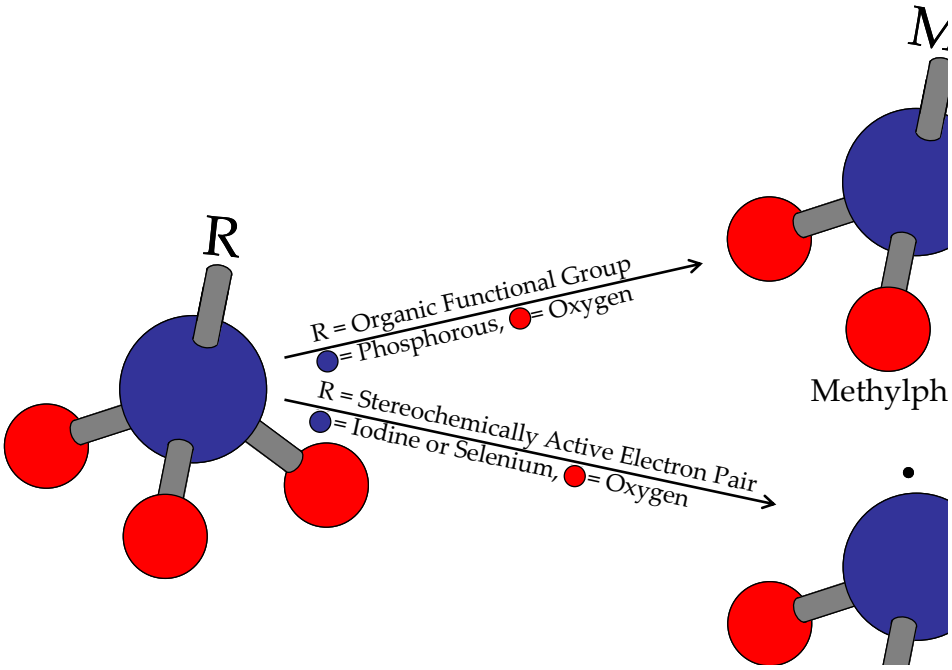

Figure 1.1. Cartoon depiction of congruent local pseudo-tetrahedral geometries of phosphonates, iodate, and selenite.[2]

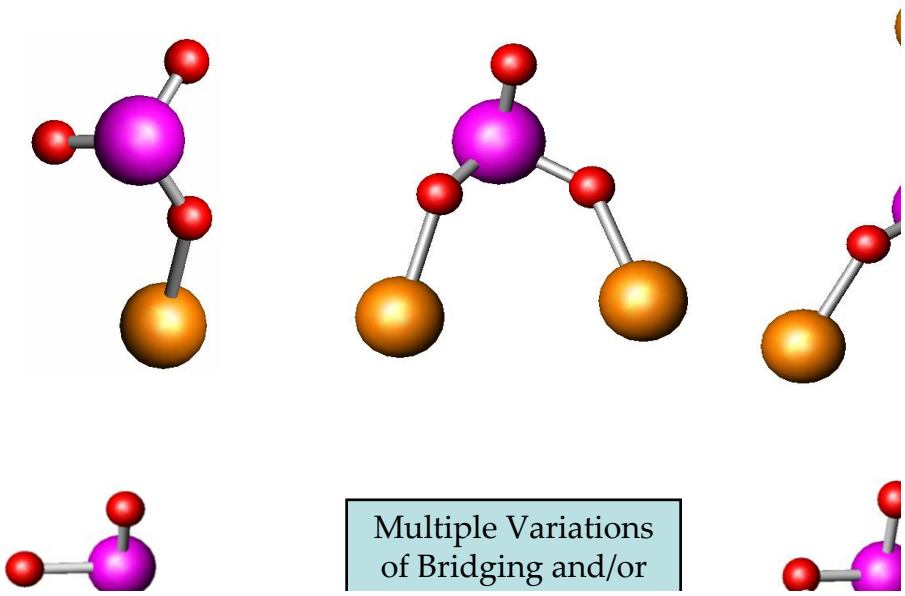

Figure 1.2. Potential binding modes of SeO_3^{2-}, IO_3^-, and RPO_3^{2-} to metal centers.[4]

Figure 1.3. Pictures of selected uranyl phosphate minerals.[5]

Uranium-Phosphorus Background. Uranium mineral-phases containing phosphate, such as autunite ($Ca(UO_2)_2(PO_4)_2 \cdot 10H_2O$), uranocircite ($Ba(UO_2)_2(PO_4)_2 \cdot 12H_2O$), tobernite ($Cu(UO_2)_2(PO_4)_2 \cdot 10H_2O$), and phosphuranylite ($KCa(H_3O)_3(UO_2)_7(PO_4)_4O_4 \cdot 8H_2O$) were being described as early as the late 19th century.[5] Figure 1.3 shows a few examples of these minerals demonstrating the fact that these uranyl phosphate mineral phases form in the presence of a variety of metals. After the discovery of elemental transmutation, scientists were faced with the problem of separating, precipitating, and thereby purifying trans-uranium elements, primarily ^{239}Pu, from bulk uranium and other fission products. While one of the first compounds precipitated after measurable quantities of plutonium were produced available was $Pu(IO_3)_4$ in 1942, it required several cycles of co-precipitating plutonium with bismuth phosphate to accomplish the initial purification.[1] Organophosphate compounds, such as phosphonates, dialkyl phosphonates, and trialkyl phosphonates were used as early as the 1950's as principle components in the recovery of uranium and thorium using solvent extraction. This is due in large part to the high stability constants of these actinide-phosphonate complexes across a wide range of pH; however, a side effect of the complexing ability of these ligands is that typically amorphous solids or microcrystalline powders precipitated rather than well-ordered single crystals. As a result, the description of the structural chemistry of these systems has been limited.[2] In fact, of the small number of proposed structures, nearly half come by way of Reitveld refinements on powder samples and not single crystal data.

Uranium-Selenium and Uranium-Iodine Background. In addition to fundamental investigations relating optical, electronic, and magnetic properties to the

structures that arise from their incorporation into actinide solid state systems, the chemistry of their central atoms is of special interest due to their potential role in the waste management of spent nuclear fuels. Among other problematic fission fragments, ^{79}Se ($t_{1/2}$ = 1.1 x 10^6) and ^{129}I ($t_{1/2}$ = 1.7 x 10^7) are two isotopes of concern because they are both long lived β^- emitters,. While these isotopes are not produced in high quantities that other metals like ^{90}Sr, ^{137}Cs, or the lanthanides are (Figure 1.4), given the large amounts of waste generated, they will certainly exist in significant quantities.[6] From the redox chemistry of selenium, it exists as either the selenate (SeO_4^{2-}) or the selenite (SeO_3^{2-}) in acidic aqueous conditions, both of which are significantly soluble. In contrast, iodine is expected to be present as either the iodide anion, I^-, or the iodate oxyanion (IO_3^-). Because of this, there is a possibility that, once cladding-failure occurs in spent nuclear fuels (SNF) storage vessels, soluble species of both the early actinides as well as, among others, iodate and selenite anions could escape and enter the surrounding environment.

Geological surveys have shown that a myriad of mineral phases form naturally inside uranium mines. Between 1963 and the present, seven uranium mineral-phases containing selenite, namely guilleminite ($Ba[(UO_2)_3(SeO_3)_2O_2](H_2O)_3$), derriksite ($Cu_4[(UO_2)(SeO_3)_2(OH)_6]$), demesaekerite ($Pb_2Cu_5[(UO_2)(SeO_3)_3]_2(OH)_6(H_2O)_2$), marthozite ($Cu[(UO_2)_3(SeO_3)_2O_2](H_2O)_8$), piretite ($Ca[(UO_2)_3(SeO_3)_2](OH)_4(H_2O)_4$), haynesite ($(UO_2)_3(OH)_2(SeO_3)_2(H_2O)_5$), and larisaite ($Na(H_3O)(UO_2)_3(SeO_3)_2O_2(H_2O)_4$) have been discovered, mostly distributed among the Musonoi and Shinkolobwe Mines in the Congo, Africa, and the Repete Mine in Utah (Figure 1.5).[5] Representatives from each

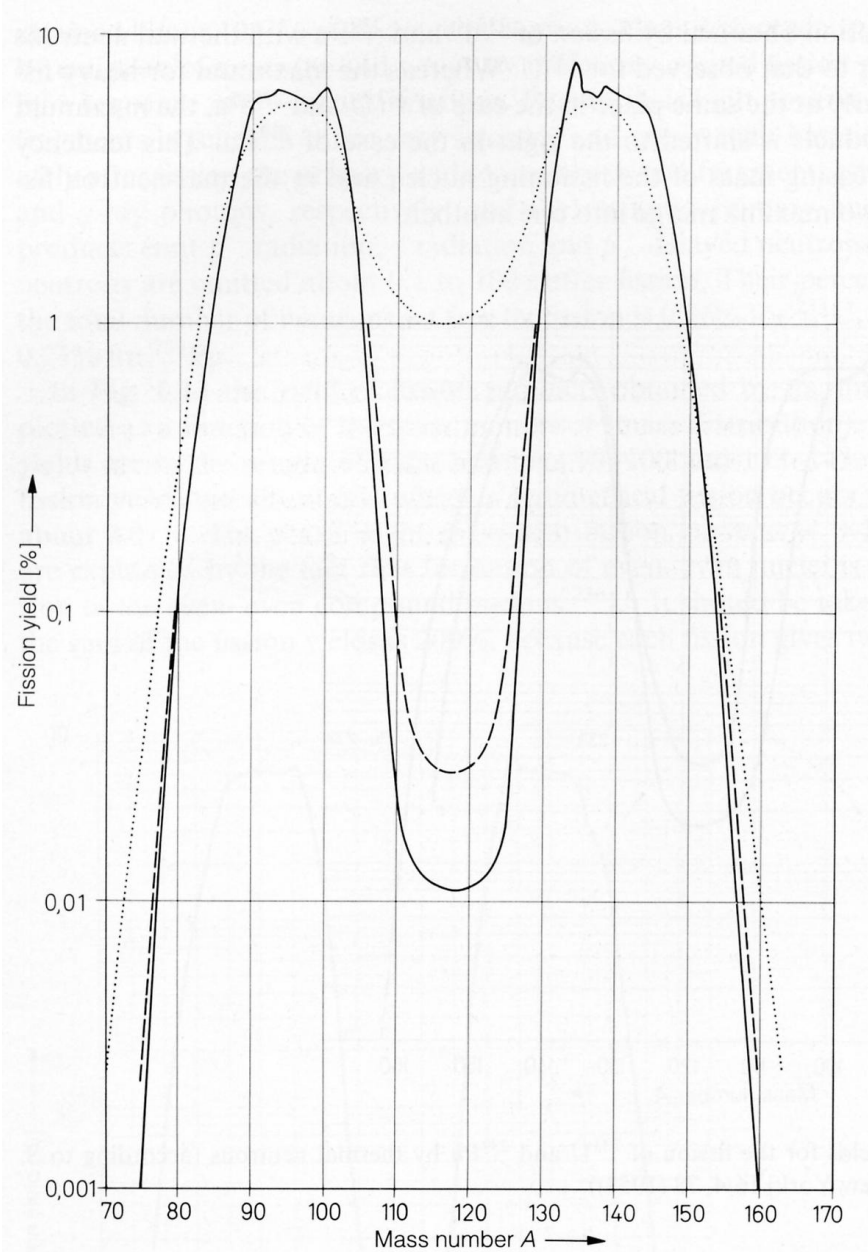

Figure 1.4. Fission yields for the fission of ^{235}uranium by neutrons of various energies: —, thermal neutrons, - - - -, neutrons produced by fission, · · · ·, 14 MeV neutrons.[6]

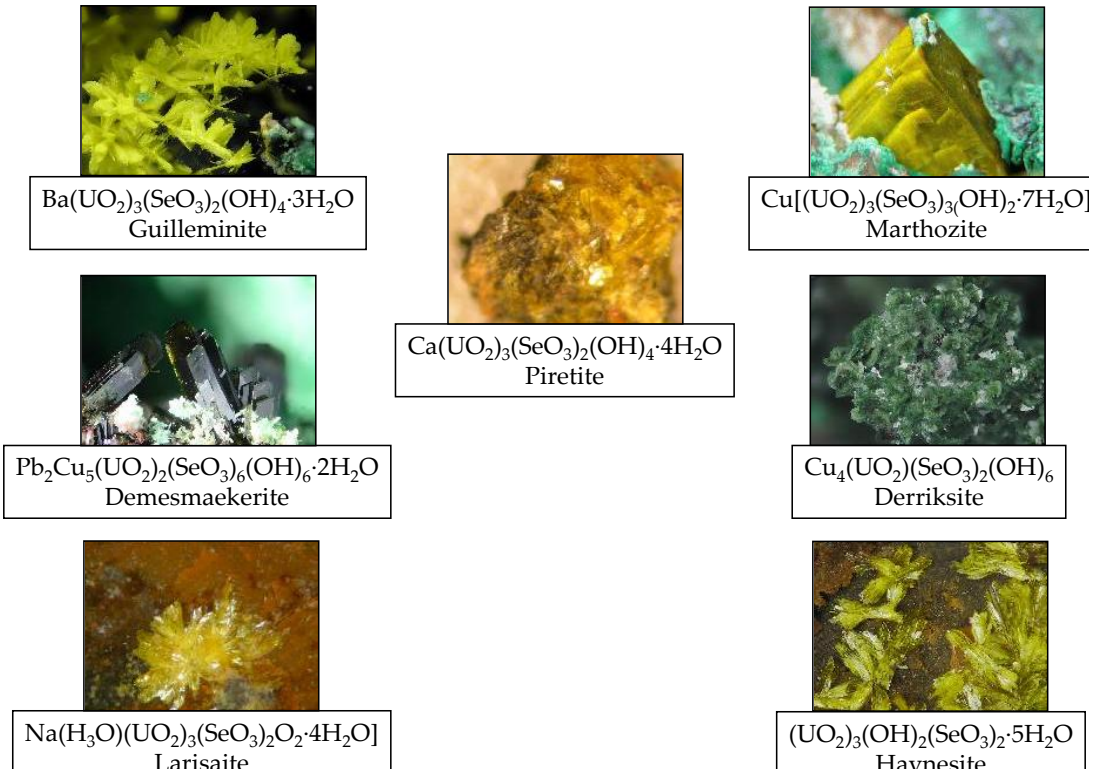

Figure 1.5. Pictures of uranyl selenite minerals.[5]

periodic group, with the exception of lanthanides, have been structurally characterized. Although no iodate mineral phases containing uranium have been discovered, based on the similar geometries of Se and I in these anions, one would expect that alteration phases of uranium and iodate would form in similar manner to the selenite minerals. For this reason, efforts have been devoted to synthesizing early actinide compounds precipitated by either selenite or iodate in the hopes of studying their physical properties and also as means to model actinide species likely to form under geological conditions. A comprehensive list of these results is shown in Table 1.1, demonstrating representatives synthesized and structurally characterized with a diverse range of countering cations.[3] These results also provide insight into a dependable and consistent method with which to extend this research to heavier actinides. Given the increased risks and scarcity of material when working with transuranium and transplutonium elements, the use of more common actinides, such as thorium and uranium, or nonradioactive elements, i.e. cerium, zirconium, and lanthanides, as surrogates for transuranic research is a common practice. Thus, a much shorter list of results has been produced for transuranium actinide selenites and iodates (Table 1.2).[8]

REDOX AND STRUCTURAL CHEMISTRY OF URANIUM, NEPTUNIUM, AND PLUTONIUM

At the present time, plans exist to make the eventual resting place of commercial spent nuclear fuel (SNF) is a repository situated deep under Yucca Mountain, approximately 100 miles east of Las Vegas, Nevada. Of great concern is that during the thousands of years these long-lived radioactive waste species might require to decay,

Table 1.1. Listing of uranyl iodates and uranyl selenites with published structures and their reference.[7]

Iodates	Ref	Selenites	Ref
$UO_2(IO_3)_2$	7a	$K[(UO_2)(HSeO_3)(SeO_3)]$	7j
$UO_2(IO_3)_2(H_2O)$	7a	$Rb[(UO_2)(HSeO_3)(SeO_3)]$	7j
$Na_2[UO_2(IO_3)_4(H_2O)]$	7b	$Cs[(UO_2)(HSeO_3)(SeO_3)]$	7j
$K[UO_2(IO_3)_3]$	7c	$Tl[(UO_2)(HSeO_3)(SeO_3)]$	7j
$K_3[(UO_2)_2(IO_3)_6](IO_3)\cdot H_2O$	7d	$Sr[(UO_2)(SeO_3)_2]\cdot 2H_2O$	7k
$K_2[(UO_2)_3(IO_3)_4O_2]$	7e,f	$Sr[(UO_2)_2(SeO_3)_2O_2]\cdot 4H_2O$	7l
$Rb_2[(UO_2)_3(IO_3)_4O_2]$	7e,f	$Ca[(UO_2)(SeO_3)_2]$	7m
$Tl_2[(UO_2)_3(IO_3)_4O_2]$	7e,f	$Sr[(UO_2)(SeO_3)_2]$	7m
$Sr[(UO_2)_2(IO_3)_2O_2]$	7e,f	$Ba[(UO_2)(SeO_3)_2]$	7m
$Ba[(UO_2)_2(IO_3)_2O_2]$	7e,f	$Ag_2[(UO_2)(SeO_3)_2]$	7j
$Pb[(UO_2)_2(IO_3)_2O_2]$	7e,f	$Pb[(UO_2)(SeO_3)_2]$	7j
$Ag_4(UO_2)_4(IO_3)_2(IO_4)_2O_2$	7g	$[C_4H_{12}N_2]_{0.5}[(UO_2)(HSeO_3)(SeO_3)]$	7n
$Rb[(UO_2)(CrO_4)(IO_3)(H_2O)]$	7h	$[C_6H_{14}N_2]_{0.5}[(UO_2)(HSeO_3)(SeO_3)]$	7n
$K_2[(UO_2)(CrO_4)(IO_3)_2]$	7h		
$Rb_2[(UO_2)(CrO_4)(IO_3)_2]$	7h		
$Cs_2[(UO_2)(CrO_4)(IO_3)_2]$	7h,i		
$K_2[(UO_2)(MoO_4)(IO_3)_2]$	7h		

Table 1.2. Listing of transuranium and transplutonium iodates and transuranium selenites with characterized structures and their reference.[8]

Iodates	**Ref**	**Selenites**	**Ref**
$Np(IO_3)_4$	8a	α – $AgNpO_2(SeO_3)$	8b
$Np(IO_3)_4 \cdot nH_2O$	8a	β – $AgNpO_2(SeO_3)$	8b
$NpO_2(IO_3)$	8b	$Pb(NpO_2)_2(SeO_3)_2$	8j
$NpO_2(IO_3)_2(H_2O)$	8c	$Np(NpO_2)_2(SeO_3)_3$	8k
$NpO_2(IO_3)_2 \cdot H_2O$	8c	$NpO_2(SeO_3)$	8j
$K[NpO_2(IO_3)_3] \cdot 1.5H_2O$	8d	$Pu(SeO_3)_2$	8l
$Pu(IO_3)_4$	8a		
$PuO_2(IO_3)_2 \cdot H_2O$	8e		
$K_3Am_3(IO_3)_{12} \cdot HIO_3$	8f		
α - $Am(IO_3)_3$	8g,h		
β - $Am(IO_3)_3$	8g		
$Cm(IO_3)_3$	8h		
$Cf(IO_3)_3$	8i		

conditions might occure that would allow for the transport and migration of not only the actinide elements remaining in the SNF, but also the resulting fission products. The first step to modeling how geological conditions surrounding Yucca Mountain Repository will either facilitate or retard actinide transport in the environment requires detailed knowledge of their aqueous chemistry. Uranium exists naturally in the +4 and +6 oxidations states, while neptunium and plutonium both have richer redox chemistry with accessible the +3, +4, +5, and +6 oxidation states. Although the U^{4+} ion plays a significant role in acidid aqueous conditions and, in the presence of strong reducing agents, can be stabilized, U^{4+} is quite easily oxidized to hexavalent uranium. The reaction for this process is shown below in equation 1 and is favored by +0.902V.[9] The

$$2U^{4+} + O_2 + 2H_2O \leftrightarrow 2UO_2^{2+} + 4H^+ \quad (1)$$

redox chemistry of neptunium and plutonium is richer and more complex.[10a,b] Latimer diagrams for these elements are shown in Figures 1.6 and 1.7 and reveal interesting features that can result during hydrothermal chemistry with neptunium or plutonium. The positive reduction potential of Np(VI) to Np(V) is significantly larger than the negative oxidation potential of Np(IV) to Np(V) resulting in possible comproportionation reactions. In the case of plutonium, it can be seen that the reduction potentials for the one electron reduction of Pu(VI), Pu(V), and Pu(IV), as well as the two electron reduction of Pu(VI) to Pu(IV) are all very close to 1 V. As such, the insolubility of Pu^{4+} can play a major role in the hydrothermal chemistry of plutonium. As a general rule, actinides in

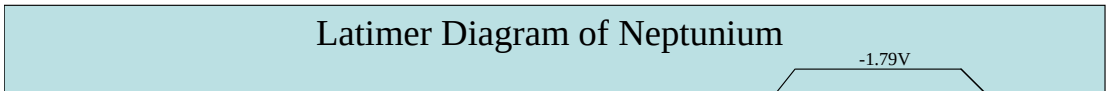

Figure 1.6. Latimer diagram of neptunium.[10a]

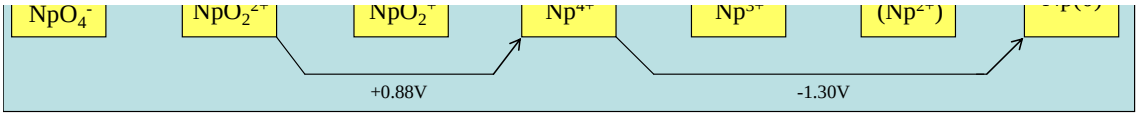

Figure 1.7 Latimer diagram of plutonium.[10b]

the +3 and +4 oxidation states are insoluble in mildly acidic to alkaline conditions and, in the absence of strong inner-sphere coordinating anions such as iodate or phosphate, highly soluble in the +5 and +6 oxidation states. Acidic conditions, coupled with heating, are often enough to oxidize insoluble tetravalent An species to soluble the hexavalent AnO_2^{2+} cation. This linear dioxo actinyl cation, AnO_2^{n+} (An = U, Np, Pu; n = 1,2) is an omnipresent feature of actinides in the +5 or +6 oxidation states and can bind equatorially to four, five, or six oxygen atoms. The result is a tetragonal, pentagonal, or hexagonal bipyramidal local geometry around the central actinide atom. Tetravalent actinides are typically eight or nine coordinate wherein the An^{4+} cation sits inside some variation of a square prism, square anti-prism, or bi- or tri-capped trigonal prism.[10c]

HYDROTHERMAL CHEMISTRY

Hydrothermal chemistry is a commonly used technique for producing well ordered single crystals of products in order to attain structural knowledge of solid state systems in question. Figure 1.8 shows a cartoon depiction of the autoclaves used, as well as pictures of the individual components and the assemble unit. A typical reaction includes loading 10 mL or 23 mL PTFE liners with salts or oxides of the elements one desires to be present in the product, adding a small amount of water, sealing and heating for some period of time. The high temperature and pressure that can be attained in this system allows opportunity to probe kinetic properties not available to traditional solid state reactions and can be used to essentially age the reactants, simulating geological timelines. Hence, this technique lends itself well to predicting the possible alteration phases produced by long-term interaction of actindes, both soluble and insoluble, with

(a)

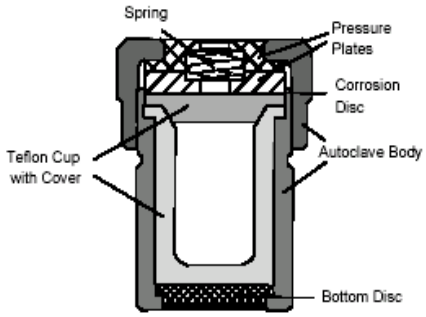

(b)

(c)

Figure 1.8. Components of autoclave used for hydrothermal synthesis shown as (a) components, (b) a cartoon depiction, and (c) an assembled unit.[11]

ancillary species present either in the environment surround the SNF repository or inside the waste itself.

MAGNETIC SUSCEPTIBILITY

Magnetic properties of actinide ions are often complex and show very individual characteristics for each electronic configuration. The 5*f* electrons of the early actinides, Th-Pu, extend out far enough, as compared to the lanthanides and later actinides, that electronic and magnetic characteristics do not solely arise from spin-orbit interactions, but also from interactions with ligand valence orbitals, i.e. crystal field effects.[12,13] Magnetic data are often plotted as the magnetic susceptibility (χ) versus temperature (T). Fitting the linear portion of a plot of $1/\chi$ vs T to the Curie-Weiss law:

$$\chi_m = C/(T-\theta) + \chi_{TIP} \quad (2),$$

where χ_m is the molar magnetic susceptibility (emu mol^{-1}), T and the Weiss constant (θ) are expressed in Kelvin, and χ_{TIP} is the temperature independent paramagnetism of the sample and is in units of emu mol^{-1}, allows one to make inferences regarding the magnetic interactions and possible long range ordering in a sample. From this fitting, in addition to the determination of the Weiss constant which gives information regarding the possible presence of antiferromagnetic or ferromagnetic interactions, an effective magnetic moment (μ_{eff} in terms of Bohr magnetons, μ_B) can be calculated using the following equation:

$$\mu_{eff} = 2.828[\chi_m(T-\theta)]^{1/2} \quad (3).$$

If the inverse susceptibility does not follow the Curie-Weiss law, the Weiss term is omitted. This value of μ_{eff} is compared to the free-ion calculated effective magnetic moment and can give indication to the amount of effect the crystal field has on the central atom.

REFERENCES

1) Seaborg, G. T. *The Transuranium Elements*; Yale University Press: New Haven, CT, 1958.

2) Gillespie, R. J.; Robinson, E. A. *Chem. Soc. Rev.* **2005**, *34(5)*, 396.

3) a) Grohol, D.; Gingl, F.; Clearfield, A. *Inorg. Chem.* **1999**, *38(4)*, 751. b) Grohol, D.; Clearfield A. *J. Am. Chem. Soc.* **1997**, *119(39)*, 9301. c) Grohol, D.; Subramanian, M. A.; Poojary, D. M.; Clearfield, A. *Inorg. Chem.* **1996**, *35(18)*, 5264. d) Poojary, D. M.; Cabeza, A.; Aranda, M. A. G.; Bruque, S.; Clearfield, A. *Inorg. Chem*. **1996**, *35(60)*, 1468. e) Doran, M. B.; Norquist, A. J.; O'Hare, D. *Chem. Mat.* **2003**, *15(7)*, 1449.

4) Sykora, R. E.; Shvareva, T. Y.; Albrecht-Schmitt, T. E. Actinide Compounds with Heavy Oxoanions Containing a Stereochemically Active Lone-Pair of Electrons. In *Structural Chemistry of Inorganic Acinide Compounds*; Elsevier: New York, NY, 2007; p 183.

5) Lauf, R. *Introduction to Radioactive Minerals*; Schiffer Publishing Ltd.: Atglen, PA, 2008.

6) Leiser, K. H. Nuclear Fission. In *Nuclear and Radiochemistry: Fundamentals and Applications*; VCH Publishers, Inc.: Ney York, NY, 1997; p.154.

7) a) Bean, A. C.; Peper, S. M.; Albrecht-Schmitt, T. E. *Chem. Mat*. **2001**, *13(4)*, 1266. b) Bray, T. H.; Beitz, J. V.; Bean, A. C.; Yu, Y.; Albrecht-Schmitt, T. E. *Inorg. Chem.* **2006**, *45(20)*, 8251. c) Shvareva, T. Y.; Almond, P. M.; Albrecht-Schmitt, T. E. *J. Solid State Chem.* **2005**, *178*, 499. d) Shvareva, T. Y.; Almond, P. M.; Albrecht-Schmitt, T. E. *J. Solid State Chem.* **2005**, *178*, 499. e) Bean, A.

C.; Ruf, M; Albrecht-Schmitt, T. E. *Inorg. Chem*. **2001**, *40(16)*, 3959. f) Bean, A. C.; Albrecht-Schmitt, T. E.; *J. Solid State Chem*. **2001**, *161(2)*, 416. g) Bean, A. C.; Campana, C. F.; Kwon, O.; Albrecht-Schmitt, T. E. *J. Am. Chem. Soc*. **2001**, *123(36)*, 8806. h) Sykora, R. E.; McDaniel, S. M.; Wells, D. M.; Albrecht-Schmitt, T. E. *Inorg. Chem*. **2002**, *41(20)*, 5126. i) Sykora, R. E.; Albrecht-Schmitt, T. E. *Inorg. Chem*. **2003**, *42(7)*, 2179. j) Sykora, R. E.; Assefa, Z.; Haire, R. G.; Albrecht-Schmitt, T. E. *Inorg. Chem.* **2005**, *44(16)*, 5667. k) Almond, P. M.; Peper, S. M.; Bakker, E.; Albrecht-Schmitt, T. E. *J. Solid State Chem.* **2003**, *171(1-2)*, 455. l) Almond, P. M.; Albrecht-Schmitt, T. E. *American Mineralogist*. **2004**, *89(7)*, 976. m) Almond, P. M.; Peper, S. M.; Bakker, E; Albrecht-Schmitt, T. E. *J. Solid State Chem.* **2002**, *168(2)*, 358. n) Almond, P. M.; Albrecht-Schmitt, T. E. *Inorg. Chem*. **2003**, *42(18)*, 5693.

8) a) Bray, T. H.; Ling, J.; Choi, E. S.; Brooks, J. S.; Beitz, J. V.; Sykora, R. E.; Haire, R. G.; Stanbury, D. M.; Albrecht-Schmitt, T. E. *Inorg. Chem.* **2007**, *46(9)*, 3663. b) Albrecht-Schmitt, T. E.; Almond, P. M.; Sykora, R. E. *Inorg. Chem*. **2003**, *42(12)*, 3788. c) Bean, A. C.; Scott, B. L.; Albrecht-Schmitt, T. E.; Runde, W. *Inorg. Chem.* **2003**, *42(18)*, 5632. d) e) Runde, W.; Bean, A. C.; Albrecht-Schmitt, T. E.; Scott, B. L. *Chem. Comm*. **2003**, *4*, 478. f) Runde, W.; Bean, A. C.; Scott, B. L. *Chem. Comm.* **2003**, *15*, 1848. g) Sykora, R. E.; Assefa, Z.; Haire, R. G.; Albrecht-Schmitt, T. E. *Inorg. Chem.* **2005**, *44(16)*, 5667. h) Runde, W.; Bean, A. C.; Brodnax, L. F.; Scott, B. L. *Inorg. Chem.* **2006**, *45(6)*, 2479. i) Sykora, R. E.; Assefa, Z.; Haire, R. G.; Albrecht-Schmitt, T. E. *Inorg. Chem.* **2006**, *45(2)*, 475. j) Unpublished results. k) Almond, P. M.; Sykora, R. E.;

Skanthakumar, S; Soderholm, L.; Albrecht-Schmitt, T. E. *Inorg. Chem.* **2004**, *43(3)*, 958. l) Bray, T. H.; Skanthakumar, S.; Soderholm, L.; Sykora, R. E.; Haire, R. G.; Albrecht-Schmitt, T. E. *J. Solid State Chem.* **2008**, *181(3)*, 493.

9) Vanysek, P; Electrochemical Series. In *CRC Handbook of Chemistry and Physics*. CRC Press: Boca Raton, FL, 75th Ed., 1994; p 8-21.

10) a) Yoshide, Z.; Johnson, S. G.; Kimura, T.; Krsul, J. R. Neptunium. In *The Chemistry of the Actinide and Transactinide Elements*; Springer: Dordrecht, The Netherlands, 2006; Vol. 2, p 699. b) Clark, D. L.; Hecker, S. S.; Jarvinen, G. D.; Neu, M. P. Plutonium. In *The Chemistry of the Actinide and Transactinide Elements*; Springer: Dordrecht, The Netherlands, 2006; Vol. 2, p 813.
c) Gutowski, K. E.; Bridges, N. J.; Rogers, R. D. Actinide Structural Chemistry. In *The Chemistry of the Actinide and Transactinide Elements*; Springer: Dordrecht, The Netherlands, 2006; Vol. 4, p 2380.

11) Parr Instrument Bulletin: 4700 0500 4000, p 4.

12) Edelstein, N. M.; Lander, G. H. Magnetic Properties. In *The Chemistry of the Actinide and Transactinide Elements*; Springer: Dordrecht, The Netherlands, 2006; Vol. 4, p 2225.

13) Orchard, A. F. *Oxford Chemistry Primers: Magnetochemistry*; Oxford Univeristy Press: New York, NY, 2003.

CHAPTER 2

THE FIRST MOLECULAR URANYL IODATE, $Na_2[UO_2(IO_3)_4(H_2O)]$: STRUCTURAL POLARITY INDUCED BY COOPERATIVE HYDROGEN BONDING AND LONE-PAIR ALIGNMENT

Reproduced with permission from Bray, Travis H.; Beitz, James V.; Bean, Amanda C.; Yu, Yaqin; Albrecht-Schmitt, Thomas E. *Inorg. Chem.* **2006**, *45*, 8251-8257. Copyright 2006 American Chemical Society.

ABSTRACT

$Na_2[UO_2(IO_3)_4(H_2O)]$ has been synthesized under mild hydrothermal conditions. The structure consists of Na^+ cations and $[UO_2(IO_3)_4(H_2O)]^{2-}$ anions. The $[UO_2(IO_3)_4(H_2O)]^{2-}$ anions are formed from the coordination of a nearly linear uranyl, UO_2^{2+}, cation by four monodentate IO_3^{1-} anions and a coordinating water molecule to yield a pentagonal bipyramidal environment around the uranium center. The water molecules form intermolecular hydrogen bonds with the terminal oxo atoms of neighboring $[UO_2(IO_3)_4(H_2O)]^{2-}$ anions to yield one-dimensional chains that extend down the *b* axis. There are two crystallographically unique iodate anions in the structure of $Na_2[UO_2(IO_3)_4(H_2O)]$. One of these anions is aligned so that the lone-pair of electrons is also directed along the *b* axis. The overall structure is therefore polar owing to the cooperative alignment of both the hydrogen bonds and the lone-pair of electrons on iodate. The polarity of the monoclinic space group *C*2 (a = 11.3810(12) Å, b = 8.0547(8)

Å, *c* = 7.6515(8) Å, β = 90.102(2)°, *Z* = 2, T = 193 K) found for this compound is consistent with the structure. Second-harmonic generation of 532 nm light from a 1064 nm laser source yields a response of 16× α-SiO_2.

INTRODUCTION

Actinide iodates have been the subject of recent intense interest owing primarily to their rich structural chemistry. In the past six years, examples of Th,[1] U,[2] Np,[3] Pu,[3c,4] Am,[5] Cm,[6] and even Cf[7] iodates have been reported. This family of compounds spans several themes in the area of f-block elements with oxoanions containing a nonbonding, but stereochemically active lone-pair of electrons. Some of these topics include the formation of noncentrosymmetric structures, a feature that is often ascribed to the alignment of the lone-pairs in the solid state,[3c,3d,4a,5a] and the apparent excision of low-dimensional substructures from higher dimensional structure types.[2f,2g] Both of these attributes can be identified in uranium, neptunium, and plutonium iodates. The early actinide iodates have thus far been isolated with the actinides in the +5 or +6 oxidation states, and therefore contain the requisite approximately linear dioxo actinyl cation, AnO_2^{n+} (An = U, Np, Pu; n = 1, 2).

In uranyl iodates, the lone-pair of electrons on I(V) can play a number of roles in both the local and extended structural chemistry. In general, the presence of a lone-pair of electrons on an oxoanion has been found to reduce the overall dimensionality from the layered forms that dominate uranyl solids,[8] to one-dimensional chain and ribbon structures. This occurs in anhydrous uranyl iodate, $UO_2(IO_3)_2$,[2b] as well more complex materials, such as $Cs_2[(UO_2)_3Cl_2(IO_3)(OH)O_2]\cdot 2H_2O$,[2c] $Rb[(UO_2)(CrO_4)(IO_3)(H_2O)]$,[2d]

$A_2[(UO_2)(MO_4)(IO_3)_2]$ (A = K, Rb, Cs; M = Cr, Mo),[2d,2e] $A_2[(UO_2)_3(IO_3)_4O_2]$ (A = K, Rb, Tl),[2f,2g] $AE[(UO_2)_2(IO_3)_2O_2]$ (AE = Sr, Ba, Pb),[2f,2g] $K_3[(UO_2)_2(IO_3)_6](IO_3)\cdot H_2O$,[2h] and $K[UO_2(IO_3)_3]$.[2j] Until now, the creation of acentric structures ascribed to lone-pair alignment has been absent from uranyl iodate chemistry, but it is displayed in the Np(V) iodate, $NpO_2(IO_3)$,[3d] and in An(VI) iodates, $AnO_2(IO_3)_2\cdot H_2O$ (An = Np, Pu).[3c,4a] We report the preparation and characterization of the first zero-dimensional, or molecular, uranyl iodate, $Na_2[UO_2(IO_3)_4(H_2O)]$. This compound adopts a polar structure owing to cooperative alignment of both hydrogen bonds from coordinated water molecules and the lone-pairs of electrons on the iodate anions.

EXPERIMENTAL

General Information. $UO_2(NO_3)_2\cdot 6H_2O$ (98%, Alfa-Aesar), UO_3 (99.8%, Alfa-Aesar), 2,2'-bipyridyl (99%, Alfa-Aesar), I_2O_5 (98%, Alfa-Aesar), NaCl (99%, Alfa-Aesar), HCl (37.4%, Fisher Scientific), and $NaHCO_3$ (99%, Alfa Aesar) were used as received. Reactions were run in PTFE-lined Parr 4749 autoclaves with a 23 mL internal volume. Distilled and Millipore filtered water with a resistance of 18.2 MΩ·cm was used in all reactions. Standard precautions were performed for handling radioactive materials during work with $UO_2(NO_3)_2\cdot 6H_2O$, UO_3, and the products of the reactions. Semi-quantitative EDX analyses were performed using a JEOL 7000F field emission SEM. Na, U, and I percentages were calibrated against standards.

$Na_2[UO_2(IO_3)_4(H_2O)]$ Synthesis (Method 1). $UO_2(NO_3)_2\cdot 6H_2O$ (82.8 mg, 0.165 mmol), I_2O_5 (175.4 mg, 0.525 mmol), 2,2'-bipyridyl (32.8 mg, 0.210 mmol), HCl (0.05 mL, 0.018 mmol), $NaHCO_3$ (132.4 mg, 1.58 mmol), and 1.5 mL of water were loaded

into a 23 mL autoclave. The autoclave was sealed and heated to 120 ^{o}C in a box furnace for 7 d. The autoclave was then cooled at an average rate of 9 ^{o}C/h to room temperature. The product consisted of yellow crystals ranging in habit from small rectangular plates to nearly cubic prisms, all of which were $Na_2[UO_2(IO_3)_4(H_2O)]$. The product was thoroughly washed with water, then rinsed with methanol, and allowed to dry. Yield, 153 mg (90% based on U). EDX analysis provided Na:U:I ratio of approximately 2:1:4. IR (KBr, cm^{-1}) vibrational bands are given in Table 2.1.[9]

$Na_2[UO_2(IO_3)_4(H_2O)]$ Synthesis (Method 2). UO_3 (114.9 mg, 0.4017 mmol), I_2O_5 (267.9 mg, 0.8026 mmol), NaCl (117.3 mg, 2.0071 mmol), and 0.5 mL of water were loaded into a 23 mL autoclave. The autoclave was sealed and heated to 180 ^{o}C in a box furnace for 3 d. The autoclave was then cooled at an average rate of 9 ^{o}C/h to room temperature. The product consisted of yellow crystals of $Na_2[UO_2(IO_3)_4(H_2O)]$. The product was thoroughly washed with water, then rinsed with methanol, and allowed to dry. Powder X-ray diffraction data were used to confirm product purity. Yield, 362 mg (87% based on U).

Crystallographic Studies. A single crystal of $Na_2[UO_2(IO_3)_4(H_2O)]$ with dimensions of 0.128 x 0.124 x 0.082 mm, was mounted on a glass fiber and optically aligned on a Bruker APEX CCD X-ray diffractometer using a digital camera. Initial intensity measurements were performed using graphite monochromated Mo Kα radiation from a sealed tube and monocapillary collimator. SMART (v 5.624) was used for preliminary determination of the cell constants and data collection control. The intensities of reflections of a sphere were collected by a combination of 3 sets of exposures (frames). Each set had a different ϕ angle for the crystal and each exposure

Table 2.1. IR vibrational modes for $Na_2[UO_2(IO_3)_4(H_2O)]$ (KBr, cm^{-1}).

UO_2^{2+}	IO_3^-	H_2O
903 (ν_3)	816 (ν)	3290 (ν)
865 (ν_1)	796 (ν)	3186 (ν)
	786 (ν)	1622 (δ)
	763 (ν)	
	731 (ν)	
	697 (ν)	
	564 (δ)	

covered a range of 0.3° in ω. A total of 1800 frames were collected with an exposure time per frame of 30 s. For $Na_2[UO_2(IO_3)_4(H_2O)]$, determination of integrated intensities and global refinement were performed with the Bruker SAINT (v 6.02) software package using a narrow-frame integration algorithm. These data were treated with a semi-empirical absorption correction by SADABS.[10] The program suite SHELXTL (v 6.12) was used for space group determination (XPREP), direct methods structure solution (XS), and least-squares refinement (XL).[11] The final refinements included anisotropic displacement parameters for all atoms. Secondary extinction was not noted. Crystals of $Na_2[UO_2(IO_3)_4(H_2O)]$ crystallize in the polar monoclinic space group *C*2. The crystal used for these X-ray diffraction experiments proved to be an enantiomorphic twin with a Flack parameter of 0.459(7). Missed symmetry was checked for using the ADDSYMM and NEWSYMM programs that are a part of the PLATON package.[12] This was particularly important because the suspiciously small β angle of 90.102(2)° is often caused by twinning or pseudo-orthorhombic symmetry – neither were detected. Some crystallographic details are given in Table 2.2. X-ray crystallographic information file and powder X-ray diffraction data for $Na_2[UO_2(IO_3)_4(H_2O)]$ is available via the Internet at http://pubs3.acs.org/acs/journals/supporting_information.page?in_coden=inocaj&in_volume=45&in_start_page=8251.

Nonlinear Optical Measurements performed by James V. Beitz, Chemistry Division, Argonne National Laboratory, Argonne, Illinois 60439. Powder second-harmonic generation (SHG) measurements were performed on a Kurtz-Perry nonlinear optical system[13] as modified by Porter and coworkers,[14] and updated here to include laser 1064 nm light used for all measurements. The SHG intensity was recorded from 60 mg

Table 2.2. Crystallographic data for $Na_2[UO_2(IO_3)_4(H_2O)]$.

Formula	$Na_2[UO_2(IO_3)_4(H_2O)]$
Formula Mass	1033.63
Color and habit	yellow prism
Space group	*C*2 (No. 5)
a (Å)	11.3810(12)
b (Å)	8.0547(8)
c (Å)	7.6515(8)
α (°)	90
β (°)	90.102(2)
γ (°)	90
V (Å^3)	701.42(13)
Z	2
T (K)	193
λ (Å)	0.71073
Maximum 2θ (deg.)	56.54
ρ_{calcd} (g cm^{-3})	4.884
μ(Mo *K*α) (cm^{-1})	205.13
R(*F*) for $F_o^2 > 2\sigma(F_o^2)$[a]	0.0263
$R_w(F_o^2)$[b]	0.0675

[a] $R(F) = \sum \| |F_o| - |F_c| \| / \sum |F_o|$. [b] $R_w\left(F_o^2\right) = \left[\sum \left[w\left(F_o^2 - F_c^2\right)^2 \right] / \sum wF_o^4 \right]^{1/2}$.

pulse energy normalization.a Q-switched Nd:YAG laser (Continuum Surelite I-10), operated at 10 Hz, provided theof $Na_2[UO_2(IO_3)_4(H_2O)]$ and from finely ground α-quartz (crystalline SiO_2). These powders were placed in separate glass tubes of the same dimensions. No index of refraction matching fluid was used in these experiments. The SHG light at 532 nm was collected in reflection, selected by a narrow band-pass interference filter (Pomfret) and detected by a photomultiplier tube (RCA 1P28). A near normal incidence beam splitter reflected a small fraction of the laser beam onto a pyroelectric detector (Molectron J3-05) that was used as a laser pulse energy monitor. A digital storage oscilloscope (Tektronix TDS 640A) signal averaged and recorded both the SHG and incident laser energy signals. Average laser power was measured separately with a calibrated Scientech volume absorber calorimeter. The observed SHG intensity per unit laser intensity, $I^{2\omega}$, was obtained by dividing the SHG signal by the laser energy signal. Replicate measurements determined the value of interest for the sample compound, $I^{2\omega}$ (s), and for α-quartz, $I^{2\omega}$ (q). The ratio of these values, $I^{2\omega}$ (s) / $I^{2\omega}$ (q), was found to be 16 at an incident laser intensity of 17 MW/cm^2.

Thermal Analysis. Thermal data for $Na_2[UO_2(IO_3)_4(H_2O)]$ were collected using a TA Instruments, Model 2920 Differential Scanning Calorimeter (DSC) and a TA Q50 Thermogravimetric Analyzer (TGA). Samples (~10 mg) were encapsulated in aluminum or platinum pans and heated at 10 °C/min from 25 °C to 600 °C (DSC) and from 25 °C to 400 °C (TGA) under a nitrogen atmosphere.

Powder X-ray Diffraction. Powder X-ray diffraction patterns were collected with a Rigaku Miniflex powder X-ray diffractometer using Cu Kα (λ = 1.54056 Å) radiation.

RESULTS AND DISCUSSION

Synthesis. The synthesis of $Na_2[UO_2(IO_3)_4(H_2O)]$ differs from that of most uranyl iodates in that the pH was intentionally increased through the addition of both bicarbonate and 2,2'-bipyridyl. Both the bicarbonate and 2,2'-bipyridyl are sacrificial The former is decomposed by the acidic conditions, and the latter is subject to both oxo atom transfer (oxidation) and iodination by the iodate anion under these conditions.[15] The initial pH of the mixture is approximately 1.3, but increases to 4.1 over the course of the reaction, resulting in the formation of single crystals of $Na_2[UO_2(IO_3)_4(H_2O)]$ (Method 1). We have found that the crystallinity of the product can be substantially improved through the addition of a few drops of conc. HF to the initial reaction mixture. Alternatively, $Na_2[UO_2(IO_3)_4(H_2O)]$ can be prepared in a straightforward manner by reacting NaCl with UO_3 and I_2O_5 under hydrothermal conditions (Method 2). Using this method, the average size of crystals steadily increases as the amount of water is decreased from 3 to 1 to 0.5 mL. Considering the ease of synthesis, this second preparation is somewhat preferable, however crystals grown using Method 2 have been twinned.

Structural Features of $Na_2[UO_2(IO_3)_4(H_2O)]$. The structure of $Na_2[UO_2(IO_3)_4(H_2O)]$ is distinct from all previously reported actinyl iodates in that it consists of Na^+ cations and $[UO_2(IO_3)_4(H_2O)]^{2-}$ anions. This is the first molecular actinide iodate. Molecular iodates containing metals are rare in general, being known only from $[CrO_3(IO_3)]^{1-}$,[16] $[MoO_2(IO_3)_4]^{2-}$,[17] and $[M(IO_3)_6]^{2-}$ (M = Ti,[18] Zr,[19] Mo[19]). An important comparison to be made is between the $[MoO_2(IO_3)_4]^{2-}$ and $[UO_2(IO_3)_4(H_2O)]^{2-}$ anions. In the former Mo(VI) compound, the well-known *cis*-MoO_2^{2+} cation exists, and

owing to second-order Jahn-Teller effects,[20] the Mo atom is distorted far from idealized octahedral symmetry. In contrast, the U(VI) compound contains the *trans*-UO_2^{2+} cation. The four iodate anions bind this cation perpendicular to the uranyl axis through a single oxo atom from the iodate anions. The fifth site in the pentagonal plane is occupied by a water molecule. The $[UO_2(IO_3)_4(H_2O)]^{2-}$ anion has two-fold symmetry as is depicted in Figure 2.1. The short U=O bond distances of 1.787(6) Å are typical for uranyl compounds, as is the approximately linear O–U–O angle of 179.2(6)°.[21] The U–O distances to the iodate anions are 2.302(8) and 2.345(7) Å. The longest U–O distance is to the coordinated water molecule with a distance of 2.450(11) Å. This distance is similar to that found between the water molecule and the uranyl cation (2.458(5) Å) in $UO_2(IO_3)_2(H_2O)$.[2b] Furthermore, it should be noted that the $[UO_2(IO_3)_4(H_2O)]^{2-}$ anion is thebasic building unit found in layered structure of $UO_2(IO_3)_2(H_2O)$, as shown in Figure 2.2b Bond-valence sum calculations[22,23] using the parameters for seven-coordinate U(VI) given by Burns et al. yield a value of 6.09,[21] which is consistent with this compound containing hexavalent uranium.

I–O distances within the iodate anions can be roughly correlated with their binding mode. The I–O distances observed where one of the oxygen atoms is involved inbonding to the uranium atom are slightly longer than the terminal ones. In the iodate anions containing I(1), the terminal I–O distances are 1.795(7) and 1.799(7) Å, whereas the bridging oxo atom has a bond distance of 1.843(7). The same pattern is observed for I(2) with terminal distances of 1.793(7) and 1.803(7) Å, and bridging distance of 1.811(7) Å. Here, the bond distance variations are not statistically significant. Bond-valence sums for I(1) and I(2) are 4.99 and 5.12, respectively.[22,23] These bond-valences are consistent

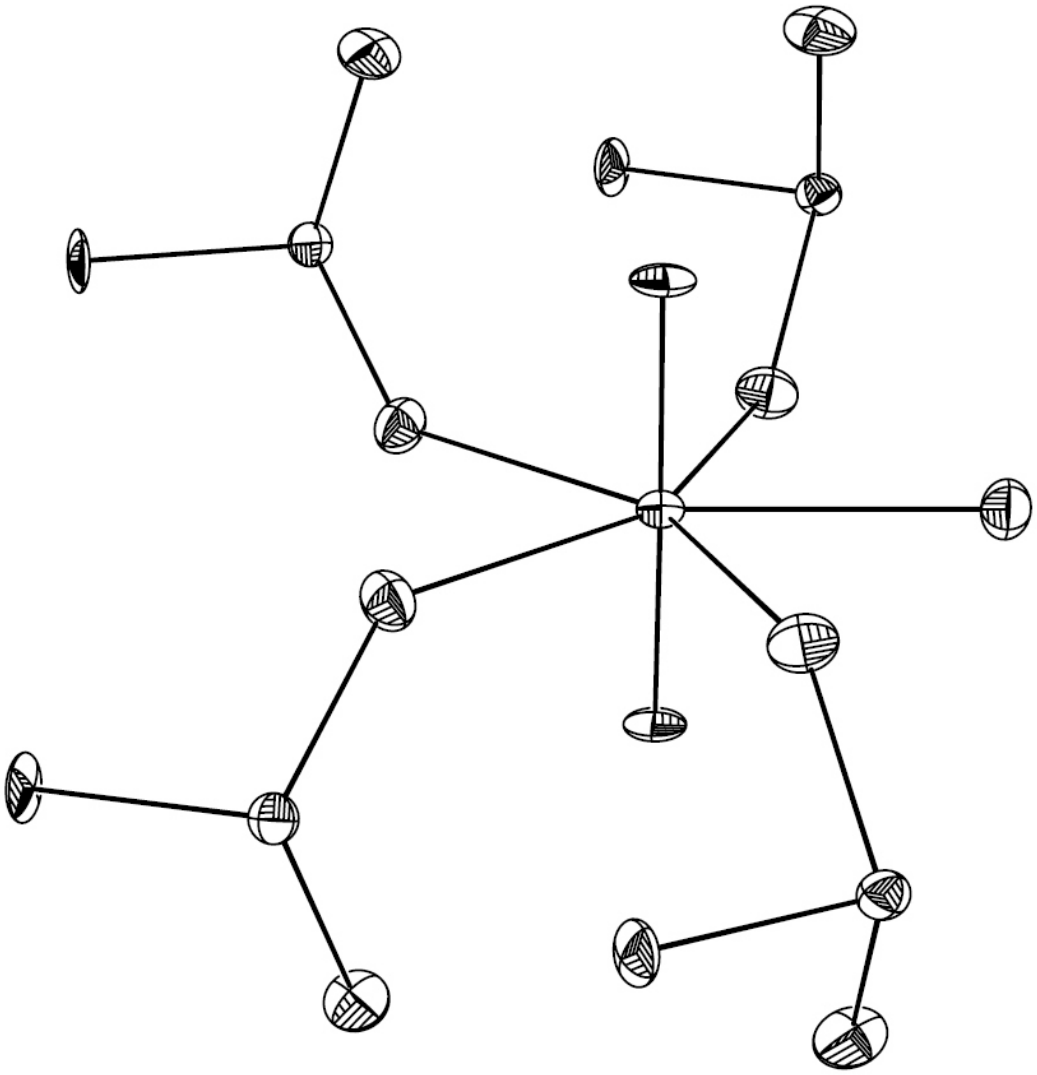

Figure 2.1 View of the structure of the $[UO_2(IO_3)_4(H_2O)]^{2-}$ anion in $Na_2[UO_2(IO_3)_4(H_2O)]$, which has imposed 2-fold symmetry. 50% probability ellipsoids are depicted.

with I(V). Selected bond distances and angles are given in Table 2.3.

$Na_2[UO_2(IO_3)_4(H_2O)]$ further deviates from previously known uranyl iodates in that the structure is polar. Polarity in actinyl iodates has been previously observed in $AnO_2(IO_3)_2{\cdot}H_2O$ (An = Np, Pu)[3c,4a] and $NpO_2(IO_3)$,[3d] wherein the iodate anions are all aligned so that the lone-pair of electrons are directed along a single crystallographic axis. Similar alignment is also observed in the structure of $Na_2[UO_2(IO_3)_4(H_2O)]$ where each of the crystallographically unique iodate units in the $[UO_2(IO_3)_4(H_2O)]^{2-}$ anion is aligned along the *b* axis, as is shown in Figure 2.3. Owing to translational symmetry all of the $[UO_2(IO_3)_4(H_2O)]^{2-}$ anions are therefore aligned in the same manner in the overall $UO_2(IO_3)_2(H_2O)$.[2b] Furthermore, it should be noted that the $[UO_2(IO_3)_4(H_2O)]^{2-}$ anion is the basic building unit found in layered structure of $UO_2(IO_3)_2(H_2O)$ as shown in Figure 2.2.[2b] Bond-valence sum calculations[22,23] using the parameters for seven coordinate

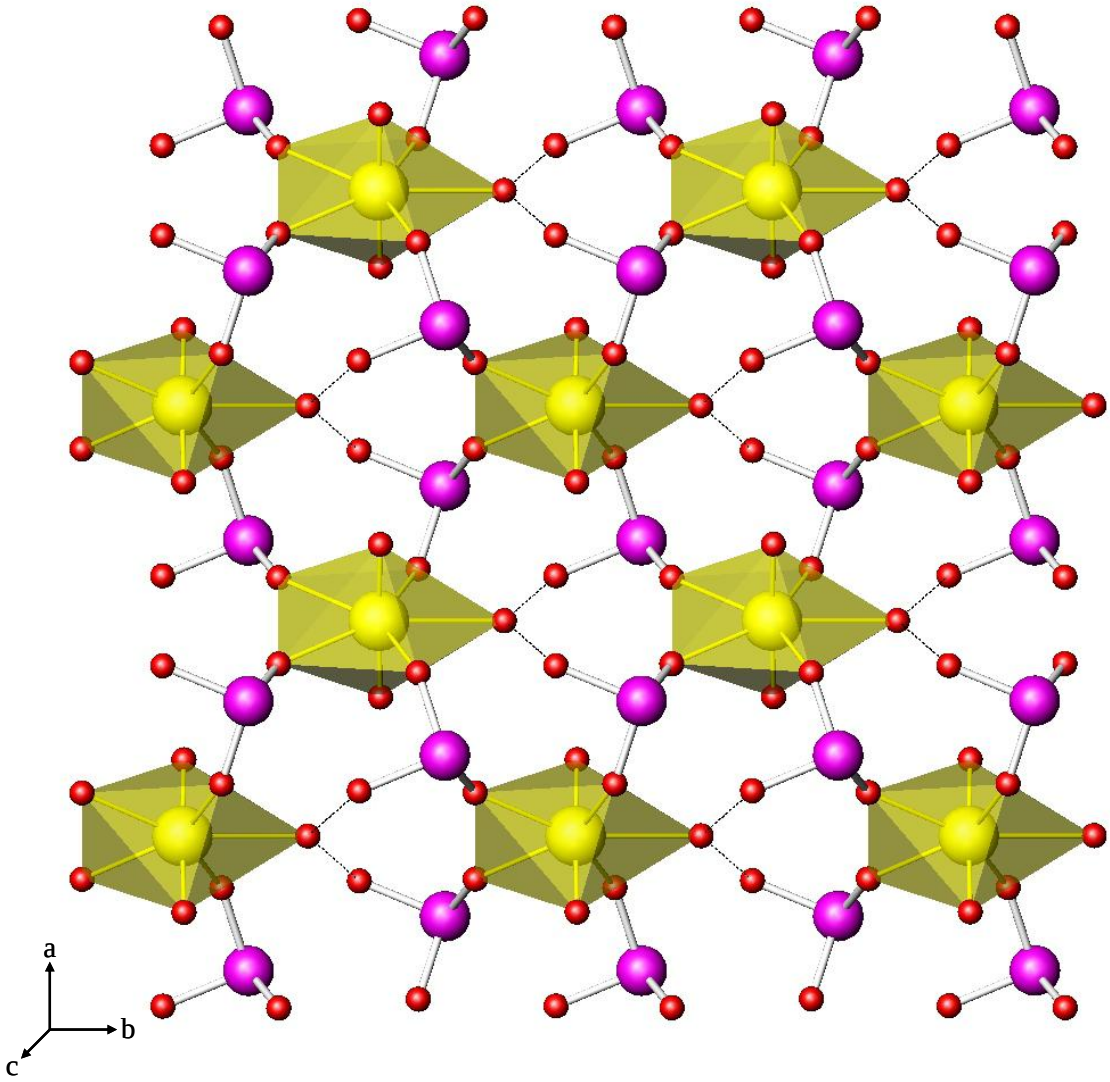

Figure 2.2. Illustration of $[UO_2(IO_3)_4(H_2O)]$ units found in $UO_2(IO_3)_2(H_2O)$.

Table 2.3. Selected bond distances (Å) and angles (°) for $Na_2[UO_2(IO_3)_4(H_2O)]$.

Distances (Å)			
U(1)–O(1) (× 2)	2.302(8)	I(1)–O(1)	1.843(7)
U(1)–O(5) (× 2)	2.345(7)	I(1)–O(2)	1.799(7)
U(1)–O(7) (H_2O)	2.450(11)	I(1)–O(3)	1.795(7)
U(1)–O(8) (× 2)	1.787(6)	I(2)–O(4)	1.803(7)
		I(2)–O(5)	1.811(7)
		I(2)–O(6)	1.793(7)
Angles (°)			
O(8)–U(1)–O(8)'	179.2(6)		

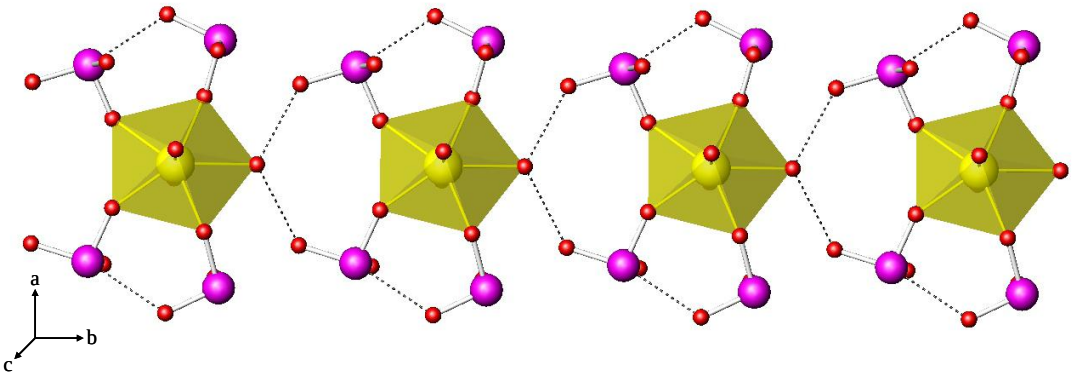

Figure 2.3. Depiction of the one-dimensional chains of $[UO_2(IO_3)_4(H_2O)]^{2-}$ anions formed through intermolecular hydrogen bonds between coordinating water molecules and oxo atoms of iodate from adjacent anions. Dashed lines between iodate anions indicate iodate···iodate interactions that orient iodate anions along the *b* axis.

U(VI) given by Burns *et al.* yield a value of 6.09,[21] which is consistent with this compound containing hexavalent uranium.structure. The oddity of this observation is that, because the iodate anions are monodentate, they should be able to freely rotate in solution, and, at first glace, there is no obvious reason for alignment in the solid state; however, as will become clear, there are a series of intermolecular interactions that account for the lone-pair alignment.

One of the key features of the structure of $Na_2[UO_2(IO_3)_4(H_2O)]$ is that all of the water molecules are oriented so that they lie along the *b* axis. There are short O···O intermolecular contacts of 2.762(7) Å that are of appropriate length for hydrogen bonding between the water molecule of one $[UO_2(IO_3)_4(H_2O)]^{2-}$ anion and the neighboring terminal oxo atoms of the iodate anions in an adjacent anion. As can be seen in Figure 2.3, the hydrogen bonds yield one-dimensional chains that extend down the *b* axis. These hydrogen bonds orient one of the crystallographically unique iodate anions (I(2)). The second iodate anion, containing I(1), is more strongly aligned along the *b* axis than the I(2) iodate anion. Its alignment can be ascribed to intramolecular I···O interactions between iodate molecules in the anion, as depicted in Figure 2.3. This interaction is on the order of 2.827(7) Å, and is typical for intermolecular iodate contacts.[2b,2f,2g,24-26] Therefore, the cooperative coexistence of hydrogen bonds and intermolecular iodate···iodate interactions leads to lone-pair alignment that contributes to the short- and long-range polarity in the structure of $Na_2[UO_2(IO_3)_4(H_2O)]$.

The environments around the Na^+ cations must also contribute to the acentricity of the overall structure of $Na_2[UO_2(IO_3)_4(H_2O)]$. There are two crystallographically

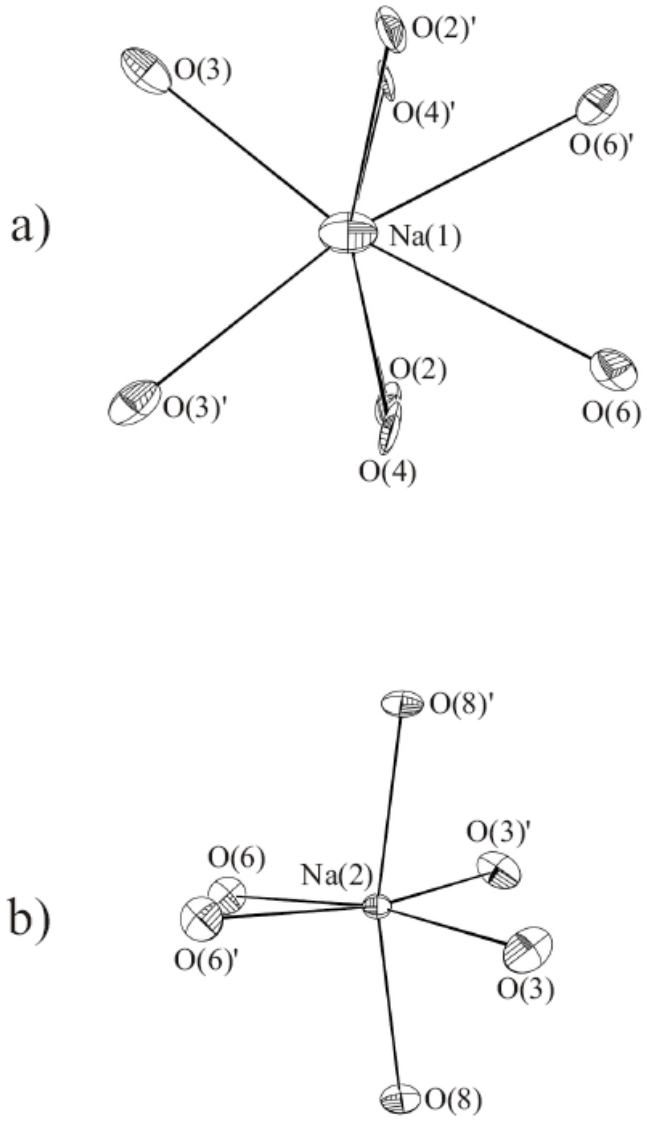

Figure 2.4. (a) View of the distorted dodecahedral environment around Na(1) and (b) the distorted octahedral environment around Na(2) in $Na_2[UO_2(IO_3)_4(H_2O)]$. The environments around the Na^+ cations are consistent with a polar structure.

unique Na^+ cations in this structure. Na(1) forms eight contacts ranging from 2.415(7) to 2.992(11) Å, with surrounding oxygen atoms to yield an approximately dodecahedral environment, as is shown in Figure 2.4a. The Na(1) center is shifted from the center of this unit toward one side by approximately 0.33 Å. Na(2) has six interactions with distances occurring from 2.303(6) to 2.343(9) Å to yield a distorted octahedral geometry, as depicted in Figure 2.4b. The environments around the Na^+ cations are also consistent with a polar structure. A packing diagram for $Na_2[UO_2(IO_3)_4(H_2O)]$ is shown in Figure 2.5.

Structural-Property Relationships in $Na_2[UO_2(IO_3)_4(H_2O)]$. A consequence of the polarity of $Na_2[UO_2(IO_3)_4(H_2O)]$ is that it should be capable of second-harmonic generation (SHG) of laser light. SHG measurements have been made on many alkali metal, transition metal, and lanthanide iodates, yielding a wide range of efficiencies that maximize with values as large as 500x α-quartz for $Cs[(VO)_2(IO_3)_3O_2]$.[27,28] For true quantification of the SHG response, the compounds must be ground into powders and sieved into ranges of particles sizes so that comparisons can be made between the compound in question and a standard using particles in the same size range. Measurements on sieved powders allow one to determine whether the material is Type 1 or Type 2 phase-matchable. While this can be done with relative ease on non-radioactive material, the grinding and, more importantly, the sieving process, disperses fine particles making this procedure unsafe from a contamination standpoint. Therefore, we only make measurements on unsieved powders with radioactive material. The SHG response for the frequency doubling of 1064 nm laser light from a Nd:YAG laser to 532 nm light by $Na_2[UO_2(IO_3)_4(H_2O)]$ was measured on unsieved powders to yield a small response of

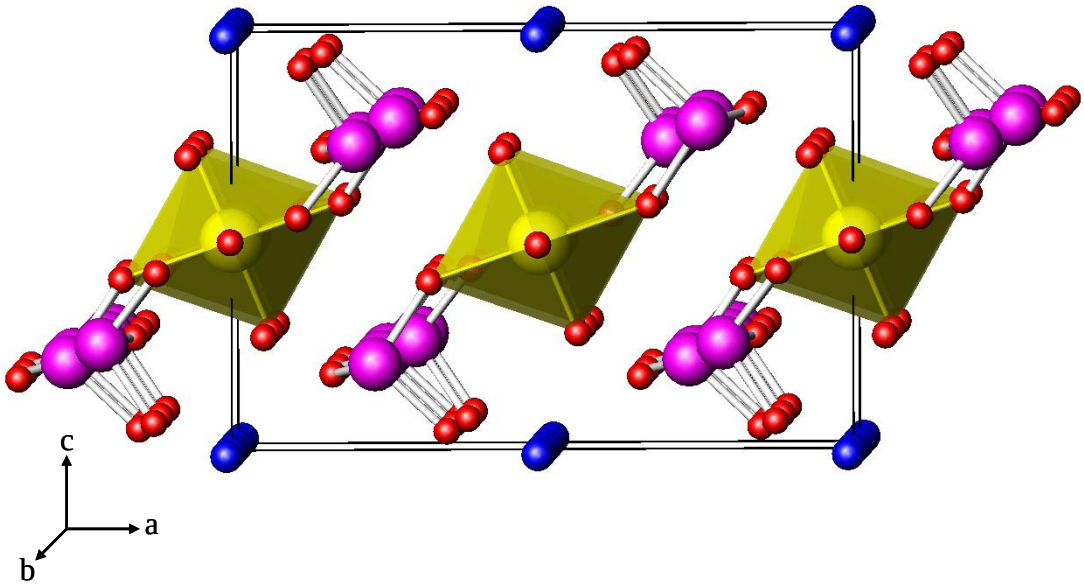

Figure 2.5. Packing diagram for $Na_2[UO_2(IO_3)_4(H_2O)]$.

approximately 16× α-SiO_2. The observation of SHG from this material provides external confirmation of the polarity of the structure.

Thermal Behavior. The thermal stability of $Na_2[UO_2(IO_3)_4(H_2O)]$ was investigated to address two issues. First, does the loss of coordinated water result in substantial structural changes? For example, the removal of water potentially opens a coordination site that the terminal oxo atoms of iodate anions from neighboring complexes might fill, thereby interconnecting $[UO_2(IO_3)_4]$ units into a structure of higher dimensionality. Second, what is the overall stability of a molecular uranyl iodate in comparison with the layered uranyl iodate $UO_2(IO_3)_2(H_2O)$, which contains similar uranyl iodate hydrate building units? A DSC thermogram of $Na_2[UO_2(IO_3)_4(H_2O)]$ reveals a complex series of endotherms beginning at 380 °C, as is shown in Figure 2.6. This large endotherm is followed by small events at 409, 424, and 492 °C, which precede a large multi-component endotherm centered at 543 °C. When combined with TGA data, it was determined that the first endotherm corresponds to water loss. Water loss occurs from $UO_2(IO_3)_2(H_2O)$ at 327 °C, and is not followed by any events until 572 °C, at which point iodate disproportionation takes place.[2b] This is similar to the disproportionation temperature of $Na_2[UO_2(IO_3)_4(H_2O)]$ as well as other actinide iodates such as $Th(IO_3)_2(SeO_4)(H_2O)_3{\cdot}H_2O$ and $Th(CrO_4)(IO_3)_2$, which undergo disproportionation at 537 °C and 543 °C, respectively.[27d] It is of interest to note that if there are multiple crystallographically unique iodate anions, then multiple disproportionation events are often observed, as is the case for $Na_2[UO_2(IO_3)_4(H_2O)]$. Although in this case, multiple iodate decompositions might be caused by the presence of a complex mixture that results from water loss and partial structural reorganization. The endothermic events between

409 and 492 °C may indeed correspond to the formation of novel uranyl iodate structures, but they are unfortunately located too closely to the iodate decomposition temperature for further investigation.

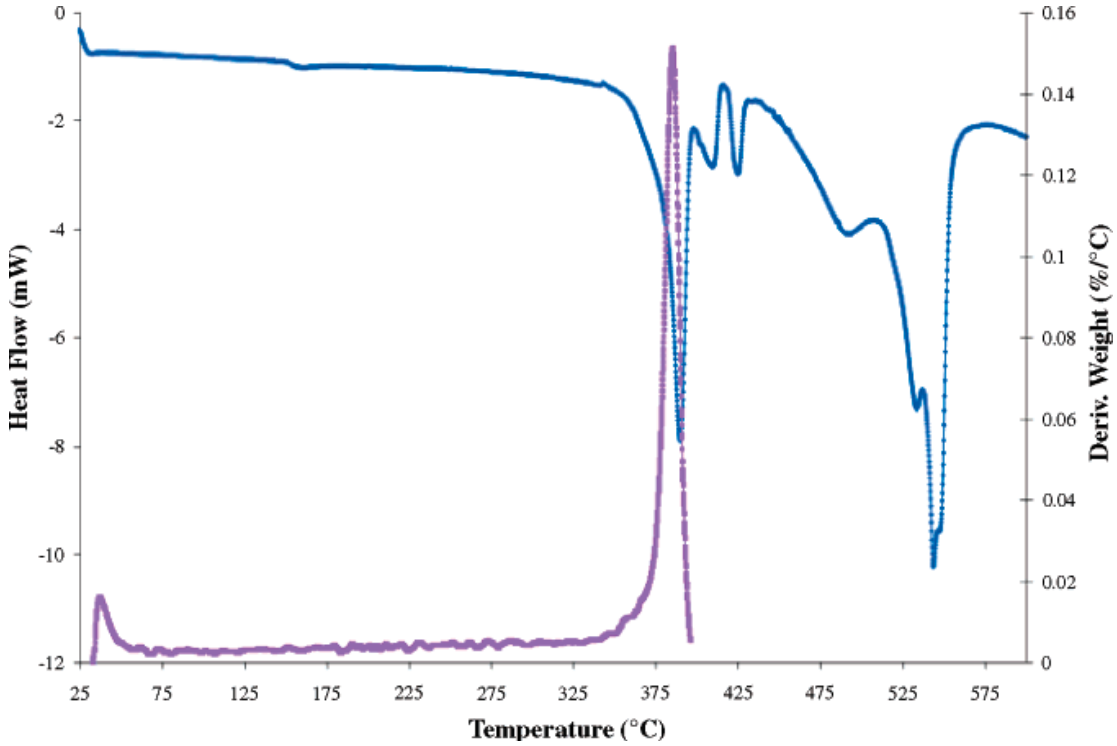

Figure 2.6. DSC and TGA thermograms of $Na_2[UO_2(IO_3)_4(H_2O)]$.

REFERENCES

1) a) Sullens, T. A.; Almond, P. M.; Byrd, J. A.; Beitz, J. V.; Bray, T. H.; Albrecht-Schmitt, T. E. *J. Solid State Chem.* **2006**, *179*, 1192. b) Sullens, T. A.; Almond, P. M.; Albrecht-Schmitt, T. E., *Mater. Res. Soc.*, **2006**, *893*, 283.

2) a) Weigel, F.; Engelhardt, L. W. H. *J. Less-Common Met.* **1983**, *91*, 339. b) Bean, A. C.; Peper, S. M.; Albrecht-Schmitt, T. E. *Chem. Mater.* **2001**, *13*, 1266. c) Bean, A. C.; Xu, Y.; Danis, J. A.; Albrecht-Schmitt, T. E.; Runde, W. *Inorg. Chem.* **2002**, *41*, 6775. d) Sykora, R. E.; McDaniel, S. M.; Wells, D. M.; Albrecht-Schmitt, T. E. *Inorg. Chem.* **2002**, *41*, 5126. e) Sykora, R. E.; Wells, D. M.; Albrecht-Schmitt, T. E. *Inorg. Chem.* **2002**, *41*, 2304. f) Bean, A. C.; Albrecht-Schmitt, T. E. *J. Solid State Chem.* **2001**, *161*, 416. g) Bean, A. C.; Ruf, M.; Albrecht-Schmitt, T. E. *Inorg. Chem.* **2001**, *40*, 3959. h) Sykora, R. E.; Bean, A. C.; Scott, B. L. Runde, W.; Albrecht-Schmitt, T. E. *J. Solid State Chem.* **2004**, *177*, 725. i) Bean, A. C.; Campana, C. F.; Kwon, O.; Albrecht-Schmitt, T. E. *J. Am. Chem. Soc.* **2001**, *123*, 8806. j) Shvareva, T. Y.; Almond, P. M.; Albrecht-Schmitt, T. E. *J. Solid State Chem.* **2005**, *178*, 499.

3) a) Bean, A. C.; Scott, B. L.; Albrecht-Schmitt, T. E.; Runde, W. *J. Solid State Chem.* **2004**, *176*, 1346. b) Sykora, R. E.; Bean, A. C.; Scott, B. L.; Runde, W.; Albrecht-Schmitt, T. E. *J. Solid State Chem.* **2004**, *177*, 725. c) Bean, A. C.; Scott, B. L.; Albrecht-Schmitt, T. E.; Runde, W. *Inorg. Chem.* **2003**, *42*, 5632. d) Albrecht-Schmitt, T. E.; Almond, P. M.; Sykora, R. E. *Inorg. Chem.* **2003**, *42*, 3788.

4) a) Runde, W.; Bean, A. C.; Albrecht-Schmitt, T. E.; Scott, B. L. *Chem. Comm.* **2003**, *4*, 478. b) Bean, A. C.; Abney, K.; Scott, B. L.; Runde, W. *Inorg. Chem.* **2005**, 44, 5209.

5) a) Runde, W.; Bean, A. C.; Scott, B. L. *Chem. Commun.* **2003**, *15*, 1848. b) Sykora, R. E.; Assefa, Z.; Haire, R. G.; Albrecht-Schmitt, T. E. *Inorg. Chem.* **2005**, *44*, 5667. c) Runde, W.; Bean, A. C.; Brodnax, L. F.; Scott, B. L. *Inorg. Chem.* **2006**, *45*, 2479.

6) Sykora, R. E.; Assefa, Z.; Haire, R. G.; Albrecht-Schmitt, T. E. *J. Solid State Chem.* **2004**, *177*, 4413.

7) Sykora, R. E.; Assefa, Z.; Albrecht-Schmitt, T. E.; Haire, R. G. *Inorg. Chem.* **2006**, *45*, 475.

8) a) P. C. Burns, M. L. Miller, R. C. Ewing, *Can. Mineral.* **1996**, *34*, 845. b) P. C. Burns, In *Uranium: Mineralogy, Geochemistry and the Environment*; Burns, P. C.; Finch, R., Eds. Ch. 1, Mineralogical Society of America: Washington, DC, 1999. c) P. C. Burns, *Mater. Res. Soc. Symp. Proc.* **2004**, *802*, 89. d) Burns, P. C. *Can. Mineral.* **2005**, *43*, 1839.

9) a) Pracht, G.; Lange, N.; Lutz, H. D. *Thermochim. Acta* **1997**, *293*, 13. b) Lutz, H. D.; Alici, E.; Kellersohn, Th. *J. Raman Spectrosc.* **1990**, *21*, 387. b) Schellenschlager, V.; Pracht, G.; Lutz, H. D. *J. Raman Spectrosc.* **2001**, *32*, 373. c)Lutz, H. D.; Suchanek, E. *Spectrochim. Acta* **2000**, *A56*, 2707. d) Pracht, G.; Nagel, R.; Suchanek, E.; Lange, N.; Lutz, H. D. *Z. Anorg. Allg. Chem.* **1998**, *624*, 1355. e) Kellersohn, Th.; Alici, E.; Eber, D.; Lutz, H. D. *Z. Kristallogr.* **1993**, *203*, 225.

10) Sheldrick, G. M. *SADABS* 2001, Program for absorption correction using SMART CCD based on the method of Blessing: Blessing, R. H. *Acta Crystallogr.* **1995**, *A51*, 33.

11) Sheldrick, G. M. SHELXTL PC, Version 6.12, An Integrated System for Solving, Refining, and Displaying Crystal Structures from Diffraction Data; Siemens Analytical X-Ray Instruments, Inc.: Madison, WI 2001.

12) Spek, A. L. *Acta Crystallogr.* **1990**, *A46*, C34.

13) Kurtz, S. K.; Perry, T. T. *J. Appl. Phys.* **1968**, *39*, 3798.

14) Porter, Y.; Ok, K. M.; Bhuvanesh, N. S. P.; Halasyamani, P. S. *Chem. Mater.* **2001**, *13*, 1910.

15) Bray, T. H.; Albrecht-Schmitt, T. E. *unpublished results*.

16) Loefgren, P. *Acta Chem. Scand.* **1967**, *21*, 2781.

17) Sykora, R. E.; Wells, D. M.; Albrecht-Schmitt, T. E. *J. Solid State Chem.* **2002**, *166*, 442.

18) Ok, K. M.; Halasyamani, P. S. *Inorg. Chem.* **2005**, *44*, 2263.

19) Shehee, T. C.; Pehler, S. F.; Albrecht-Schmitt, T. E. *J. Alloys Compd*. **2005**, *388*, 225.

20) a) Opik, U.; Pryce, M. H. L.; *Proc. R. Soc.* (*London*) **1937**, *A161*, 220. b) Wheeler, R. A.; Whangbo, M. H.; Hughbanks, T.; Hoffman, R.; Burdett, J. K.; Albright, T. A. *J. Am. Chem. Soc.* **1986**, *108*, 2222. c) Pearson, R. G. *J. Mol. Struct.* **1983**, *103*, 25. d) Kang, S. K.; Tang, H.; Albright, T. A. *J. Am. Chem. Soc.* **1993**, *115*, 1971. e) Cohen, R. E. *Nature* **1992**, *358*, 136. f) Burdett, J. K. *Molecular Shapes*. Wiley-Interscience, New York, 1980. g) Kunz, M.; Brown, I.

D. *J. Solid State Chem.* **1995**, *115*, 395. h) Goodenough, J. B.; Longo, J. M.: *Crystallographic and magnetic properties of perovskite and perovskite-related compounds.* In *Landolt-Bornstein*; Hellwege, K. H.; Hellwege, A. M., Eds.; Springer-Verlag: Berlin, 1970; Vol.4, pp 126-314. i) Brown, I. D. *Acta Crystallogr*. **1977**, *B33*, 1305.

21) Burns, P. C.; Ewing, R. C.; Hawthorne, F. C. *Can. Mineral.* **1997**, *35*, 1551.

22) Brown, I. D.; Altermatt, D. *Acta Crystallogr*. **1985**, *B41*, 244.

23) Brese, N. E.; O'Keeffe, M. *Acta Crystallogr.* **1991**, *B47*, 192.

24) Abrahams, S. C.; Bernstein, J. L.; Elemans, J. B. A. A.; Verschoor, G. C. *J. Chem. Phys.* **1973**, *59*, 2007.

25) Burns, P. C.; Hawthorne, F. C. *Can. Mineral.* **1993**, *31*, 313.

26) Cooper, M. A.; Hawthorne, F. C.; Roberts, A. C.; Grice, J. D.; Stirling, J. A. R.; Moffatt, E. A. *Am. Mineral.* **1998**, *83*, 390.

27) Sykora, R. E.; Ok, K. M.; Halasyamani, P. S.; Albrecht-Schmitt, T. E. *J. Am. Chem. Soc.* **2002**, *124*, 1951. b) Shehee, T. C.; Sykora, R. E.; Ok, K. M.; Halasyamani, P. S.; Albrecht-Schmitt, T. E. *Inorg. Chem.* **2003**, *42*, 457. c) Halasyamani, P. S. *Chem. Mater.* **2004**, *16*, 3586 (and references therein). d) Sullens, T. A.; Almond, P. M.; Byrd, J. A.; Beitz, J. V.; Albrecht-Schmitt, T. E. *J. Solid State Chem.* **2006**, *179*, 1181. e) Ok, K. M.; Halasyamani, P. S. *Inorg. Chem.* **2005**, *44*, 9353. Ok, K. M.; Halasyamani, P. S. *Inorg. Chem.* **2005**, *44*, 2263. Ok, K. M.; Halasyamani, P. S. *Angew. Chem., Inter. Ed.* **2004**, *43*, 5489.

28) R. E. Sykora, K. M. Ok, P. S. Halasyamani, D. M. Wells, and T. E. Albrecht-Schmitt, *Chem. Mater.* **2002**, *14*, 2741.

CHAPTER 3

CRITICAL ROLE OF WATER CONTENT IN THE FORMATION AND REACTIVITY OF URANIUM, NEPTUNIUM, AND PLUTONIUM IODATES UNDER HYDROTHERMAL CONDITIONS: IMPLICATIONS FOR THE OXIDATIVE DISSOLUTION OF SPENT NUCLEAR FUEL

Reproduced with permission from Bray, T. H.; Ling, J.; Choi, E.-S.; Brooks, J. S.; Beitz, J. V.; Sykora, R. E.; Haire, R. G.; Stanbury, D. M.; Albrecht-Schmitt, T. E. *Inorg. Chem.* **2007**, *46*, 3663. Copyright 2007 American Chemical Society.

ABSTRACT

The reactions of $^{237}NpO_2$ with excess iodate under acidic hydrothermal conditions result in the isolation of the Np(IV), Np(V), and Np(VI) iodates, $Np(IO_3)_4$, $Np(IO_3)_4{\cdot}nH_2O{\cdot}nHIO_3$, $NpO_2(IO_3)$, $NpO_2(IO_3)_2(H_2O)$, and $NpO_2(IO_3)_2{\cdot}H_2O$, depending on both the pH and the amount of water present in the reactions. Reactions with less water and lower pH favor reduced products. While the initial redox processes involved in the reactions between $^{237}NpO_2$ or $^{242}PuO_2$ and iodate are similar, the low solubility of $Pu(IO_3)_4$ dominates product formation in Pu iodate reactions to a much greater extent than $Np(IO_3)_4$ does in the Np iodate system. UO_2 reacts with iodate under these conditions to yield U(VI) iodates solely. The isotypic structures of the An(IV) iodates, $An(IO_3)_4$ (An = Np, Pu) are reported and consist of one-dimensional chains of

dodecahedral An(IV) cations bridged by iodate anions. The structure of $Np(IO_3)_4 \cdot nH_2O \cdot nHIO_3$ is constructed from NpO_9 tricapped trigonal prisms that are bridged by iodate into a polar three-dimensional framework structure. Second-harmonic generation measurements on a polycrystalline sample of the Th-analog of $Np(IO_3)_4 \cdot nH_2O \cdot nHIO_3$ reveals a response of approximately 12× α-SiO_2. Single crystal magnetic susceptibility measurements of $Np(IO_3)_4$ show magnetically isolated Np(IV) ions.

INTRODUCTION

Under the oxidizing conditions present in the groundwater taken from wells near Yucca mountain, introduced iodine should occur in the form of both iodide, I^-, and iodate, IO_3^-.[1] Whereas I^- is not expected to form strong complexes with actinide ions in aqueous media,[2] IO_3^- forms stable, inner-sphere complexes with actinides.[3] The remarkable insolubility of actinide iodates has been used for decades to precipitate actinides selectively from fission products and other elements.[4] The initial form of actinides in spent nuclear fuel (SNF) are primarily reduced, e.g. UO_2, NpO_2, and PuO_2. Owing to its high vapor pressure, iodine is expected to be concentrated near the surface and in grain boundaries in SNF where it could react with dissolved oxygen in water to form iodate.[5] Therefore, the products of the reactions of tetravalent actinides with iodate might play an important role in the potential release of several key long-lived radionuclides (e.g. ^{129}I, $t_{½} = 1 \times 10^7$ y; ^{238}U, $t_{½} = 4.46 \times 10^9$ y; ^{237}Np, $t_{½} = 2.14 \times 10^6$ y, and ^{239}Pu, $t_{½} = 2.411 \times 10^4$ y) into the environment in the event of aged SNF contacting groundwater. During the lifetime of stored SNF, it is possible that minute cracks and

pores will form in the casings. This scenario will significantly limit the amount of groundwater interacting with the nuclear waste. Here, we show that the chemistry that occurs under hydrothermal conditions where a limited amount of water is present is dramatically different from what is predicted based on homogeneous solution redox potentials.[6]

EXPERIMENTAL

General Information. $Th(NO_3)_4 \cdot xH_2O$ (99%, Alfa Aesar), UO_2 (99.8%, Alfa Aesar, depleted), $^{237}NpO_2$ (99.9%, Oak Ridge, $t_{½} = 2.14 \times 10^6$ y), $^{242}PuO_2$ (99.9%, Oak Ridge, $t_{½} = 3.76 \times 10^5$ y), and HIO_3 (99.5%, Alfa Aesar) were used as received. Distilled and Millipore water with a resistance of 18.2 MΩ·cm was used in all reactions. Reactions were run in Parr 4749 autoclaves with custom-made 10-mL PTFE liners.

Actinide Iodate Synthesis. All reactions were conducted with 10 mg of AnO_2 (An = U, Np, or Pu) and a tenfold molar amount of iodic acid unless otherwise noted. For the Th reactions, $Th(NO_3)_4 \cdot xH_2O$ was used as the starting material. Sealed reaction vessels were placed in box furnaces that had been pre-heated to 200 °C. The reactions occurred under an air atmosphere. Cooling was accomplished by turning the furnaces off.

As a cautionary note, both $Np(IO_3)_4$ and $Pu(IO_3)_4$ are pleochroic owing to their low-dimensional structures. Different crystal growth conditions lead to changes in crystal morphology, agglomeration of crystallites, and different product coloration depending on the angle that the crystallites are viewed. For $Np(IO_3)_4$, grey to green to black transitions can be observed by rotating single crystals and clusters of crystals;

whereas for $Pu(IO_3)_4$, blue to green to brown coloration is exhibited. Crystals of $Np(IO_3)_4 \cdot nH_2O \cdot nHIO_3$ have a very pale yellow coloration. Crystals of $Th(IO_3)_4 \cdot nH_2O \cdot nHIO_3$ are colorless.

Crystallographic Studies. Single crystals of $An(IO_3)_4$ (An = Np and Pu) and $Np(IO_3)_4 \cdot nH_2O \cdot nHIO_3$ were optically aligned on a Bruker SMART APEX CCD X-ray diffractometer. For each crystal, intensity measurements were performed using graphite monochromated Mo Kα radiation from a sealed tube and a monocapillary collimator. SMART was used for preliminary determination of the cell constants and data collection control. The intensities of reflections of a sphere were collected by a combination of 3 sets of exposures (frames). Each set had a different ϕ angle for the crystal and each exposure covered a range of 0.3° in ω. A total of 1800 frames were collected.

The determination of integral intensities and global cell refinement were performed with the Bruker SAINT (v 6.02) software package using a narrow-frame integration algorithm. Numerical and semi-empirical absorption corrections were applied to the data.[7] The program suite SHELXTL (v 5.1) was used for spacegroup determination (XPREP), structure solution (XS), and refinement (XL).[8] The final refinement included anisotropic displacement parameters for all atoms. Some crystallographic details are listed in Table 3.1 for $An(IO_3)_4$ (An = Np and Pu) and $Np(IO_3)_4 \cdot nH_2O \cdot nHIO_3$. X-ray crystallographic files for $Np(IO_3)_4$, $Pu(IO_3)_4$, and $Np(IO_3)_4 \cdot nH_2O \cdot nHIO_3$ in CIF format.available free of charge via the Internet at http://pubs3.acs.org/acs/journals/supporting_ information.page?in_ manuscript= ic070170d.

Table 3.1. Crystallographic data for $Np(IO_3)_4$, $Pu(IO_3)_4$, and $Np(IO_3)_4 \cdot nH_2O \cdot nHIO_3$.

Formula	$Np(IO_3)_4$	$Pu(IO_3)_4$	$Np(IO_3)_4 \cdot nH_2O \cdot nHIO_3$
Formula mass (amu)	936.60	941.60	956.41
Crystal System	Tetragonal	Tetragonal	Rhombohedral
Space group	$P4_2/n$ (No. 86)	$P4_2/n$ (No. 86)	$R3c$
A (Å)	9.8790(5)	9.869(1)	21.868(1)
C (Å)	5.3063(4)	5.2861(7)	12.9705(8)
V (Å^3)	517.87(5)	514.8(1)	5371.4(5)
Z	2	2	18
T (°C)	-80	-80	-80
λ (Å)	0.71073	0.71073	0.71073
ρ_{calcd} (g cm^{-3})	6.006	6.074	5.322
μ(Mo $K\alpha$) (cm^{-1})	220.17	184.57	191.93
$R(F)$ for $F_o^2 > 2\sigma(F_o^2)$ [a]	0.0250	0.0266	0.0403
$R_w(F_o^2)$ [b]	0.0654	0.0467	0.0880

[a] $R(F) = \sum \left| |F_o| - |F_c| \right| / \sum |F_o|$. [b] $R_w(F_o^2) = \left[\sum \left[w(F_o^2 - F_c^2)^2 \right] / \sum w F_o^4 \right]^{1/2}$.

Magnetic Susceptibility Measurements performed by Eun Sang Choi and James S. Brooks, Department of Physics and National High Magnetic Field Laboratory, Florida State UniVersity, Tallahassee, Florida 32310. Magnetism data for $Np(IO_3)_4$ were measured with a Quantum Design MPMS 7T magnetometer-susceptometer between 2 and 300 K and in applied fields up to 7 T. DC temperature dependent susceptibility measurements were made under zero-field-cooled conditions with an applied field of 0.1 T. Susceptibility values were corrected for the sample diamagnetic contribution according to Pascal's constants,[9] as well as for the sample holder diamagnetism.

Nonlinear Optical Measurements performed by James V. Beitz, Chemistry Division, Argonne National Laboratory, Argonne, Illinois 60439. Powder second-harmonic generation (SHG) measurements were performed on a Kurtz-Perry nonlinear optical system,[10] as modified by Porter and coworkers,[11] and updated here to include laser pulse energy normalization. A Q-switched Nd:YAG laser (Continuum Surelite I-10), operated at 10 Hz, provided the 1064 nm light used for all measurements. The SHG intensity was recorded from $Th(IO_3)_4 \cdot nH_2O \cdot nHIO_3$ and from fine ground α-quartz. These powders were placed in separate glass tubes of the same dimensions. No index of refraction matching fluid was used in these experiments. The SHG light at 532 nm was collected in reflection, selected by a narrow band-pass interference filter (Pomfret) and detected by a photomultiplier tube (RCA 1P28). A near normal incidence beam splitter reflected a small fraction of the laser beam onto a pyroelectric detector (Molectron J3-05) that was used as a laser pulse energy monitor. A digital storage oscilloscope (Tektronix TDS 640A) signal averaged and recorded both the SHG and incident laser energy signals.

Average laser power was measured separately with a calibrated Scientech volume absorber calorimeter. The observed SHG intensity per unit laser intensity, $I^{2\omega}$, was obtained by dividing the SHG signal by the laser energy signal. Replicate measurements determined the value of interest for the sample compound, $I^{2\omega}$ (s), and for α-quartz, $I^{2\omega}$ (q). The ratio of these values, $I^{2\omega}$ (s) / $I^{2\omega}$ (q), was found to be 12 at an incident laser intensity of 6.7 MW/cm^2.

RESULTS AND DISCUSSION

Reactions. When $^{237}NpO_2$ is reacted with excess iodate under acidic mild hydrothermal conditions, Np(IV), Np(V), and Np(VI) iodates are isolated as is shown in Scheme 3.1. Reaction 1 describes the direct two-electron oxidation of Np^{4+} to NpO_2^{2+} by iodate. Acidic dissolution of NpO_2 in the presence of oxygen typically yields Np(V) in the form of NpO_2^+ in solution (e.g. in 1 M HCl). Reaction 1 is governed by the strong oxidizing potential of iodate under acidic conditions that is sufficient to directly oxidize Np^{4+} to NpO_2^{2+}.[6] The formal potentials for these reactions are given below in Scheme 3.2.[6,12] It is important to note that these E° values are given at 25 °C and 1 atm. Our reactions are occurring at 200 °C and approximately 17 atm (if H_2O exhibits the vapor pressure of pure water), and therefore these potentials can only be used for guidance. These reactions should be thought of as taking place in steam under autogenously generated pressure. There is approximately 170 μL of liquid water present at 200 °C in a reaction that starts with 250 μL of water. In contrast, there will only be 20 μL of liquid water present at 200 °C in a reaction that begins with 100 μL of water. When the reactions occur with only a limited amount of liquid water present, as is demonstrated in

Reactions 2 and 7, reduction of NpO_2^{2+} back to Np^{4+} takes place. When sufficient amounts of water are present to approximate a solution (500 μL), as in Reaction 6, the predicted reaction between NpO_2 and iodate occurs, via Reaction 1, and $NpO_2(IO_3)_2(H_2O)$ and $NpO_2(IO_3)_2 \cdot H_2O$ form.[13] Reaction 5 is the most interesting of this series, and represents conditions under which comproportionation of Np^{4+} and NpO_2^{2+} occurs to yield two equivalents of NpO_2^{+}. It is important to note that even when the Np(VI) products are isolated as solids, they can be slowly converted to Np(IV) iodates by the application of appropriate hydrothermal conditions (250 μL water), as is shown in Reaction 7. If the amount of water is increased to 500 μL, reduction does not take place.

Scheme 3.1.

$$5NpO_2 + 12H^+ + 2IO_3^- \xrightarrow[H_2O]{200\,^\circ C,\ 3\ d} 5NpO_2^{2+} + I_2 + 6H_2O \quad (1)$$

$$2NpO_2^{2+} + 4H^+ \xrightarrow[<375\ \mu L\ H_2O]{200\,^\circ C,\ 3\ d} 2Np^{4+} + 2H_2O + O_2 \quad (2)$$

$$Np^{4+} + 4IO_3^- \xrightarrow[100\ \mu L\ H_2O]{200\,^\circ C,\ 3\ d} Np(IO_3)_4 \quad (3)$$

$$2Np^{4+} + 8IO_3^- + nH_2O \xrightarrow[250\ \mu L\ H_2O]{200\,^\circ C,\ 3\ d} Np(IO_3)_4 + Np(IO_3)_4 \cdot nH_2O \quad (4)$$

$$NpO_2^{2+} + Np^{4+} + 2IO_3^- + 2H_2O \xrightarrow[375\ \mu L\ H_2O]{200\,^\circ C,\ 3\ d} 2NpO_2(IO_3) + 4H^+ \quad (5)$$

$$2NpO_2^{2+} + 4IO_3^- + 2H_2O \xrightarrow[500\ \mu L\ H_2O]{200\,^\circ C,\ 3\ d} NpO_2(IO_3)_2 \cdot H_2O + NpO_2(IO_3)_2(H_2O) \quad (6)$$

$$2H^+ + NpO_2(IO_3)_2 \cdot H_2O + 2IO_3^- \xrightarrow[250\ \mu L\ H_2O]{200\,^\circ C,\ 30\ d} Np(IO_3)_4 + 2H_2O + 1/2O_2 \quad (7)$$

Scheme 3.2

$$Np^{4+} \xleftarrow{0.60\ V} NpO_2^{+} \xleftarrow{1.16\ V} NpO_2^{2+} \qquad (0.88\ V)$$

$$2IO_3^- + 12H^+ + 10e^- \xrightarrow{1.195\ V} I_2 + 6H_2O$$

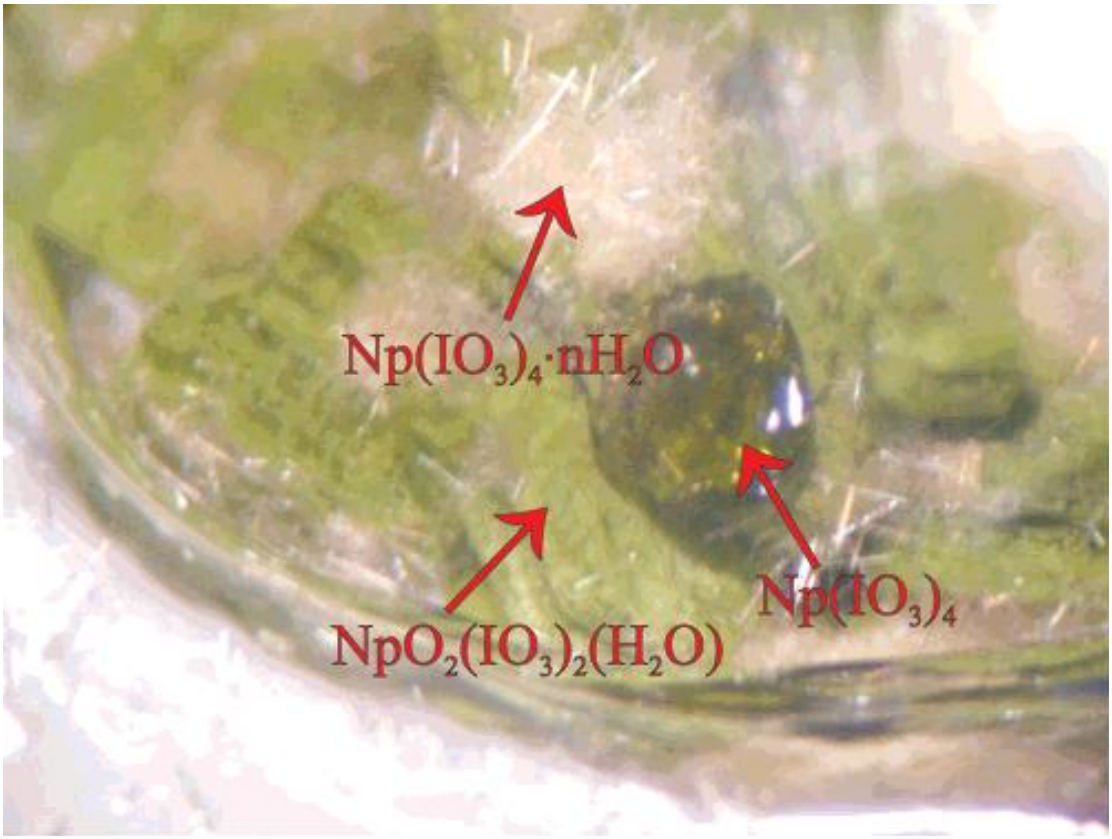

Figure 3.1. Photograph showing the hydrothermal reduction of the neptunium(VI) iodate $NpO_2(IO_3)_2(H_2O)$ to the neptunium(IV) iodates $Np(IO_3)_4$ and $Np(IO_3)_4{\cdot}nH_2O{\cdot}nHIO_3$.

Reactions 2–4 are not solely driven by the solution phase thermodynamics of the oxidation of Np^{4+} by iodate, but also by the reduction of Np(VI) to yield Np(IV), and the subsequent crystallization of the Np(IV) iodate products, $Np(IO_3)_4$ and $Np(IO_3)_4{\cdot}nH_2O{\cdot}nHIO_3$. Figure 3.1 depicts the results of Reaction 7, and shows crystals of $Np(IO_3)_4$ and $Np(IO_3)_4{\cdot}nH_2O{\cdot}nHIO_3$ that have grown directly off of the surface of delaminating crystals of $NpO_2(IO_3)_2(H_2O)$. This result supports the hypothesis that the reaction is a solid-to-solid transformation that is probably surface-mediated. The same may be true for Reactions 2–5. In the presence of a large external radiation source, radiolysis products of water (e.g. H, HO_2, and H_2O_2) might play a role in the reduction of Np(VI) to Np(IV).[14] As was observed with Np, the reaction of PuO_2 with iodate leads to the two-electron oxidation of Pu^{4+} to PuO_2^{2+} with concomitant production of elemental iodine (Scheme 3.3, Reaction 8). In contrast to the $^{237}NpO_2$ reactions, the reaction of $^{242}PuO_2$ with iodate with up to 1000 μL of water lead to the formation of $Pu(IO_3)_4$ (Scheme 3.3, Reaction 9). These results imply that the hydrothermal chemistry of Pu iodates is dominated to an even greater extent than in the Np reactions by the solubility-driven formation of the An(IV) iodates.

Scheme 3.3

$$5PuO_2 + 12H^+ + 2IO_3^- \xrightarrow[H_2O]{200\ ^\circ C,\ 3\ d} 5PuO_2^{2+} + I_2 + 6H_2O \qquad (8)$$

$$Pu^{4+} + 4IO_3^- \xrightarrow[100\text{-}1000\ \mu L\ H_2O]{200\ ^\circ C,\ 3\ d} Pu(IO_3)_4 \qquad (9)$$

$$5UO_2 + 12H^+ + 2IO_3^- \xrightarrow[H_2O]{200\ ^\circ C,\ 3\ d} 5UO_2^{2+} + I_2 + 6H_2O \qquad (10)$$

$$2UO_2^{2+} + 4IO_3^- + H_2O \xrightarrow[H_2O]{200\ ^\circ C,\ 3\ d} UO_2(IO_3)_2(H_2O) + UO_2(IO_3)_2 \qquad (11)$$

In previous work, it was shown that stock solutions of Pu^{4+} and NpO_2^+ react with excess metaperiodate, IO_4^-, to yield products containing the actinides in the +6 oxidation state (e.g. $NpO_2(IO_3)_2(H_2O)$ and $AnO_2(IO_3)_2 \cdot H_2O$ (An = Np, Pu)).[13,15] Metaperiodate contains I(VII), and is a much stronger oxidant than iodate (1.601 V vs. 1.195 V). Clearly, the reactions reported herein of AnO_2 (An = Np, Pu) with iodate under hydrothermal conditions with limited amounts of water are dramatically different fromthose of aqueous actinide ions with very strong oxidants. While these reactions are occurring at a much lower pH than natural groundwaters, this work calls into question the the use of standard solution reactivity data on actinide ions to predict the behavior of SNF that will start off as a reduced solid. The thermodynamic data for actinide complexation are already being reevaluated in light of the substantial changes that occur at elevated temperatures.[16]

The least complex of these reactions is that of UO_2 with iodate. The process proceeds in accordance with Scheme 3.3, reactions 10 and 11, yielding only U(VI) iodates, such as $UO_2(IO_3)_2$ and $UO_2(IO_3)_2(H_2O)$.[17] Given the ease of oxidation of U^{4+} to UO_2^{2+}, this result is not surprising ($E° = -0.327$ V).[6]

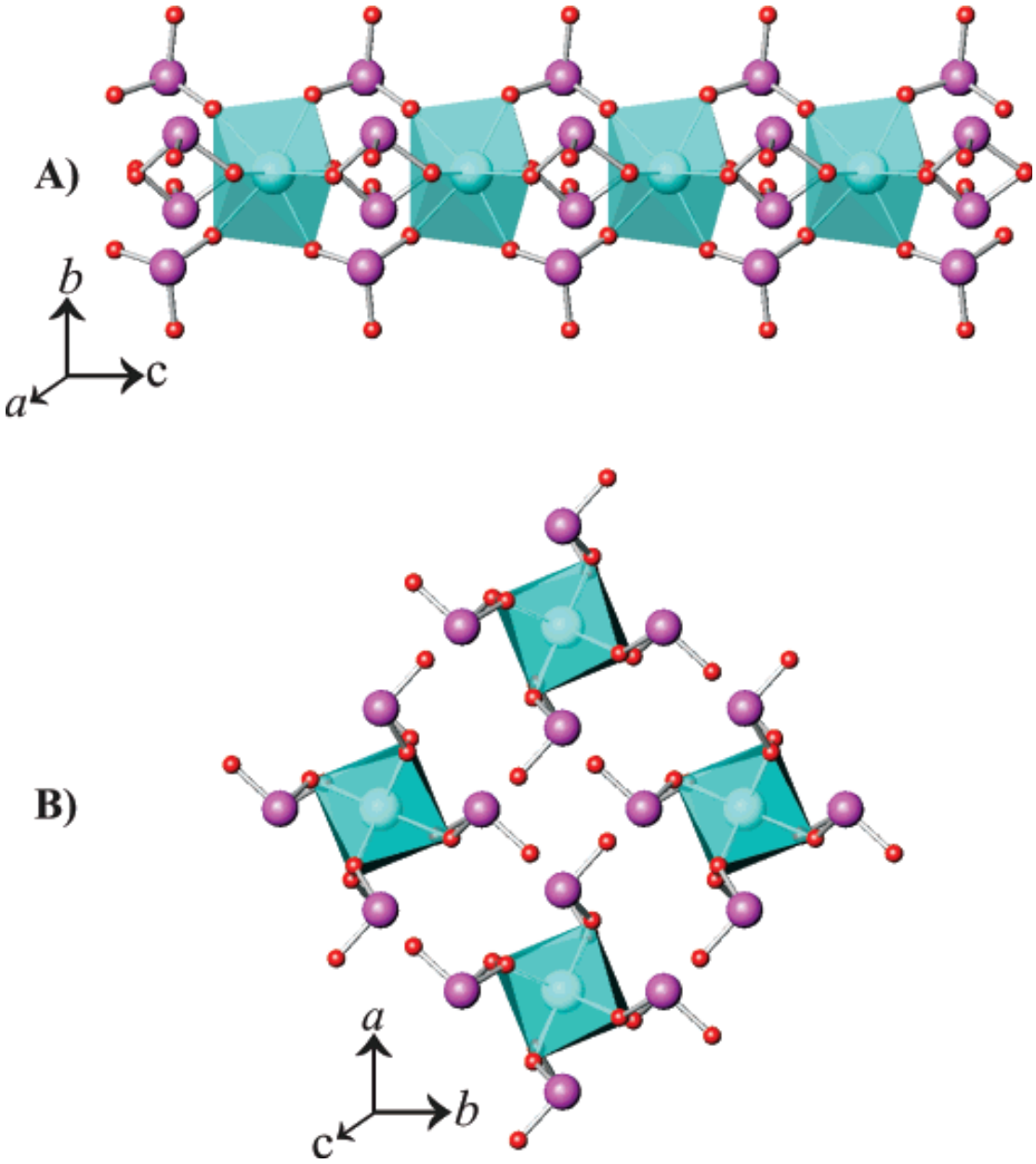

Figure 3.2. (a) View of the one-dimensional chains in $An(IO_3)_4$ (An = Np, Pu) consisting of eight-coordinate, dodecahedral An(IV) centers bridged by iodate. (b) Depiction of the pinwheel packing of the $An(IO_3)_4$ chains.

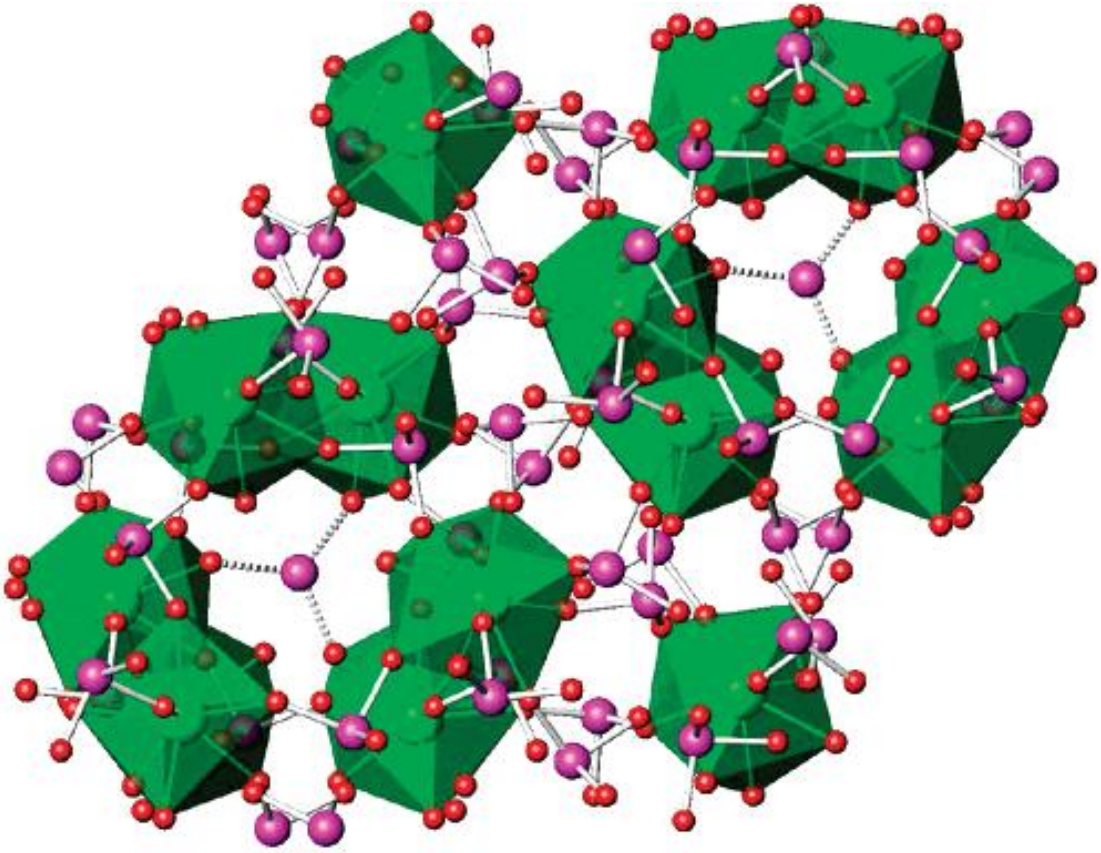

Figure 3.3. Depiction of the structure of $Np(IO_3)_4 \cdot nH_2O \cdot nHIO_3$. This structure consists of a three-dimensional network constructed from nine coordinate tricapped trigonal prismatic Np(IV) that are bridged by iodate anions to create the channels that extend along the *c* axis. The channels are partially filled by iodate anions or water molecules.

Structure of $An(IO_3)_4$ (An = Np and Pu). In addition to the new actinide reactivity patterns, these syntheses provide access to single crystals of $An(IO_3)_4$ (An = Np and Pu) and $Np(IO_3)_4 \cdot nH_2O \cdot nHIO_3$. The crystal structure of $An(IO_3)_4$ (An = Np and Pu) consists of eight-coordinate, trigonal dodecahedral An(IV) centers (D_{2d}) bridged by iodate to form one-dimensional chains as is shown in Figure 3.2a. These compounds are isostructural with $Ce(IO_3)_4$.[18] The Np centers reside on $\bar{4}$ sites yielding two independent An–O bond distances of 2.329(4) Å (×4) and 2.358(4) Å (×4) (for $Np(IO_3)_4$). The I–O bond distances of 1.782(5), 1.811(4), and 1.827(4) Å are normal.[17] The terminal I–O bond distance is slightly shorter than those bridging to the Np(IV) ions. These chains pack together in a pin-wheel fashion (Figure 3.2b). While the structures of Np(IV) iodates are expected to be similar, if not identical, with those of Th(IV), we have yet to isolate a Th-analog of $An(IO_3)_4$ (An = Np, Pu), although the Ce(IV) version has been prepared, underscoring some of the problems of using early, less radioactive actinides like Th(IV) and U(IV) as surrogates for Np(IV) and Pu(IV).[20] This was also observed in the An(VI) iodates, where the U(VI) and Pu(VI) compounds are not isostructural.[13,15,17]

Structure of $Np(IO_3)_4 \cdot nH_2O \cdot nHIO_3$. The structure of $Np(IO_3)_4 \cdot nH_2O \cdot nHIO_3$ is isometric with $K_3Am_3(IO_3)_{12} \cdot HIO_3$,[21] although the chemical formula and Z values are expressed differently. This structure-type consists of a three-dimensional network constructed from nine-coordinate tricapped trigonal prismatic An(III) or An(IV) centers bridged by iodate anions to create a channel structure, as is shown in Figure 3.3. The channels are partially filled by iodate anions or water molecules. Although the structure of $K_3Am_3(IO_3)_{12} \cdot HIO_3$ was reported as being stoichiometric, refinement on the occupancy of the iodate units in the channels reveals that they are only partially occupied.

Furthermore, there are three very long I−O bonds of ca. 1.9 Å to this partially occupied iodine atom. We have prepared the Ce-analog of $K_3Am_3(IO_3)_{12}{\cdot}HIO_3$,[100] and it shows partial occupancy of the iodine atoms in the channels, disorder and partial occupancy of the K^+ sites, and mixed-valency (Ce(III)/Ce(IV)). Clearly something unusual is taking place in this series of compounds associated with the iodate groups in the channels.

$K_3Am_3(IO_3)_{12}{\cdot}HIO_3$ is reported as crystallizing in the polar rhombohedral space group *R*3*c*.[21] Confirmation of the polarity of the space group via some external measurement, e.g. second-harmonic generation, is quite challenging given the extreme radioactivity of ^{241}Am. While ^{237}Np is substantially less radioactive than ^{241}Am, it nevertheless poises serious handling challenges. Fortunately, as the result of separate studies, the Th-analog of $Np(IO_3)_4{\cdot}nH_2O{\cdot}nHIO_3$ was prepared, and second-harmonic generation measurements were performed that showed a response of approximately 12× α-quartz, confirming the acentricity of the structure.

An unusual type of disorder to explain the abnormal bond distances and partial occupancy in this family of compounds is proposed here based on the following data: 1) the ninth capping position (O(13)) around the NpO_9 units appears to be fully occupied. 2) The atom lying at the center of the channels refines best as a partially occupied iodine. 3) The displacement parameters for O(13) are large (all light atoms were refined isotropically in $K_3Am_3(IO_3)_{12}{\cdot}HIO_3$). Taken together a model can be proposed where the channels are either occupied by iodate or only by the capping water molecules. This would create an oxygen position (O(13)) that is an average of the water position(s) and the position(s) of the oxygen atoms from the iodate unit.

The Np−O bond distances range from 2.296(13) to 2.68(12) Å; the longest distance is to the coordinating water molecules in the channels. The four ordered iodate anions that are a part of the three-dimensional network contain regular I−O bond distances that range from 1.781(12) to 1.827(13) Å. All other aspects of the structure are also normal.

Magnetic Properties of $Np(IO_3)_4$. $Np(IO_3)_4$ crystallizes as single crystals that can have maximum dimensions as large as several millimeters, making this compound amenable to single-crystal magnetic susceptibility measurements. Magnetic susceptibility data for $Np(IO_3)_4$ are shown in Figure 3.4. Data were collected on two different crystals yielding μ_{eff} of 2.22 and 2.25 μ_B per Np atom for the different crystals. The observed magnetic moment for the Np^{4+} ions in $Np(IO_3)_4$ is markedly lower than that calculated for the free-ions (3.62 μ_B).[22] This is not a reflection of covalency of the 5f orbitals, but rather arises from crystal field effects in $Np(IO_3)_4$,[23] as has also been suggested recently for two Np(V) compounds.[24] Magnetic fields well outside of the range of a standard 7 T magnet would be needed to achieve full saturation of the magnetic moment.[23] The data follow the Curie-Weiss law with θ = 0.0(5) K, indicating that the Np(IV) ions are magnetically isolated from one another. This observation is consistent with the large Np···Np distance of 5.306(1) Å within the one-dimensional chains.

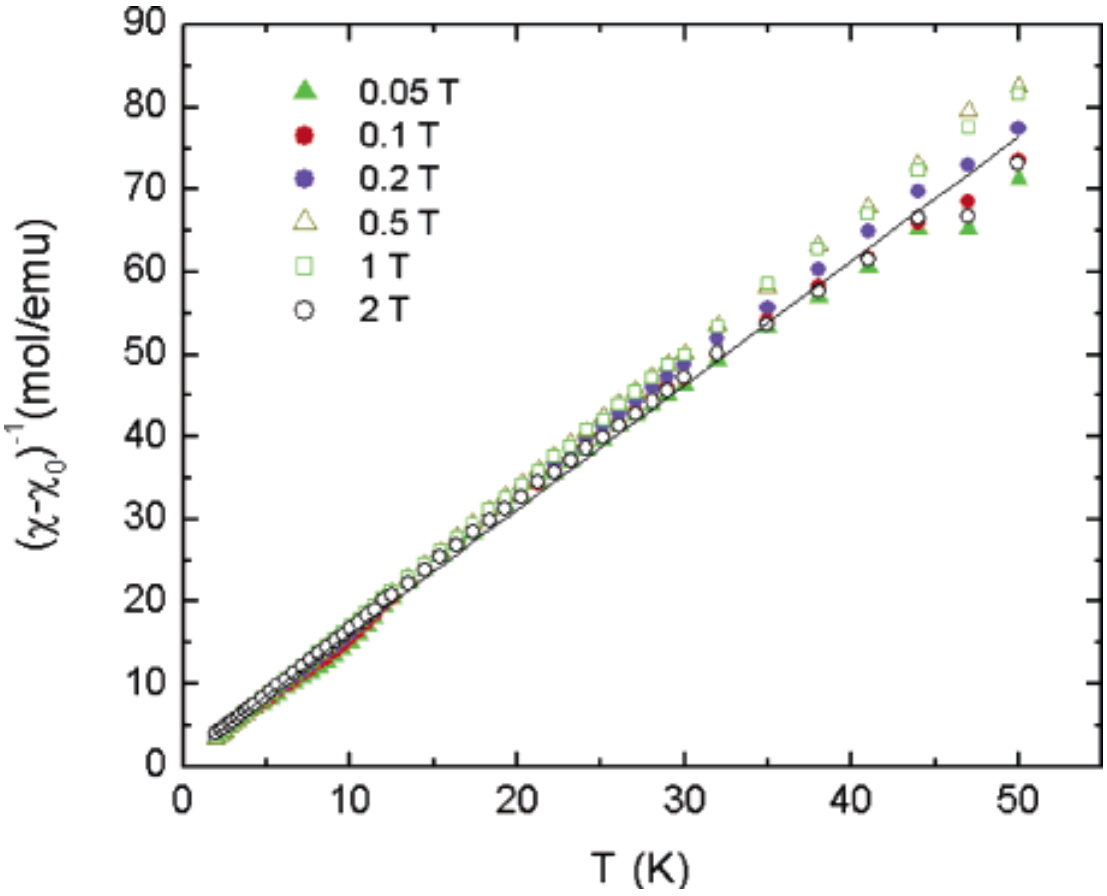

Figure 3.4. Temperature dependence of the inverse magnetic susceptibility of a $Np(IO_3)_4$ single crystal. The Curie-Weiss fitting curve is shown as a solid line.

REFERENCES

1) a) Bruchertseifer, H.; Cripps, R.; Guentay, S.; Jaeckel, B. *Anal. Bioanal. Chem.* **2003**, *375*, 1107. b) Huang, Z.; Ito, K.; Timerbaev, A. R.; Hirokawa, T. *Anal. Bioanal. Chem.* **2004**, *378*, 1836. c) Bard, A. J.; Parsons, R.; Jordan, J. *Standard Potentials in Aqueous Solution*, Dekker, New York, 1985. d) Charlot, G. *Oxidation-Reduction Potentials*, Pergamon, London, 1958. e) Pourbaix, M. *Atlas d'equilibries electrochemiques à 25 °C*, Gautier Villars, Paris, 1963.

2) Crawford, M.-J.; Ellern, A.; Karaghiosoff, K.; Mayer, P. Noth, H.; Suter, M. *Inorg. Chem.* **2004**, *43*, 7120.

3) a) Choppin, G. R.; Khalili, F. I.; Rizkalla, E. N. *J. Coord. Chem.* **1992**, *26*, 243. b) Rao, P. R. V.; Patil, S. K. *Radiochem. Radioanal. Lett.* **1978**, *36*, 169.

4) a) Seaborg, G. T.; Wahl, A. C. *J. Am. Chem. Soc.* **1948**, *70*, 1128. b) Cunningham, B. B.; Werner, L. B. *J. Am. Chem. Soc.* **1949**, *71*, 1521. c) Seaborg, G. T.; Thompson, S. G. U.S. Patent #2,950,168, 1960.

5) Kaholek, M.; Triendl, L. *React. Kinet. Catal. Lett.* **1998**, *63*, 297.

6) a) Morss, L. R.; Edelstein, N. M.; Fuger, J. *The Chemistry of the Actinide and Transactinide Elements* (Springer, Heidelberg, 2006), vol. 2, Ch. 6. b) Katz, J. J.; Seaborg, G. T.; Morss, L. R. *The Chemistry of the Actinide Elements* (Chapman and Hall, New York, ed 2, 1986), vol. 1, Ch. 6.

7) Sheldrick, G. M. *SADABS* 2001, Program for absorption correction using SMART CCD based on the method of Blessing: Blessing, R. H. *Acta Crystallogr.* **1995**, *A51*, 33.

8) Sheldrick, G. M. SHELXTL PC, Version 6.12, An Integrated System for Solving, Refining, and Displaying Crystal Structures from Diffraction Data; Siemens Analytical X-Ray Instruments, Inc.: Madison, WI 2001.

9) Mulay, L. N.; Boudreaux, E. A. *Theory and Applications of Molecular Diamagnetism*; Wiley–Interscience: New York, 1976.

10) Kurtz, S. K.; Perry, T. T. *J. Appl. Phys.* **1968**, *39*, 3798.

11) Porter, Y.; Ok, K. M.; Bhuvanesh, N. S. P.; Halasyamani, P. S. *Chem. Mater.* **2001**, *13* 1910.

12) Lide, D. R. *CRC Handbook of Chemistry and Physics*, 71st Ed., CRC Press, Boston, 1990, pp 8-18.

13) Bean, A. C.; Scott, B. L.; Albrecht-Schmitt, T. E.; Runde, W. *Inorg. Chem.* **2003**, *42*, 5632.

14) Vladimirova, M. V. *Radiochem.* **1997**, *39*, 250.

15) Runde, W.; Bean, A. C.; Albrecht-Schmitt, T. E.; Scott, B. L. *Chem. Commun.* **2003**, *4*, 478.

16) Rao, L.; Srinivasan, T. G.; Garnov, A. Y.; Zanonato, P. L.; Di Bernardo, P.; Bismondo, A. *Geochim. Cosmochim. Acta* **2004**, *68*, 4821.

17) a) Weigel, F.; Engelhardt, L. W. H. *J. Less-Common Met.* **1983**, *91*, 339. b) Bean, A. C.; Peper, S. M.; Albrecht-Schmitt, T. E. *Chem. Mater.* **2001**, *13*, 1266.

18) a) Staritsky, E.; Cromer, D. T. *Anal. Chem.* **1956**, *28*, 913. b) Cromer, T.; Larson, A. C. *Acta Cryst.* **1956**, *9*, 1015.

19) a) Sullens, T. A.; Almond, P. M.; Albrecht-Schmitt, T. E. *Mater. Res. Soc.* **2006**, *893*, 283. b) Gorden, A. E. V.; Shuh, D. K.; Tiedemann, B. E. F.; Wilson, R. E.; Xu, J.; Raymond, K. N. *Chemistry*, **2005**, *11*, 2842.

20) A historical footnote is worthwhile here: The microscale precipitation of $Pu(IO_3)_4$ was used by B. B. Cunningham and L. B. Werner to show, for the first time, that Pu has a stable +4 oxidation state in 1942 (*3b*). Since this time $Pu(IO_3)_4$ has been used as a benchmark compound because of its remarkable insolubility in low pH media. The structure, precise elemental analyses, and spectroscopic data for Pu(IV) iodates has never been reported in the primary literature. We believe that the compound referred to in the past as $Pu(IO_3)_4$ is in fact $Pu(IO_3)_4 \cdot nH_2O \cdot nHIO_3$, and not the anhydrous $Pu(IO_3)_4$.

21) Runde, W.; Bean, A. C.; Scott, B. L. *Chem. Comm.* **2003**, *15*, 1848.

22) Kittel, C. *Introduction to Solid State Physics*, 6th Ed., Wiley, New York, 1986.

23) a) Morss, L. R.; Edelstein, N. M.; Fuger, J. *The Chemistry of the Actinide and Transactinide Elements*, Springer, Heidelberg, vol. 4, Ch. 20, 2006.

24) Forbes, T. Z.; Burns, P. C.; Soderholm, L.; Skanthakumar, S. *Chem. Mater.* **2006**, *18*, 1643.

25) See for example: Grohol, D.; Matan, K.; Cho, J.-H.; Lee, S.-H.; Lynn, J. W.; Nocera, D. G.; Lee, Y. S. *Nat. Mat.* **2005**, *4*, 323.

26) Unpublished results.

CHAPTER 4

HYDROTHERMAL SYNTHESIS, STRUCTURE, AND MAGNETIC PROPERTIES OF $Pu(SeO_3)_2$

Reproduced with permission from Bray, Travis H.; Skanthakumar, S.; Soderholm, L.; Sykora, Richard E.; Haire, Richard G.; Albrecht-Schmitt, Thomas E. *J. Solid State Chem.* **2008**, *181*, 493-498. Copyright 2008 Elsevier.

ABSTRACT

The reaction between PuO_2 and SeO_2 under mild hydrothermal conditions results in the formation of $Pu(SeO_3)_2$ as brick-red prisms. This compound adopts the $Ce(SeO_3)_2$ structure type, and consists of one-dimensional chains of edge-sharing [PuO_8] distorted bicapped trigonal prisms linked by [SeO_3] units into a three-dimensional network. Crystallographic data: $Pu(SeO_3)_2$, monoclinic, space group $P2_1/n$, a = 6.960(1), b = 10.547(2), c = 7.245(1) Å, β = 106.880(9), V = 508.98(17), Z = 4 (T = 193 K), R(F) = 2.92% for 83 parameters with 1140 reflections with $I > 2\sigma(I)$. Magnetic susceptibility data for $Pu(SeO_3)_2$ are linear from 35-320 K and yield an effective moment of 2.71(5) μ_B and a Weiss constant of -500(5) K.

INTRODUCTION

The recent resurgence in the structural chemistry of transuranium compounds has brought to light notable differences between the bonding in early actinides and later

actinides, as well as discrepancies between these elements and non-radioactive surrogates, e.g. Ce^{4+}. At issue is whether or not transuranium element behavior can be modeled by the lanthanides and early actinides. Notable examples of divergence between the behaviors of these two groups includes $PuO_2(IO_3)_2 \cdot H_2O$,[1] whose structure differs substantially from $UO_2(IO_3)_2(H_2O)$,[2] and [Pu{5LIO(Me-3,2-HOPO)}$_2$] (5LIO designating that the HOPO ligands connect to either end of an diethyl ether chain, *i.e.*, -CH_2-CH_2-O-CH_2-CH_2),[3] which is not isostructural with its Ce^{4+} analog.[4] As a part of ongoing investigations concerning the structures and properties of actinide materials containing oxoanions with a non-bonding, but stereochemically active lone-pair of electrons,[5] the Pu^{4+} selenite, $Pu(SeO_3)_2$, has been prepared here and its structure compared with that of $Ce(SeO_3)_2$.[6]

Unlike Ce^{4+}, which has a $4f^0$ electron configuration, Pu^{4+} is $5f^4$, and the magnetic susceptibility of $Pu(SeO_3)_2$ is therefore included in this report. The simplest approach appropriate to modeling the magnetic behavior of valence f-states is the Russell-Saunders coupling scheme, which for the f^4 configuration predicts a $^5I_4$ ground level. Although this scheme works well for 4f electrons, configuration mixing, intermediate coupling, and bonding considerations all contribute complexity to the accurate representation of 5f wavefunctions under a crystal-field potential. In addition, the magnitude of the crystal-field may influence the temperature dependence of the susceptibility either through the energy of low lying excited states or through second-order effects that result in temperature-independent paramagnetism.[17, 18] There is simply too little known about the magnetic properties of Pu(IV) compounds to begin to untangle these complexities.[7,8] It is expected that the magnetic behavior of $Pu(SeO_3)_2$ will extend the available examples of

the magnetic response in a structurally well characterized 5f compound and, together with a variety of similar results, may provide the experimental basis upon which to extend our theoretical understanding of magnetic coupling.

EXPERIMENTAL

General Information. $^{242}PuO_2$ (99.9%, Oak Ridge National Laboratory) and SeO_2 (Alfa-Aesar, 9.4%) were used as received. Reactions were run in PTFE-lined Parr 4749 autoclaves with a 10 mL volume. Distilled and Millipore filtered water with a resistance of 18.2 MΩ·cm was used in the reactions. All studies were conducted in a laboratory dedicated to working with transuranium elements, located in a nuclear science facility, and equipped with HEPA filtered hoods and gloveboxes that are ported directly into the hoods. Counters continually monitor radiation levels in the lab. The lab is licensed by the state of Alabama (a NRC compliant state) and Auburn University's Radiation Safety Office. All experiments were carried out with approved safety operating procedures. All free-flowing solids are handled in the gloveboxes and solid products are only examined externally after coating with either water or Krytox oil and water.

$Pu(SeO_3)_2$ Synthesis. PuO_2 (10 mg, 0.036 mmol), SeO_2 (8 mg, 0.072 mmol), and 250 μL of water were loaded in a 10 mL PTFE-lined autoclave. The autoclave was sealed and placed in a preheated furnace for 3 d at 200 °C and then cooled at 9 °C/h to 23 °C. The product consisted of brick-red prisms of $Pu(SeO_3)_2$.

Crystallographic Studies. A single crystal of $Pu(SeO_3)_2$ was mounted on a glass fiber with epoxy, and optically aligned on a Bruker APEX CCD X-ray diffractometer using a digital camera. Intensity measurements were performed using graphite monochromated

Mo Kα radiation from a sealed tube and monocapillary collimator. SMART (v 5.624) was used for initial determination of the cell constants and for data collection control. The intensities of reflections of a sphere were collected by a combination of 3 sets of exposures (frames). Each set had a different ϕ angle for the crystal and each exposure covered 0.3° in ω. A total of 1800 frames were collected with an exposure time per frame of 30 s. Determination of integrated intensities and global refinement were performed with the Bruker SAINT (v 6.02) software package using a narrow-frame integration algorithm. A face-indexed numerical absorption correction was initially applied using XPREP.[9] Individual shells of unmerged data were corrected and exported in the same format. These files were subsequently treated with a semi-empirical absorption correction by SADABS.[10] The program suite SHELXTL (v 6.12) was used for space group determination (XPREP), direct methods structure solution (XS), and least-squares refinement (XL).[9] The final refinements included anisotropic displacement parameters for all atoms. Selected crystallographic details are given in Table 4.1. Table 4.2 shows the atomic coordinates and equivalent isotopic displacement parameters for $Pu(SeO_3)_2$. Further details of the crystal structure investigation may be obtained from the Fachin-formationzentrum Karlsruhe, D-76344 Eggenstein-Leopoldshafen, Germany (Fax: (+49)7247-808-666; Email: crysdata@fiz-karlsruhe.de) on quoting the depository number CSD 418050.

Magnetic Studies were performed by S. Skanthakumar and Lynne Soderholm, Chemistry Division, Argonne National Laboratory, Argonne, Illinois 60439. The magnetic susceptibility data were collected on a 18.3 mg powdered sample of $Pu(SeO_3)_2$ using a Quantum Design MPMS 7 SQUID magneto-meter. Due to the

Table 4.1. Crystallographic Data for $Pu(SeO_3)_2$.

Formula	$Pu(SeO_3)_2$
Formula Mass	495.92
Color and habit	brick-red prism
Crystal System	monoclinic
Space group	$P2_1/n$ (No. 14)
a (Å)	6.960(1)
b (Å)	10.547(2)
c (Å)	7.245(1)
β (°)	106.880(9)
V (Å^3)	509.0(2)
Z	4
T (K)	193
λ (Å)	0.71073
Maximum 2θ (deg.)	56.66
ρ_{calcd} (g cm^{-3})	6.472
μ(Mo $K\alpha$) (cm^{-1})	272.04
Number of Reflections	4689
Independent Reflections	1240
Data/restraints/parameters	1240/0/83
$R(F)$ for $F_o^2 > 2\sigma(F_o^2)$[a]	0.0292
$R_w(F_o^2)$[b]	0.0730

[a] $R(F) = \sum \left| |F_o| - |F_c| \right| / \sum |F_o|$. [b] $R_w\left(F_o^2\right) = \left[\sum \left[w\left(F_o^2 - F_c^2\right)^2 \right] / \sum wF_o^4 \right]^{1/2}$.

Table 4.2. Atomic coordinates and equivalent isotopic displacement parameters for $Pu(SeO_3)_2$.

Atom(site)	x	y	z	U_{eq} ($Å^2$)[a]
Pu(1)	0.25883(3)	0.09623(2)	0.01252(3)	0.00790(13)
Se(1)	0.23680(8)	0.28285(6)	0.42993(10)	0.00841(17)
Se(2)	0.27828(9)	-0.06979(6)	-0.43640(10)	0.00948(17)
O(1)	0.1430(6)	0.2422(4)	0.1989(7)	0.0133(9)
O(2)	0.4052(7)	0.4004(4)	0.4126(8)	0.0114(10)
O(3)	0.0711(7)	0.3964(4)	0.4570(7)	0.0116(10)
O(4)	0.1842(6)	0.0213(4)	-0.2898(7)	0.0124(9)
O(5)	0.5261(7)	-0.0904(4)	-0.3172(8)	0.0128(10)
O(6)	0.1928(7)	-0.2142(4)	-0.3938(7)	0.0164(10)

radiological hazards of ^{242}Pu, the sample was doubly encapsulated in a sealed aluminum holder that contributed significantly (up to 80%) to the measured signals. Empty Al sample holders were measured separately under identical conditions and their magnetic response was subtracted directly from the raw data. Experiments under variable temperatures were carried out between 5 and 320 K under applied fields of 0.5, 2, 5, and 10 kOe. Field measurements, up to 10 kOe, were carried out at 5 and 300 K and revealed a non-linearity to the measured signal as a function of field below about 2000 Oe. The susceptibility was corrected by removing the diamagnetic contribution of the sample from the raw data.

The magnetization of $Pu(SeO_3)_2$ is non-linear with field at fields lower than about 2 kOe. In addition, the measured susceptibility as a function of temperature (M/H) has a field-dependent component, even at higher fields. Taken together, these observations are consistent with the presence of a ferromagnetic component to the measured magnetic response that has a Curie temperature well above room temperature. Because the ferromagnetic response is so small, this ordered component is assumed to constitute an impurity phase. Assuming for example that the impurity phase was composed of metallic iron, which is ferromagnetic with a Curie temperature of 1043 (15), about 40 ppm in the Pu selenite sample would be sufficient to produce the anomalous field dependence to the data. Following previous precedent for a minor ferromagnetic impurity (16), the magnetization data at two different fields in the linear region, 5000 and 2000 Oe, were subtracted and used to obtain the measured, field-independent, susceptibility used in the analysis.

RESULTS AND DISCUSSION

Synthesis. The synthesis of $Pu(SeO_3)_2$ proceeded by the dissolution of PuO_2 in selenous acid under hydrothermal conditions, which led to crystallization of $Pu(SeO_3)_2$ that appeared as brick-red prisms.

Structural Features of $Pu(SeO_3)_2$. The structure of $Pu(SeO_3)_2$ is isotypic with that of $Ce(SeO_3)_2$,[6] and consists of one-dimensional chains of edge-sharing PuO_8 units that extend down the *a* axis, as is shown in Figure 4.1. The chains are interconnected by selenite anions to form a dense three-dimensional structure depicted in Figure 4.2. There are small channels in the structure that extend down the *a* axis to which hold the lone-pair of electrons from the selenite anions. Selected bond distances and angles for the product are given in Table 4.3. The Pu−O bond distances range from 2.240(5) to 2.495(5) Å. Se−O bonds range from 1.667(5) to 1.735(4) Å for Se(1), and from 1.696(5) to 1.704(5) Å for Se(2).

The geometry of eight-coordinate metal centers in the structure has been the subject of interest for sometime.[11] Four idealized shapes are possible. Theseinclude the D_{2d} trigonal dodecahedron found for Pu^{4+} in $Pu(IO_3)_4$,[12] the C_{2v} bicapped trigonal prism, (e.g. for Cf^{3+} in orthorhombic-$CfCl_3$),[13] the D_{4d} square antiprism observed for Ce^{4+} in $Ce(5LI\text{-}Me\text{-}3,2\text{-}HOPO)_2{\cdot}CH_3OH$,[14] and the O_h cubic environment for Pu^{4+} in PuO_2. Raymond and co-workers have developed an algorithm for determining the polyhedron that the eight-coordinate units most closely approximate .[14] We have used this program to evaluate the environment around the Pu centers in $Pu(SeO_3)_2$, and find that they are most closely approximated by a bicapped trigonal prism (C_{2v}, $S = 17.6^o$), although the deviations from D_{2d} ($S = 18.8^o$) and D_{4d} ($S = 18.7^o$) are only slightly more significant.[14]

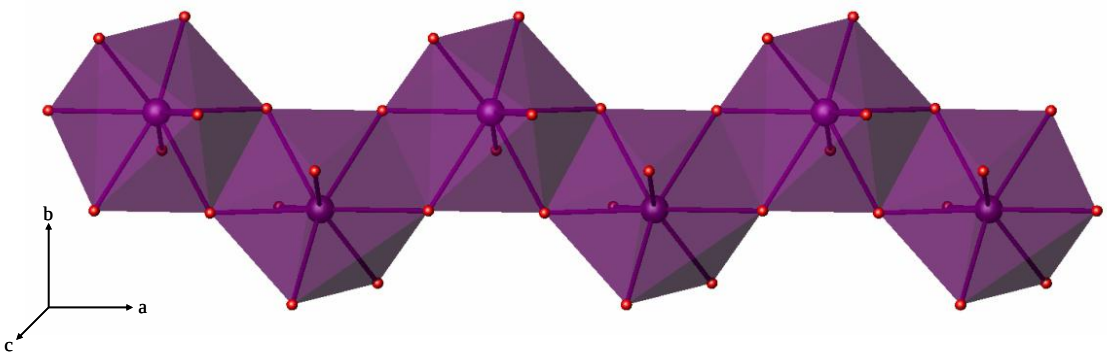

Figure 4.1. A view of the one-dimensional chains of edge-sharing PuO_8 dodecahedra that extend down the *a* axis in the structure of $Pu(SeO_3)_2$.

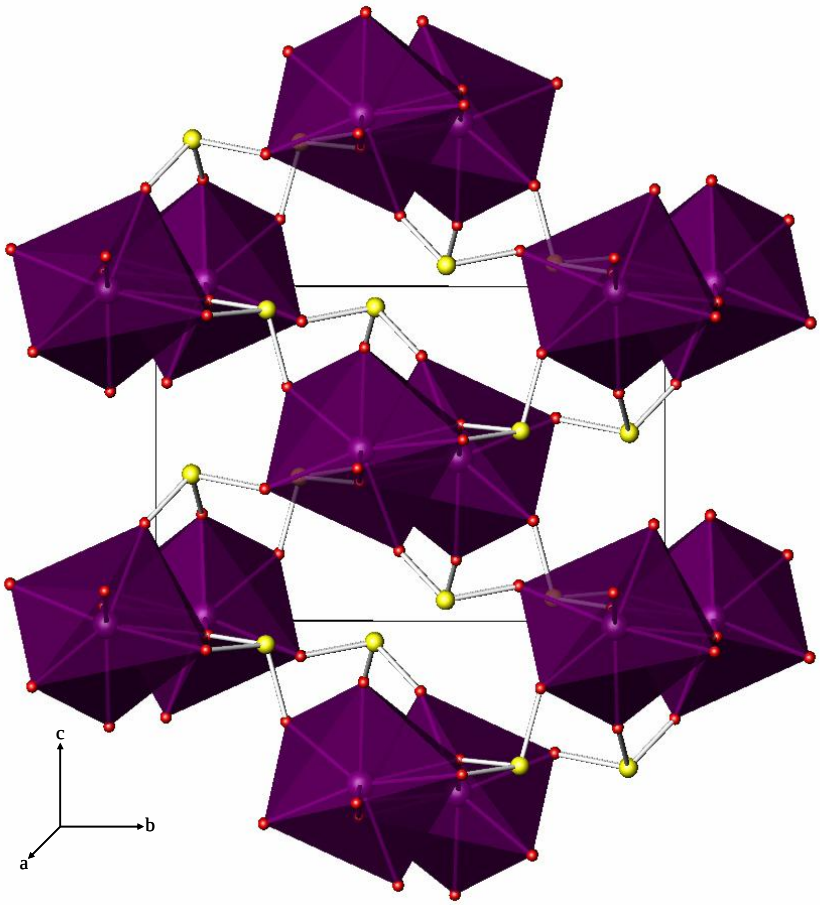

Figure 4.2. A depiction of the three-dimensional structure of $Pu(SeO_3)_2$ formed from the interconnection of one-dimensional chains of edge-sharing PuO_8 dodecahedra by selenite anions.

Table 4.3. Selected bond distances (Å) and angles (^{o}) for $Pu(SeO_3)_2$.

Distances (Å)			
Pu(1)–O(1)	2.340(5)	Se(1)–O(1)	1.667(5)
Pu(1)–O(2)	2.356(5)	Se(1)–O(2)	1.713(5)
Pu(1)–O(2)′	2.495(5)	Se(1)–O(3)	1.735(4)
Pu(1)–O(3)	2.324(5)	Se(2)–O(4)	1.698(5)
Pu(1)–O(3)′	2.396(4)	Se(2)–O(5)	1.704(5)
Pu(1)–O(4)	2.243(5)	Se(2)–O(6)	1.696(5)
Pu(1)–O(5)	2.280(5)		
Pu(1)–O(6)	2.240(5)		
Angles (°)			
O(1)–Se(1)–O(2)	100.8(2)	O(4)–Se(2)–O(5)	105.8(2)
O(2)–Se(1)–O(3)	90.0(2)	O(4)–Se(2)–O(6)	100.1(2)
O(1)–Se(1)–O(3)	102.4(2)	O(5)–Se(2)–O(6)	98.6(2)

Magnetism. Pu^{4+} has a J=4 ground manifold. Under an idealized cubic electrostatic field the manifold is expected to split into a singlet, a doublet, and two triplet states, with the lowest energy state a singlet for all ratios of the 4^{th} to the 6^{th} order crystal-field parameters.[19] The Pu^{4+} in $Pu(SeO_3)_2$ sits on an eight- coordinate site with C_1 symmetry and, as such, all symmetry-imposed degeneracies are lifted. The splitting of the resulting nine singlets within the first J manifold the splitting is expected to be much larger than kT (20). Such an electronic structure is expected to produce at lower temperatures only van Vleck temperature-independent paramagnetism (TIP), which arises from the mixing by the magnetic field of crystal-field states in different f-ion J manifolds.

The magnetic susceptibility of $Pu(SeO_3)_2$ is shown in Figure 4.3. It exhibits a temperature dependence over the entire range of the experiment but there is no evidence of magnetic ordering as low as 5k. Assuming non-interacting, temperature-independent magnetic moments, the magnetic susceptibility can be represented by the Curie-Weiss Law, $\chi = C/(T-\theta)$, where C is the Curie constant, related to the effective moment by $\mu_{eff} = (3kC/N\mu_B^2)^{1/2}$, and θ is the Weiss constant, which is interpreted as a temperature offset to adjust for lower-temperature moment correlations.[17] A standard Curie-Weiss plot, shown as an insert to Figure 4.3, reveals a linear region to the susceptibility over the temperature range of 35-320 K. The linearity of the data plotted in this manner is consistent with a negligible TIP over this temperature range. A fit to the linear range of the data produces an effective moment of 2.71(5) μ_B and a Weiss constant of -500(5) K. The effective moment is within error limits of the full free ion moment of 2.68 μ_B expected for a $^5I_4$ ground level assuming Russell-Saunders coupling. This result is unexpected based on the

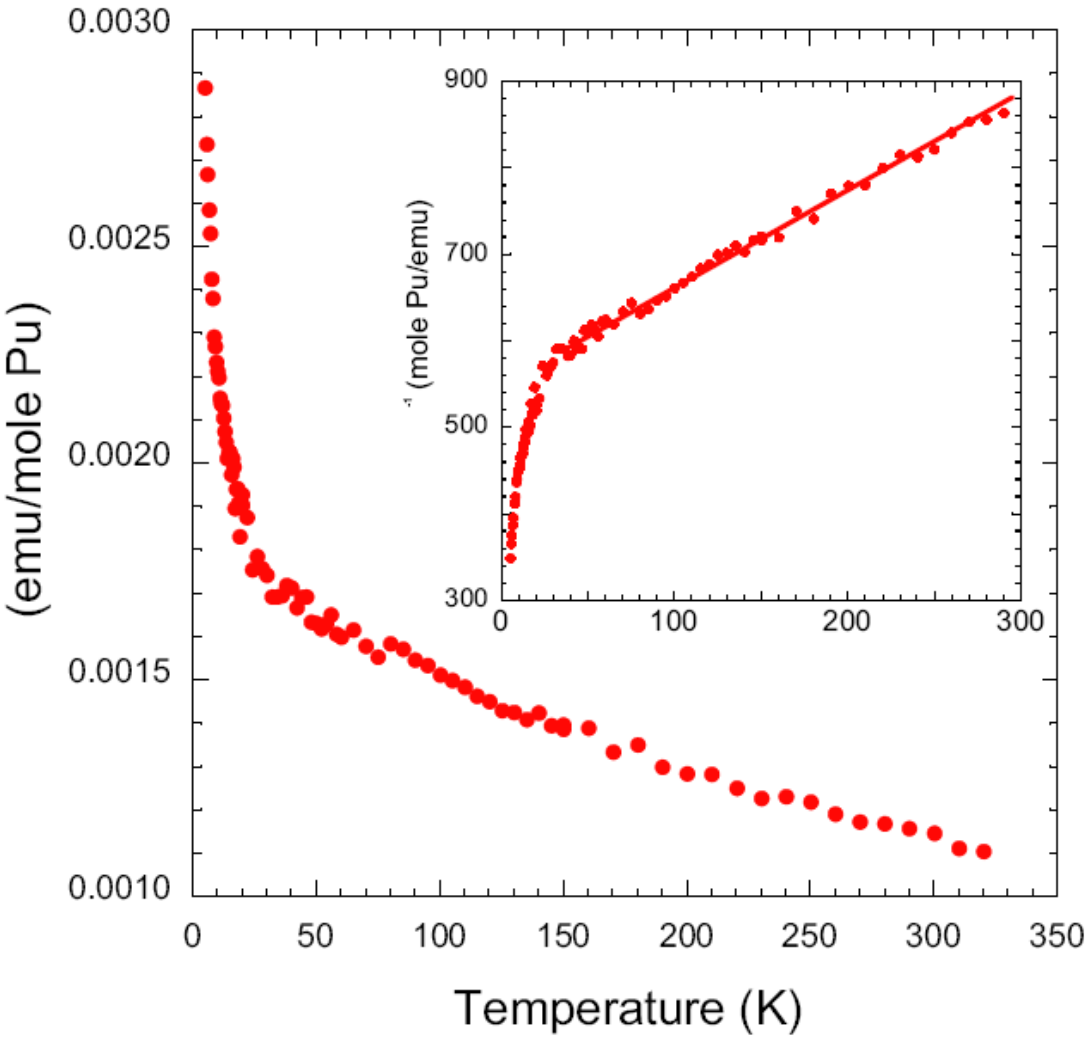

Figure 4.3. The magnetic susceptibility of $Pu(SeO_3)_2$ as a function of temperature obtained by subtracting the magnetization measured under an applied field of 2000 Oe from the contribution under a field of 5000 Oe (see text). Temperature dependence at low temperature is not consistent with simple magnetic ordering. Inset shows the same data plotted assuming Curie-Weiss behavior. The solid line, extending over the temperature range of 35 – 300 K, represents the best fit to the data (see text). Low temperature deviation from linearity is consistent with the influence of magnetic correlations.

coordination environment and its splitting of the ground level into singlet states. Even in a cubic crystal-field such as found in PuO_2, in which the metal sits in a cubic site that is also surrounded by 8 oxygens, there is an isolated ground state singlet with a triplet state at about 90 meV or higher in energy. As expected, it has no measurable temperature dependence to its susceptibility and an experimentally determined TIP of 536 x 10^{-6} emu/mole.[21, 22]

The absence of a TIP term to the susceptibility measured for $Pu(SeO_3)_2$, together with strong evidence that the Pu has a degenerate ground state, raises the question of whether Pu may be trivalent in this material; however, a f^5 configuration has a free-ion moment of 0.845 μ_B, which is too small to account for the magnetic behavior. In addition, the structural data are consistent with tetravalent Pu, i.e., the bond-valence sum for Pu(1) is 4.45.[25, 26]

The inclusion of a Weiss constant in the Curie Law is meant to represent the influence at higher temperatures for low temperature collective or correlated magnetic fluctuations, which are not explicitly included in the simpler model.[15] Within this formalism, a negative value of the Weiss constant could suggest antiferromagnetic interactions. However, the very large value of -500 K found here for the Pu^{4+} selenite would suggest a very strong spin interaction that persists well above room temperature and outside the range of our measurements. The absence of magnetic ordering is not consistent with such a strong coupling. Furthermore, field dependence studies do not support this suggestion. An alternate explanation requires the magnetic moment to change with temperature, a situation that arises when there are low-lying excited crystal field states that are within kT of the ground state and therefore change population over

the temperature range of the experiment. Such changes are known to result in significant deviations from a simple Curie law, which may be incorporated, at least to some extent, into a Weiss constant.[18] Thus, the presence of a large local moment suggests that the C_1 symmetry results in an accidentally degenerate ground state or almost degenerate single states that are thermally populated even at low temperatures.

The susceptibility has been published for two different hydrated sulfates, $Pu(SO_4)_2 \cdot 4H_2O$ and $Rb_4Pu(SO_4)_4 \cdot 2H_2O$.[23, 24] The Pu^{4+} in the hydrated disulfate sits on a low symmetry site surrounded by 8 oxygen atoms, whereas the Pu^{4+} in the hydrated tetrasulfate is coordinated to nine oxygens. Both compounds show deviations from simple Curie Weiss behavior at low temperatures. Fitting the data over 200-335 K results in effective moments of 2.96 μ_B and Weiss constant of 290 and 830 K, respectively. Similar behavior has been reported for PuF_4, in which the Pu sits in a distorted 8-coordinate site and has a μ_{eff} of 2.90 μ_B and a θ of 270 K. The latter compound also exhibits a strong TIP contribution below about 150 K. The very large value of the Weiss constants required for fitting the data, coupled with the absence of evidence for magnetic ordering at lower temperatures and unusual temperature dependence suggest that a simple Curie-Weiss model does not well represent the susceptibility data for these complex chalcogenide-oxide systems.

Data obtained for the Pu monochalcogenides including PuS, PuSe, and PuTe, have similar temperature dependences to those obtained here for $Pu(SeO_3)_2$ in the sense that they have a sharply rising susceptibility at low temperature but exhibit only temperature-independent paramagnetism above 60 K(27). These monochalcogonides have the rocksalt structure in which the Pu sits in a six coordinate, cubic site. Although

the oxidation state is unclear, the evidence presented is inconsistent with an intermediate-valent system. The difficulties in fitting the susceptibility data for these monochalcogenides were explained in terms of defect sites that could include charge transfer, a scenario that is ruled out in our case.

The magnetic behavior of $Pu(SeO_3)_2$ is complex and not fully understood. On the one hand, the fit to the data assuming a simple Curie Weiss behavior produces an effective moment in the range expected for an f^4 configuration with no discernable TIP. This would suggest an aggregate of non-interacting spins above about 35 K, consistent with a simple paramagnet. On the other hand, the data fitting requires a Weiss constant of -500 K; a value that suggests very strong magnetic correlations that are not borne out by any evidence of ordering at low temperature. Overall, this system is not well modeled by the Curie-Weiss formalism despite the presence of a well localized moment that does not order above 5 K. The mechanism by which the Pu acquires such a large ground-state moment in this system is not understood, nor is the apparent large interaction temperature, but these findings are of interest in the broader question of local moment formation, or lack thereof, in simple actinide compounds.[28]

REFERENCES

1) a) Runde, W.; Bean, A. C.; Albrecht-Schmitt, T. E.; Scott, B. L. *Chem. Comm.* **2003**, *4*, 478. b) Bean, A. C.; Scott, B. L.; Albrecht-Schmitt, T. E.; Runde, W. *Inorg. Chem.* **2003**, *42*, 5632.

2) a) Weigel, F.; Engelhardt, L. W. H. *J. Less-Common Met.* 1983, *91*, 339. b) Bean, A. C.; Peper, S. M.; Albrecht-Schmitt, T. E. *Chem. Mater.* 2001, *13*, 1266.

3) a) Gorden, A. E. V.; Shuh, D. K.; Tiedemann, B. E. F.; Wilson, R. E.; Xu, J.; Raymond, K. N.; *Chemistry*, **2005**, *11*, 2842. b) Gorden, A. E. V.; Xu, J.; Raymond, K. N. *Chem. Rev.* **2003**, *103*, 4207.

4) Xu, J.; Radkov, E.; Ziegler, M.; Raymond, K. N. *Inorg. Chem.* **2000**, *39* 4156.

5) Sykora, R. E.; Shvareva, T. Y.; Albrecht-Schmitt, T. E. in *Structural Chemistry of Inorganic Actinide Compounds*, Elsevier Science, 2007.

6) Delage, C.; Carpy, A. ; H'Naïfi, A. ; Goursolle, M. *Acta Cryst.* **1986**, *C42*, 1475.

7) Edelstein, N. M.; Lander, G. H. in *The Chemistry of the Actinide and Transactinide Elements*, Ed. Morss, L.; Edelstein, N. M.; Fuger, J.: Springer, Dordrecht, Ch. 20, 2006.

8) Karraker, D. G. *Inorg. Chem.* 10 (1971) 1564.

9) Sheldrick, G. M. SHELXTL PC, Version 6.12, "An Integrated System for Siemens Analytical X-Ray Instruments, Inc.: Madison, WI 2001.

10) Sheldrick, G. M. *SADABS* 2001, Program for absorption correction using SMART CCD based on the method of Blessing: Blessing, R. H. *Acta Crystallogr.* **1995**, *A51*, 33.

11) a) Hoard, J. L.; Silverton, J. V. *Inorg. Chem.* **1963**, *2*, 235. b) Lippard, S. J.; Russ, B. J. *Inorg. Chem.* **1968**, *7*, 1686. c) Porai-Koshits, M. A.; Aslanov, L. A. *Russ. J. Struct. Chem.* **1974**, *13*, 244. e) Muetteries, E. L.; Guggenberger, L. *J. Am. Chem. Soc.* **1974**, *96*, 1748.

12) Bray, T. H.; Ling, J.; Choi, E.-S.; Brooks, J. S.; Beitz, J. V.; Sykora, R. E.; Haire, R. G.; Stanbury, D. M.; Albrecht-Schmitt, T. E. *Inorg. Chem.* **2007**, *46*, 3663.

13) Burns, J. H.; Peterson, J. R.; Baybarz, R. D. *J. Inorg. Nucl. Chem.* **1973**, *35*, 1171.

14) Xu, J.; Radkov, E.; Ziegler, M.; Raymond, K. N. *Inorg. Chem.* **2000**, *39*, 4156.

15) Kittel, C. *Introduction to Solid State Physics*. 1976, New York: John Wiley & Sons. 608.

16) Gray, D. L.; Backus, L. A.; Von Nidda, H.-A. K.; Skanthakumar, S.; Loidl, A.; Soderholm, L.; Ibers, J. A. *Inorg. Chem.* **2007**, *46*, 6992.

17) Ashcroft, N. W.; Mermin, N. D. *Solid State Physics*. 1976, Philadelphia: Saunders College. p. 826.

18) Staub, U.; Soderholm, L. *Electronic 4f state splittings in cuprates*, in *Handbook on the Physics and Chemistry of Rare Earths*, Gschneidner Jr., K. A.; Eyring, L.; and Maple, M. B. Editors. 2000, Elsevier Science: Amsterdam. p. 491-545.

19) Lea, K. R.; Leask, M. J. M.; Wolf, W. P. *J. Phys. Chem. Solids.* **1962**, *23*, 1381.

20) Newman, D. J.; Ng, B. *J. Phys.:Condens. Matter*, **1989**, *1*, 1619.

21) Raphael, G.; Lallement, R. *Solid State Commun*. **1968**, *6*, 383.

22) Colarieti-Tosti, M.; Eriksson, O.; Nordstrom, L.; Wills, J.; Brooks, M. S. S. *Phys. Rev. B.* **2002**, *65*, 195102.

23) Lewis, W. B.; Elliott, N. *J. Chem. Phys.* **1957**, *27*, 904.

24) Kanellakopulos, B.; Klenze, R. *Magnetic properties of organometallic and coordination compounds of plutonium*, in *Plutonium Chemistry*, Carnall, W.T. and Choppin, G.R. Editors. 1983, American Chemical Society: Washington, D.C. p. 25-40.

25) Brown, I. D.; Altermatt, D. *Acta Crystallogr.* **1985**, *B41*, 244.

26) Brese, N. E.; O'Keeffe, M. *Acta Crystallogr.* **1991**, *B47*, 192.

27) Lander, G. H.; Rebizant, J.; Spirlet, J. C.; Delapalme, A.; Brown, P. J.; Vogt, O.; Mattenberger, K. *Physica B.* **1987**, *146*, 341.

28) Hotta, T. *Reports Prog. Phys.* **2006**, *69*, 2061.

CHAPTER 5

PRODUCT EVOLUTION IN THE Np(IV) FLUOROPHOSPHATE SYSTEM

Reproduced with permission from Bray, Travis H.; Sullens, Tyler A.; Shvareva, Tatiana Y.; Sykora, Richard E.; Haire, Richard G.; Albrecht-Schmitt, Thomas E. *J. Solid State Chem.* **2007**, *180*, 70-74. Copyright 2007 Elsevier.

ABSTRACT

The reaction of $^{237}NpO_2$ with Cs_2CO_3, Ga_2O_3, H_3PO_4, and HF under mild hydrothermal conditions leads to the formation of $NpFPO_4$ after four days at 180 °C. Heating at 180 °C for an additional six days leads to the crystallization of $Cs_2Np_2F_7PO_4$ and NpF_4. The Ga_2O_3 forms a $GaPO_4$ matrix in which crystals of $NpFPO_4$, $Cs_2Np_2F_7PO_4$, and NpF_4 grow. Single crystal X-ray data reveal that the structure of $NpFPO_4$ consists of Np(IV) centers bound by both fluoride and phosphate to yield $[NpF_2O_6]$ distorted dodecahedra. These are linked by corner-sharing with fluoride and both corner- and edge-sharing with phosphate to yield a dense, three-dimensional network. The structure of $Cs_2Np_2F_7PO_4$ is complex and contains both distorted dodecahedral $[NpO_2F_6]$ and tricapped trigonal prismatic $[NpO_2F_7]$ environments around Np(IV) that are linked with each other through corner- and edge-sharing, and with the phosphate groups to create a three-dimensional structure. There are small channels extending down the *a* axis in $Cs_2Np_2F_7PO_4$. Crystallographic data: $NpFPO_4$, orthorhombic, space group *Pnma*, a = 8.598(2), b = 6.964(1), c = 6.337(1) Å, Z = 4, V =

379.44(13) Å^3, R(F) = 3.53% for 40 parameters and 465 reflections with $I > 2\sigma(I)$ (T = 193 K); $Cs_2Np_2F_7PO_4$, monoclinic, space group $P2_1/c$, a = 8.8727(4), b = 16.2778(7), c = 7.8009(4) Å, β = 112.656(1), Z = 4, V = 379.44(13) Å^3, R(F) = 2.27% for 146 parameters and 2465 reflections with $I > 2\sigma(I)$ (T = 193 K).

INTRODUCTION

Np(IV) phosphates were first prepared to determine the solubility of a wide range of Np compounds for designing separation and purification processes for the actinides.[1] Reports on the intentional preparation of pure Np(IV) phosphates came surprisingly late with the indication that $NaNp_2(PO_4)_3$ and $Na_2Np(PO_4)_2$ are isostructural with other tetravalent actinide analogs.[2] A thorough investigation of the An^{4+} (An = Th, U, Np) phosphate system showed that the only orthophosphate that could be prepared is $Th_3(PO_4)_4$.[3] Furthermore, while the pyrophosphates, α-MP_2O_7, (M = U, Th, and Np) can be prepared, the oxypyrophosphates were only found for $(MO)_2P_2O_7$ (M = Np, U) (3). Recent interest in Np(IV) phosphates has been primarily motivated by the potential utility of phosphate phases, particularly monazites, for long-term storage hosts for transuranium elements.[4] In addition, the complexation of higher oxidation states of Np by phosphate in solution may be of environmental importance.[5]

A recent search of the Inorganic Crystal Structure Database (ICSD) for single crystal structures of Np(IV) phosphates revealed their surprising absence,[6] although powder diffraction data are noted in the ICSD files. Despite the aforementioned importance of these compounds, the lack of information on these Np phases occurs in part because of the practice of using the substantially less radioactive elements, Th and U,

as surrogates for Np. The use of Th and U to represent Np chemistry is questionable, especially if the potential for redox processes to occur.[7] As a part of ongoing studies on actinide phosphates,[8] the preparation, structures, and properties of Np(IV) phosphates are of interest. Herein, the three-dimensional frameworks of two Np(IV) fluorophosphates, $NpFPO_4$ and $Cs_2Np_2F_7PO_4$, are reported.

EXPERIMENTAL

General Information. $^{237}NpO_2$ (99.9%, ORNL), Ga_2O_3 (99.99%, Alfa-Aesar), Cs_2CO_3 (99.99%, Alfa-Aesar), H_3PO_4 (98%, Aldrich), and HF (48 wt.%, Aldrich) were used as received. Distilled and Millipore filtered water with a resistance of 18.2 MΩ·cm was used in all syntheses. Reactions were run in Parr 4749 autoclaves with custom-made 10-mL PTFE liners. All studies were conducted in a lab dedicated to studies on transuranium elements using procedures previously described.[7]

$NpFPO_4$ and $Cs_2Np_2F_7PO_4$ Syntheses. NpO_2 (0.0100 g, 0.037 mmol), Ga_2O_3 (0.0070 g, 0.037 mmol), H_3PO_4 (0.0150 g, 0.153 mmol), Cs_2CO_3 (0.0360 g, 0.110 mmol), HF (0.2 mL), and 0.5 mL of water were loaded into a 10-mL PTFE-lined autoclave. The autoclave was sealed and placed into a box furnace that had been pre-heated to 180 °C. The reaction solutions were cooled for different periods at a rate of 9 °C/h to 23 °C. After four days of heating, the solid products consisted of green blocks of $NpFPO_4$ in $GaPO_4$ matrix. The yield was considered to be nearly 100%: $NpFPO_4$ was the only Np-containing product and soluble Np in the mother liquor was not detected using UV-vis-NIR spectroscopy. After a total of ten days at 180 °C, green, roughly hexagonal

tablets of $Cs_2Np_2F_7PO_4$ and large acicular crystals of NpF_4 were isolated from a $GaPO_4$ matrix, and NpF_4 was the major product.

Crystallographic Studies. Single crystals of $NpFPO_4$ (0.094 x 0.034 x 0.032 mm) and $Cs_2Np_2F_7PO_4$ (0.079 x 0.060 x 0.034 mm) were selected using a digital microscope with remote viewing capabilities, and were transferred to Krytox oil. Crystals suitable for diffraction studies were mounted on glass fibers with epoxy and optically aligned on a Bruker SMART APEX CCD X-ray diffractometer using a digital camera. Intensity measurements were performed using graphite monochromated MoKα radiation from a sealed tube and monocapillary collimator. SMART (v 5.624) was used for preliminary determination of the cell constants and data collection control. The intensities of reflections of a sphere were collected by a combination of 3 sets of exposures (frames). Each set had a different ϕ angle for the crystal and each exposure covered a range of 0.3° in ω. A total of 1800 frames were collected with an exposure time per frame of 30 s for each compound.

Determination of integrated intensities and global refinement were performed with the Bruker SAINT (v 6.02) software package using a narrow-frame integration algorithm. A face-indexed analytical absorption correction was initially applied using XPREP, where individual shells of unmerged data were corrected analytically. These files were subsequently treated with a semiempirical absorption correction by SADABS.[9] The program suite, SHELXTL (v 6.12), was used for a space group determination (XPREP), direct methods structure solution (XS), and least-squares refinement (XL).[10] The final refinements included anisotropic displacement parameters for all atoms and secondary extinction. Selected crystallographic details are listed in Table 5.1. Atomic

Table 5.1. Crystallographic data for $NpFPO_4$ and $Cs_2Np_2F_7PO_4$.

Formula	$NpFPO_4$	$Cs_2Np_2F_7PO_4$
Formula Mass	350.97	967.79
Color and habit	green block	green tablet
Crystal System	Orthorhombic	monoclinic
Space group	*Pnma* (No. 62)	$P2_1/c$ (No. 14)
a (Å)	8.598(2)	8.8727(4)
b (Å)	6.964(1)	16.2778(7)
c (Å)	6.337(1)	7.8009(4)
V (Å^3)	379.4(1)	1039.73(8)
Z	4	4
T (K)	193	193
λ (Å)	0.71073	0.71073
Maximum 2θ (deg.)	56.48	56.60
ρ_{calcd} (g cm^{-3})	6.144	6.183
μ(Mo *K*α) (cm^{-1})	277.16	270.30
R(*F*) for $F_o^2 > 2\sigma(F_o^2)$	0.0353	0.0227
$R_w(F_o^2)$ [b]	0.0976	0.0590

[a] $R(F) = \sum \left| |F_o| - |F_c| \right| / \sum |F_o|$. [b] $R_w\left(F_o^2\right) = \left[\sum \left[w\left(F_o^2 - F_c^2\right)^2 \right] / \sum wF_o^4 \right]^{1/2}$.

Table 5.2. Atomic coordinates and equivalent isotropic displacement parameters for $NpFPO_4$.

Atom (site)	*x*	*y*	*z*	U_{eq} ($Å^2$) [a]
Np(1)	0.45116(6)	¾	0.14279(8)	0.0070(3)
P(1)	0.6003(5)	¾	-0.3203(6)	0.0110(7)
F(1)	0.7135(9)	¾	0.1933(13)	0.0148(17)
O(1)	0.4897(13)	¾	-0.5049(18)	0.0143(19)
O(2)	0.5657(8)	0.9234(12)	-0.1689(11)	0.0112(15)
O(3)	0.7718(11)	¾	-0.3894(16)	0.013(2)

Table 5.3. Atomic coordinates and equivalent isotropic displacement parameters for $Cs_2Np_2F_7PO_4$.

Atom (site)	*x*	*y*	*z*	U_{eq} (Å^2) [a]
Np(1)	0.14644(3)	0.577904(12)	0.17201(3)	0.00784(8)
Np(2)	0.45409(3)	0.741629(13)	0.49805(3)	0.00726(8)
Cs(1)	-0.03199(5)	0.82970(2)	0.08366(5)	0.01638(10)
Cs(2)	-0.35359(5)	0.99230(2)	-0.23771(6)	0.01908(10)
P(1)	0.72866(18)	0.62731(9)	0.8809(2)	0.0092(3)
O(1)	0.9087(5)	0.6460(2)	0.0045(6)	0.0121(8)
O(2)	0.7051(5)	0.5344(2)	0.8390(6)	0.0131(8)
O(3)	0.6783(5)	0.6733(3)	0.6953(6)	0.0118(8)
O(4)	0.6218(5)	0.6527(2)	0.9864(6)	0.0126(8)
F(1)	0.0994(5)	0.5517(2)	0.4170(5)	0.0179(8)
F(2)	0.0466(4)	0.5277(2)	-0.1265(5)	0.0133(7)
F(3)	0.1788(4)	0.7055(2)	0.3172(5)	0.0125(7)
F(4)	0.2857(4)	0.6495(2)	0.0214(5)	0.0140(7)
F(5)	0.3965(4)	0.5998(2)	0.4142(5)	0.0124(7)
F(6)	0.3465(4)	0.6928(2)	0.7004(5)	0.0122(7)
F(7)	0.5649(4)	0.6955(2)	0.2966(5)	0.0112(6)

coordinates and equivalent isotropic displacement parameters for $NpFPO_4$ and $Cs_2Np_2F_7PO_4$ are given in Tables 5.2 and 5.3, respectively. Further details of the crystal structure investigation may be obtained from the Fachinformationzentrum Karlsruhe, D-76344 Eggenstein-Leopoldshafen, Germany (Fax: (+49)7247-808-666; Email: crysdata@fiz-karlsruhe.de) on quoting depository numbers CSD 416757 and 416758.

UV-vis-NIR Spectroscopy. Absorption spectra of the mother liquors were collected using a Shimadzu UV3101 spectrophotometer.

RESULTS AND DISCUSSION

Synthesis. The evolution of product formation in the Np(IV) fluorophosphate system is of interest from several standpoints. First, the dissolution of NpO_2 in acid often leads to the formation of solutions containing NpO_2^+.[11] While it is possible that NpO_2^+ could form and then disproportionate to yield Np^{4+} and NpO_2^{2+},[12] Np(VI) was not detected in our solutions. We have previously reported that HF can reduce U(VI) under hydrothermal conditions, but organic amines have always been present in these cases.[13] One explanation for the absence of oxidation in these reactions is that $NpFPO_4$ may be sufficiently insoluble and precipitate before oxidation of Np(IV) occurs, as it is process known to be slow.[14] A subsequent reaction of $NpFPO_4$ with fluoride in the presence of Cs^+ could also lead to the formation of $Cs_2Np_2F_7PO_4$, which upon further reaction would yield NpF_4. Nucleation sites for crystals of NpF_4, $NpFPO_4$, and $Cs_2Np_2F_7PO_4$ are provided by the $GaPO_4$ matrix that forms. The acicular crystals of NpF_4 that grow from this matrix were quite long (several mm in length), although they were unfortunately

highly twinned. Crystals of $NpFPO_4$ and $Cs_2Np_2F_7PO_4$ were found both on the surface and within the $GaPO_4$ matrix.

Structure of $NpFPO_4$. The structure of $NpFPO_4$ consists of Np(IV) centers bound by both fluoride and phosphate to yield $[NpF_2O_6]$ distorted dodecahedra, as is shown in Figure 5.1. The PO_4^{3-} anions play a fascinating role in this structure in that they chelate one Np center and through two μ_3 and two μ_2 oxo atoms, bind an additional four Np sites. The fluoride anions are μ_2 and simply bridge between two Np(IV) ions. The $[NpF_2O_6]$ units share two edges and two corners with identical polyhedra to assemble into a dense three-dimensional network that is shown in Figure 5.2.

The Np–O bond distances range from 2.227(9) to 2.515(8) Å, and the two Np–F distances are 2.278(8) and 2.292(8) Å. It is important to note here, and for that matter in most oxyfluorides, that it is usually not possible to distinguish between the O atoms and F atoms based on standard X-ray scattering or bond distances. This is a pervasive problem in fluoride chemistry, especially when hydrolysis is involved. One argument for it being a fluoride ion and not a hydroxide ion is a lack of an appropriate hydrogen bonding distance. Furthermore, semi-quantitative SEM-EDX measurements clearly show the presence of F in the crystals. The P–O bond distances are normal with two longer bonds of 1.571(8) Å (×2) to the μ_3–O atoms, and two shorter bonds of 1.508(11) and 1.537(10) Å to the μ_2–O atoms. Selected bond distances for $NpFPO_4$ are given in Table 5.4. The structure of $NpFPO_4$ is also illustrative of another problem with published single crystal structures described as containing Np(IV).[6] In an previous work, we derived bond-valence parameters for Np(V) and Np(VI),[7d, 15] and we have found that these parameters work quite well, although they should be improved as more high-resolution

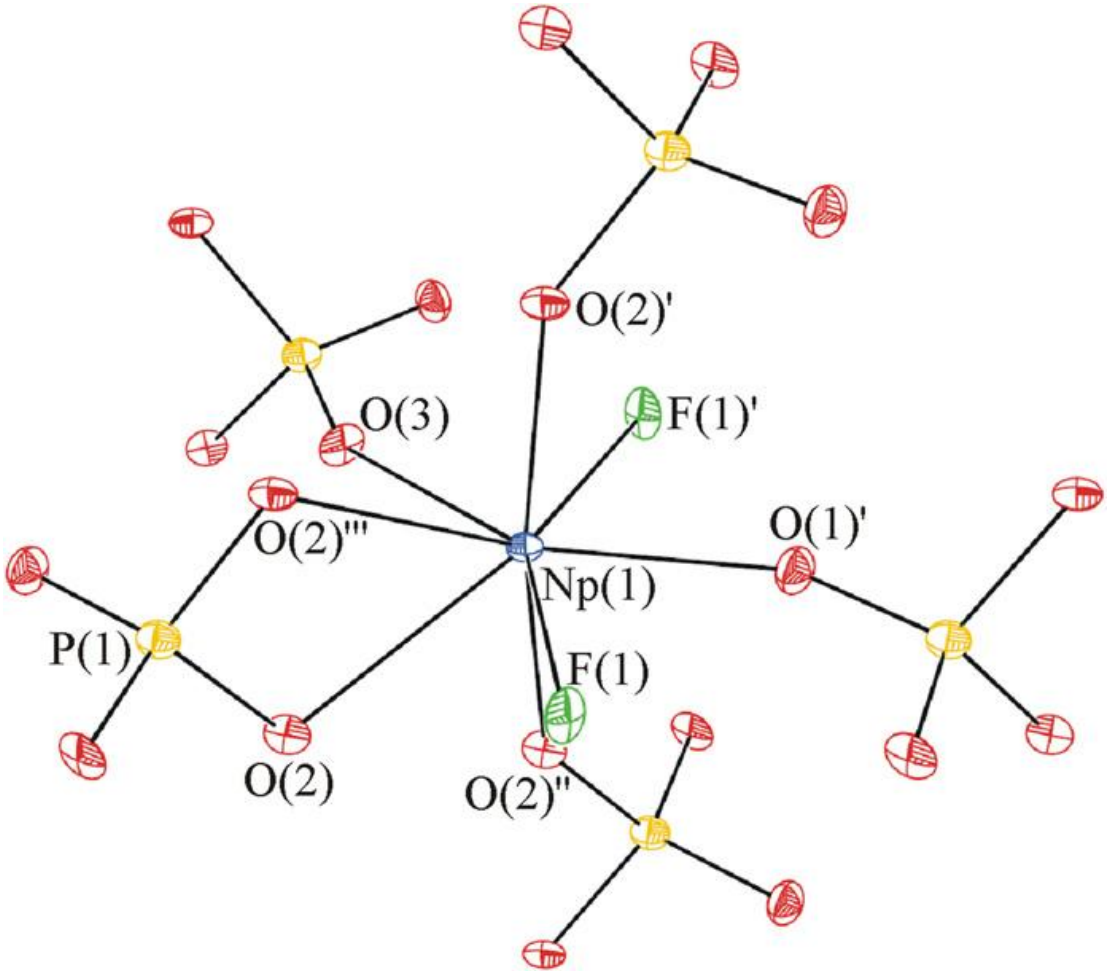

Figure 5.1. A view of the fundamental building units in $NpFPO_4$ that consist of Np(IV) centers bound by both fluoride and phosphate to yield [NpF_2O_6] distorted dodecahedra. [50% probability ellipsoids are depicted.]

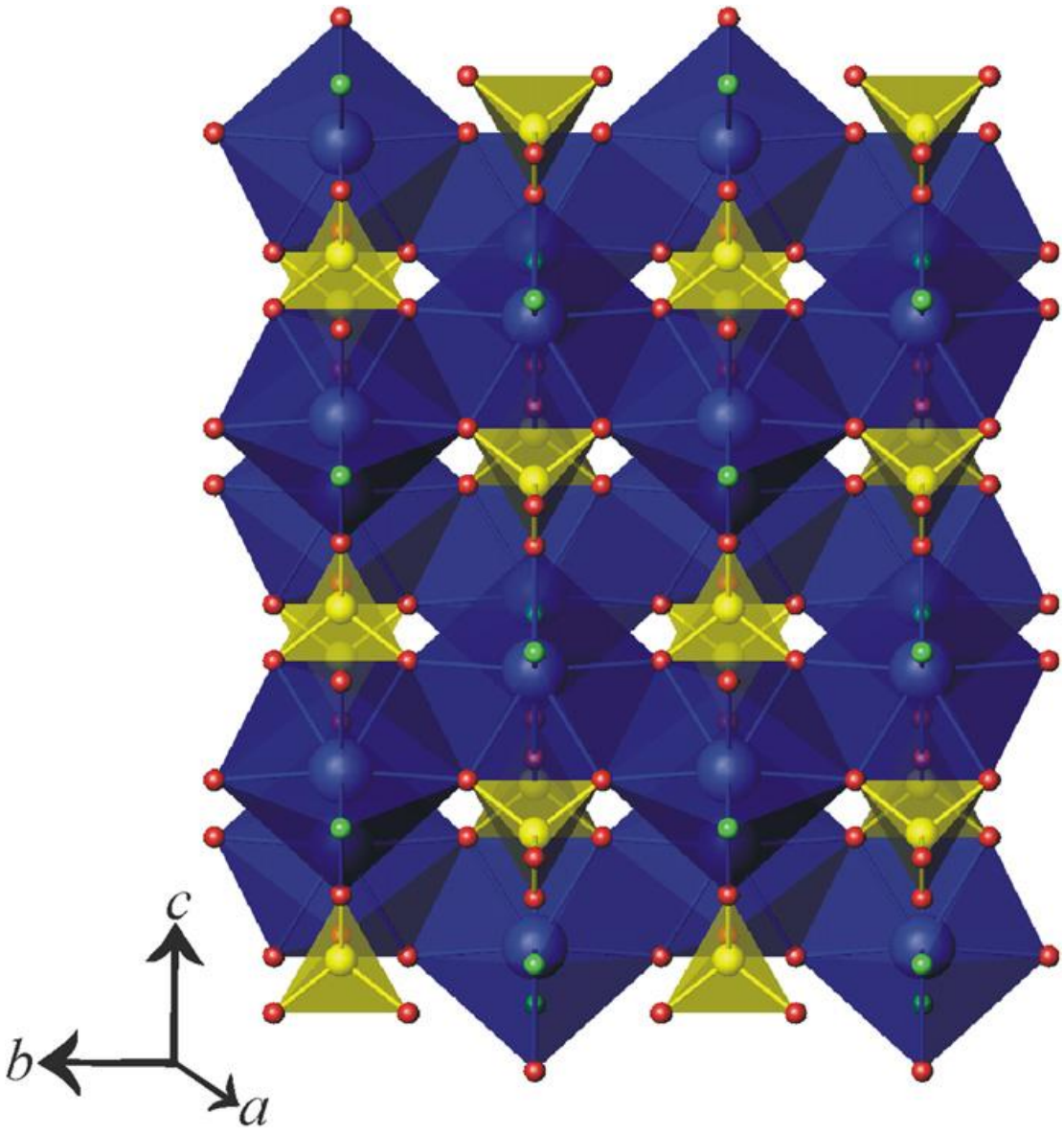

Figure 5.2. A depiction of the tightly-packed structure of $NpFPO_4$. $[NpF_2O_6]$ distorted dodecahedra are shown in blue, phosphate anions in yellow, oxygen atoms are red, and fluoride anions in green.

Table 5.4. Selected bond distances (Å) for $NpFPO_4$.

Distances (Å)			
Np(1)–O(1)	2.257(11)	Np(1)–F(1)	2.278(8)
Np(1)–O(2)	2.285(8)	Np(1)–F(1)'	2.292(8)
Np(1)–O(2)'	2.285(8)	P(1)–O(1)	1.508(11)
Np(1)–O(2)"	2.515(8)	P(1)–O(2)	1.571(8)
Np(1)–O(2)"'	2.515(8)	P(1)–O(2)'	1.571(8)
Np(1)–O(3)	2.227(9)	P(1)–O(3)	1.537(10)

structures become available. When we attempted to determine an appropriate bond-valence parameter for Np(IV)–O bonds, the distances available from the small number of known structures could not be used to derive a reliable value. There may simply be too few structures available at this time, and/or some of the previously reported Np(IV) compounds structures may be incorrect.

Structure of $Cs_2Np_2F_7PO_4$. The structure of $Cs_2Np_2F_7PO_4$, as its formula suggests, is much more complex than that of $NpFPO_4$. To begin, there are two crystallographically unique Np centers in two different coordination environments. Both Np(IV) cations are bound by both fluoride and phosphate. Np(1) is found as a $[NpO_2F_6]$ distorted dodecahedron, while Np(2) in $[NpO_2F_7]$ is a tricapped trigonal prism, as depicted in Figure 5.3. The method of fusing together these polyhedra is quite intricate. The $[NpO_2F_6]$ units share one edge with an adjacent $[NpO_2F_6]$ unit, one edge with a $[NpO_2F_7]$ polyhedron, and one corner with a second $[NpO_2F_7]$ unit. The $[NpO_2F_7]$ tricapped trigonal prisms share two opposite edges with neighboring $[NpO_2F_7]$ polyhedra, one edge with a $[NpO_2F_6]$ unit, and one corner with a different, but crystallographically equivalent, $[NpO_2F_6]$ unit. This joining of the $[NpO_2F_6]$ distorted dodecahedra and $[NpO_2F_7]$ tricapped trigonal prisms along with the PO_4 tetrahedra, that bridge between two Np(1) and two Np(2) centers, creates a three-dimensional framework structure that has small channels extending along the *a* axis, as is illustrated in Figure 5.4. The Cs^+ cations are not specifically located within these channels, but rather fill other spaces within the framework. The structure can also be described as containing chains of $[NpO_2F_7]$ units that are joined by dimers of $[NpO_2F_6]$.

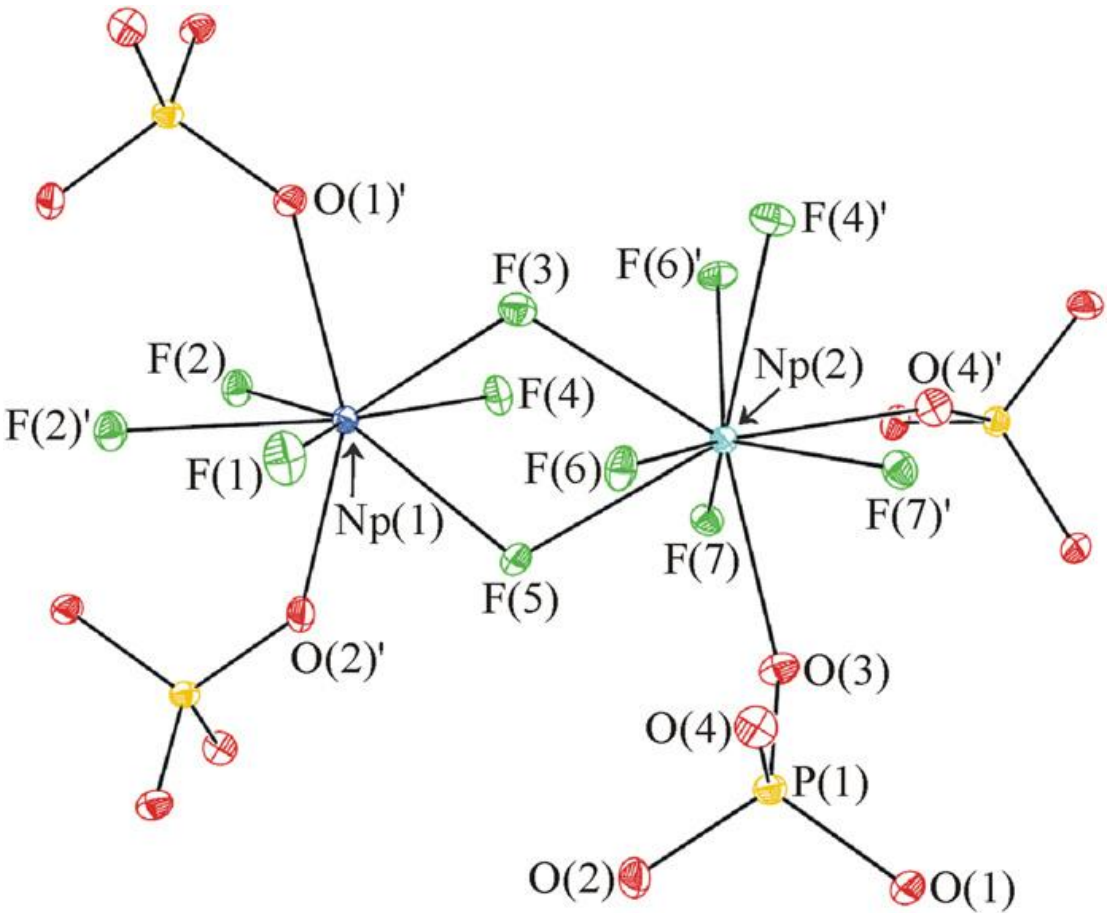

Figure 5.3. A view of the fundamental building units in $Cs_2Np_2F_7PO_4$. Np(1) is present in a distorted dodecahedral environment, and Np(2) in tricapped trigonal prismatic environment. [50% probability ellipsoids are depicted].

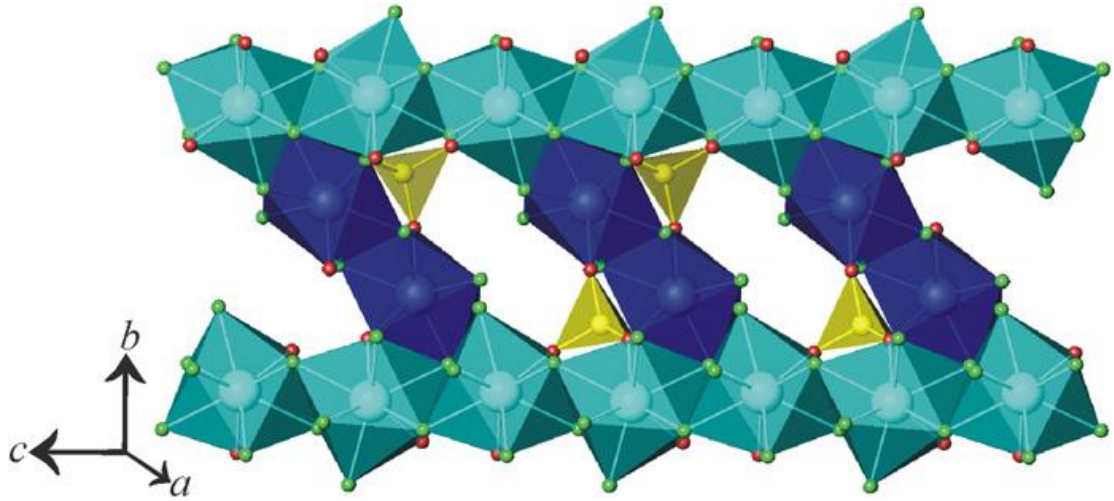

Figure 5.4. An illustration of the $[NpO_2F_6]$ distorted dodecahedra (dark blue) and $[NpO_2F_7]$ tricapped trigonal prisms (light blue), PO_4^{3-} (yellow), and F^- anions (green) that form the structure of $Cs_2Np_2F_7PO_4$.

The two Np(1)–O bond distances are 2.274(4) and 2.294(4) Å. The remaining six Np(1)–F bond distances range from 2.150(3) to 2.355(3) Å. For both Np(1) and Np(2), all of the O and F atoms are bridging except F(1), which is terminal, and thus possesses the shortest bond distance. The Np(2)–O bond distances are 2.282(4) and 2.299(4) Å, which are similar in length to the Np(2)–F bond distances that vary from 2.280(3) to 2.401(3) Å. As in $NpFPO_4$, if the oxygen atoms were not a part of the phosphate anions, they would be essentially indistinguishable from the fluoride anions. However, semi-quantitative EDX measurements also support the presence of F in these crystals. The P–O bond distances are quite regular and range only from 1.532(4) to 1.545(4) Å. The two crystallographically unique Cs^+ cations form a large number of long contacts with surrounding oxygen and fluorine atoms. If an arbitrary cut-off of 3.45 Å is chosen, then there are eight interactions ranging from 2.818(4) to 3.436(3) Å for Cs(1), and eight contacts occurring from 2.817(4) to 3.331(4) Å for Cs(2). Selected bond distances for $Cs_2Np_2F_7PO_4$ are given in Table 5.5.

Table 5.5. Selected bond distances (Å) for $Cs_2Np_2F_7PO_4$.

Distances (Å)			
Np(1)–O(1)	2.294(4)	Np(2)–F(4)	2.370(3)
Np(1)–O(2)	2.274(4)	Np(2)–F(5)	2.401(3)
Np(1)–F(1)	2.150(3)	Np(2)–F(6)	2.280(3)
Np(1)–F(2)	2.299(3)	Np(2)–F(6)'	2.395(3)
Np(1)–F(2)'	2.355(3)	Np(2)–F(7)	2.278(3)
Np(1)–F(3)	2.330(3)	Np(2)–F(7)'	2.382(3)
Np(1)–F(4)	2.320(3)	P(1)–O(1)	1.545(4)
Np(1)–F(5)	2.321(3)	P(1)–O(2)	1.544(4)
Np(2)–O(3)	2.282(4)	P(1)–O(3)	1.535(4)
Np(2)–O(4)	2.299(4)	P(1)–O(4)	1.532(4)
Np(2)–F(3)	2.377(3)		

REFERENCES

1) a) LaChapelle, T. J.; Magnusson, L. B. ; Hindman, J. C. National Nuclear Energy Series, Manhattan Project Technical Section, Division 4: Plutonium Project, **1949**, *14B*, 1097. b) Kimura, T. *J. Radioanal. Nucl. Chem.* **1990**, *139*, 297.

2) There were many Np phosphates prepared that did not appear in the peer-reviewed literature for a considerable time after they were first characterized. See for example: a) Zachariasen, W. H. *Acta Cryst.* **1949**, *2*, 388. b) Nectoux, F.; Tabuteau, A. *Radiochem. Radioanal. Lett.* **1981**, *49*, 43.

3) Bamberger, C. E.; Haire, R. G.; Begun, G. M.; Hellwege, H. E. *J. Less-Common Met.***1984**, *102*, 179.

4) a) Volkov, Yu. F.; Tomilin, S. V.; Orlova, A. I.; Lizin, A. A.; Spiryakov, V. I.; Lukinykh, A. N. *Z. Neorgan. Khim.* **2005**, *50*, 1776. b) Kitaev, D. B.; Volkov, Yu. F.; Orlova, A. I. *Radiochem.* **2004**, *46*, 211. c) Volkov, Yu. F.; Tomilin, S. V.; Orlova, A. I.; Lizin, A. A.; Spiryakov, V. I.; Lukinykh, A. N. *Radiochem.* **2003**, *45*, 319. d) Dacheux, N.; Thomas, A. C.; Chassigneux, B.; Pichot, E. ; Brandel, V. ; Genet, M. *Mater. Res. Soc. Symp. Proc.* **1999**, *556*, 85. e) Dacheux, N.; Thomas, A. C. ; Chassigneux, B.; Pichot, E.; Brandel, V.; Genet, M. *Cer. Trans.* **1999**, *93*, 373. f) Tabuteau, A.; Pages, M.; Livet, J.; Musikas, C. *J. Mater. Sci. Lett.* **1988**, *7*, 1315. g) Begg, B. D.; Vance, E. R.; Conradson, S. D. *J. Alloys Comp.* **1998**, *271-273*, 221. h) Dacheux, N.; Thomas, A. C.; Brandel, V.; Genet, M. *J. Nucl. Mater.* **1998**, *257* 108. i) Volkov, Yu. F. *Radiochem.* **1999**, *41*, 168. j) Wellman, D. M.; Mattigod, S. V.; Parker, K. E.; Heald, S. M.; Wang, C.; Fryxell, G. E. *Inorg. Chem.* **2006**, *45*, 2382.

5) a) Mathur, J. N.; Choppin, G. R. *Radiochim. Acta* **1994**, *64*, 175. b) Morgenstern, A.; Kim, J. I. *Radiochim. Acta* **1996**, *72* 73.

6) *Inorganic Crystal Structure Database (ICSD)*, Fachinformationszentrum, Karlsruhe, **2006**.

7) a) Almond, P. M.; Sykora, R. E.; Skanthakumar, S.; Soderholm, L.; Albrecht-Schmitt, T. E. *Inorg. Chem.* **2004**, *43*, 958. b) Sykora, R. E.; Bean, A. C.; Scott, B. L.; Runde, W.; Albrecht-Schmitt, T. E. *J. Solid State Chem.* **2004**, *177*, 725. c) Bean, A. C.; Scott, B. L.; Albrecht-Schmitt, T. E.; Runde, W. *Inorg. Chem.* **2003**, *42*, 5632. d) Albrecht-Schmitt, T. E.; Almond, P. M.; Sykora, R. E. *Inorg. Chem.* **2003**, *42*, 3788.

8) a) Shvareva, T. Y.; Albrecht-Schmitt, T. E. *Inorg. Chem.* **2006**, *45*, 1900. b) Shvareva, T. Y.; Beitz, J. V.; Duin, E. C.; Albrecht-Schmitt, T. E. *Chem. Mater.* **2005**, *17*, 6219. c) Shvareva, T. Y.; Sullens, T. A.; Shehee; T. C.; Albrecht-Schmitt, T. E. *Inorg. Chem.* **2005**, *44*, 300.

9) Sheldrick, G. M. *SADABS* **2001**, Program for absorption correction using SMART CCD based on the method of Blessing, R. H. *Acta Crystallogr.* **1995**, *A51*, 33.

10) Sheldrick, G. M. SHELXTL PC, Version 6.12, An Integrated System for Solving, Refining, and Displaying Crystal Structures from Diffraction Data; Siemens Analytical X-Ray Instruments, Inc.: Madison, WI **2001**.

11) Lieser, K. H.; Muehlenweg, U.; Sipos-Galiba, I. *Radiochim. Acta.* **1985**, *39*, 35.

12) Sullivan, J. C.; Cohen, D.; Hindman, J. C. *J. Am. Chem. Soc.* **1957**, 79 4029.

13) a) Halasyamani, P. S.; Walker, S. M.; O'Hare, D. *J. Am. Chem. Soc.* **1999**, *121*, 7415. b) Walker, S. M.; Halasyamani, P. S.; Allen, S.; O'Hare, D. *J. Am. Chem. Soc.* **1999**, 121, 10513. c) Almond, P. M.; Deakin, L.; Porter, M. J.; Mar, A.; Albrecht-Schmitt, T. E. *Chem. Mater.* **2000**, *12*, 3208. d) Talley, C. E.; Bean, A. C.; Albrecht-Schmitt, T. E. *Inorg. Chem.* **2000**, *39*, 5174. e) Almond, P. M.; Deakin, L.; Mar, A.; Albrecht-Schmitt, T. E. *J. Solid State Chem.* **2001**, *158*, 87. f) Almond, P. M.; Deakin, L.; Mar, A.; Albrecht-Schmitt, T. E. *Inorg. Chem.* **2001**, *40*, 866. g) Cahill, C. L.; Burns, P. C. *Inorg. Chem.* **2001**, *40*, 1347.

14) a) Magnusson, L. B.; Hindman, J. C.; LaChapelle, T. J. National Nuclear Energy Series, Manhattan Project Technical Section, Division 4: Plutonium Project, **1949**, *14B* (Transuranium Elements, Pt. II), 1134. b) Rotmanov, K. V.; Andreichuk, N. N. *Radiochem.* **2000**, *42*, 569.

15) a) Brown, I. D.; Altermatt, D. *Acta Crystallogr*. **1985**, *B41*, 244. b) Brese, N. E.; O'Keeffe, M. *Acta Crystallogr.* **1991**, *B47*, 192.

CHAPTER 6

SYNTHESIS AND STRUCTURE OF $[C_6H_{14}N_2][(UO_2)_4(HPO_4)_2(PO_4)_2(H_2O)]\cdot H_2O$: AN EXPANDED OPEN-FRAMEWORK AMINE-BEARING URANYL PHOSPHATE

Reproduced with permission from *Journal of Solid State Chemistry*, in press.

Unpublished work copyright 2008 Elsevier.

ABSTRACT

A new open-framework compound, $[C_6H_{14}N_2][(UO_2)_4(HPO_4)_2(PO_4)_2(H_2O)]\cdot H_2O$, (**DUP-1**) has been synthesized under mild hydrothermal conditions. The resulting structure consists of diprotonated $DABCOH_2^{2+}$ ($C_6H_{14}N_2^{2+}$) cations and occluded water molecules occupying the channels of a complex uranyl phosphate three-dimensional lattice. The anionic lattice contains uranophane-like sheets connected by hydrated pentagonal bipyramidal UO_7 units. $[C_6H_{14}N_2][(UO_2)_4(HPO_4)_2(PO_4)_2(H_2O)]\cdot H_2O$ possesses five crystallographically unique U centers. U(VI) is present here in both six- and seven-coordinate environments. The $DABCOH_2^{2+}$ cations are held within the channels by hydrogen bonds to both two uranyl oxygen atoms and a μ_2-O atom. Crystallographic data (193 K, MoKα, λ = 0.71073 Å): **DUP-1**, monoclinic, $P2_1/n$, a = 7.017(1), b = 21.966(4), c = 17.619(3), β = 90.198(3), Z = 4, R(F) = 4.76% for 382 parameters with 6615 reflections with $I > 2\sigma(I)$.

INTRODUCTION

Uranium-containing three-dimensional anionic lattices form a myriad of diverse frameworks primarily because of variability in the coordination environments that are available for the uranium centers.[1] Eight- and nine-coordinate environments are known for U(IV), and six-, seven-, and eight-coordinate environments for U(VI). Several framework uranyl phosphates have been shown to be promising hosts for radionuclides such as ^{90}Sr and ^{137}Cs.[2] In addition, layered uranyl phosphates have been shown to readily undergo ion-exchange reactions.[3] For example, $(BuNH_3)UO_2PO_4{\cdot}3H_2O$ intercalates $[Co(NH_3)_4(CO_3)]^+$, $[Co(NH_3)_5Cl]^{2+}$, and $[Co(NH_3)_6]^{3+}$.[4] More recent results by Paterson-Beedle *et al.*, confirm that the layered hydrogen uranyl phosphate (HUP) does act as an ion-exchanger in the presence of ^{137}Cs, ^{85}Sr, and ^{60}Co.[5]

Organic amines have the ability to template or direct the formation of uranyl-based compounds to form a wide variety of open-framework structures. This is observed in $(C_4H_{12}N_2)U_2O_4F_6$,[6] $(C_4H_{12}N_2)(UO_2)[(UO_2)(PO_4)]_4(H_2O)_2$,[7] $[C_6H_{14}N_2]_2[(UO_2)_6(H_2O)_2F_2(PO_4)_2(HPO_4)_4]{\cdot}4H_2O$,[8] $[(C_2H_5)_2NH_2]_2[(UO_2)_5(PO_4)_4]$,[9] $(UO_2)_{0.82}[C_8H_{20}N]_{0.36}[(UO_2)_6(MoO_4)_7(H_2O)_2](H_2O)_n$ and $[C_6H_{14}N_2][(UO_2)_6(MoO_4)_7(H_2O)_2](H_2O)_m$,[10] $[C_6H_{16}N]_2[(UO_2)_6(MoO_4)_7(H_2O)_2](H_2O)_2$,[11] $[(CH_3)_4N][(C_5H_6N)_{0.8}((CH_3)_3NH)_{0.2}]U_2Si_9O_{23}F_4$,[12] $(NH_4)_4[(UO_2)_5(MoO_4)_7](H_2O)_5$,[13] $[(C_2H_5)_2NH_2]_2[(UO_2)_4(MoO_4)_5(H_2O)](H_2O)$,[14] $[(CH_3)_4N][(UO_2)_2F_5]$,[1e] and $(NH_4)_3(H_2O)_2\{[(UO_2)_{10}O_{10}(OH)][(UO_4)(H_2O)_2]\}$.[15] The simplest example of these, $(C_4H_{12}N_2)U_2O_4F_6$,[6] is constructed solely from UO_2F_5 pentagonal bipyramids (PB) corner-sharing via bridging fluorides to make 10-, 8-, and 6-member rings. Piperazine ($C_4H_{12}N_2$) incorporation into a uranyl phosphate system produces uranophane-type sheets bridged by UO_7 PB's.[7] In the case of $[C_6H_{14}N_2]_2$-

$[(UO_2)_6(H_2O)_2F_2(PO_4)_2(HPO_4)_4]\cdot 4H_2O$, using DABCO ($C_6H_{12}N_2$) instead of ethylene diamine directs the uranyl fluorophosphate network to be constructed from corrugated chains of corner-sharing U_2O_{14} dimers connected by $UO_5F(H_2O)$ pillars.[8] While fluorine here acts to connect these layers through hydrogen bonding, it also effectively excises the layers, thereby reducing overall dimensionality. Interestingly, cooperative efforts of the flexible molybdate oxoanion and the structure directing amine-bearing organic guests yield, not only extended networks with at least one chiral axis, but also a low-temperature phase transition in the compound, $[C_6H_{16}N]_2[(UO_2)_6(MoO_4)_7(H_2O)_2](H_2O)_2$.[9-11] We continue this sect of research and report on the synthesis and structure of the organically templated uranyl phosphate, $[C_6H_{14}N_2][(UO_2)_4(HPO_4)_2(PO_4)_2(H_2O)]\cdot H_2O$ (**DUP-1**), that fits in the above family of extended open-framework compounds.

EXPERIMENTAL

General Information. UO_3 (99.8%, Alfa-Aesar), triethylenediamine (99%, Alfa-Aesar), and H_3PO_4 (85% Fisher Scientific) were used as received. Reactions were run in PTFE-lined Parr 4749 autoclaves with a 23 mL internal volume. Distilled and Millipore filtered water with a resistance of 18.2 MΩ·cm was used in all reactions. Standard precautions were performed for handling radioactive materials during work with UO_3, as well as with reaction products.

$[C_6H_{14}N_2][(UO_2)_4(HPO_4)_2(PO_4)_2(H_2O)]\cdot H_2O$ (DUP-1) Synthesis. UO_3 (286.0 mg, 1.000 mmol), $C_6H_{12}N_2$ (triethylene diamine or DABCO) (22.4 mg, 0.200 mmol), H_3PO_4 (0.3 mL, 5.204 mmol), and 1000 μL of deionized water were loaded into a 23 mL autoclave. The autoclave was sealed and heated to 180 ^oC in a box furnace, and the

temperature was held constant for 3 d. The autoclave was then cooled at an average rate of 9 ^{o}C/h until it reached room temperature. The major product is pale-yellow in color and acicular in habit. X-ray powder diffraction was utilized to compare measure Bragg reflections to a powder pattern generated from single crystal data using the ATOMS 6.0 program. These data show that **DUP-1** is the primary crystalline phase present, with a small amount of residual $C_2H_{12}N_2$ leftover from the initial reaction mixture.

Elemental Analysis. Analyses for carbon, hydrogen, and nitrogen mass percentages were conducted by Atlantic Microlab, Inc. (Theoretical/Actual percentages listed) C: 4.56%/4.60%; H: 1.26%/1.15%; N: 1.77%/1.70%. Qualitative Energy Dispersive X-ray (EDX) microanalyses were performed using a JEOL 7000F field emission Scanning Electron Microscope confirming the presence of Uranium and Phosphorous.

Vibrational Spectroscopy. IR (KBr, cm^{-1}): 912 (ν_1, UO_2^{2+}), 831 (ν_3, UO_2^{2+}), 1123 (ν_3, PO_3^{4-}), 1063 (ν_3, PO_3^{4-}), 1032 (ν_3, PO_3^{4-}), 563 (ν_4, PO_3^{4-}), 513 (ν_4, PO_3^{4-}), 3042(N-H), 2837(N-H), 2733(C-C), 2684(C-C), 2642(C-C), 1466(N-H), 1422, 1325, 626.

Crystallographic Studies. A single crystal of **DUP-1**, with measurements of 0.54 x 0.80 x 0.230 mm^3, was mounted on a glass fiber and optically aligned on a Bruker APEX CCD X-ray diffractometer using a digital camera. Initial intensity measurements were performed using graphite monochromated Mo Kα radiation from a sealed tube and monocapillary collimator. SMART (v 5.624) was used for preliminary determination of the cell constants and data collection control. The intensities of reflections of a sphere were collected by a combination of 3 sets of exposures (frames). Each set had a different

ϕ angle for the crystal and each exposure covered a range of 0.3° in ω. A total of 1800 frames were collected with an exposure time per frame of 30 s.

Determinations of integrated intensities and global refinement were performed with the Bruker SAINT (v 6.02) software package using a narrow-frame integration algorithm. These data were treated with a semi-empirical absorption correction by SADABS.[15] The program suite SHELXTL (v 6.12) was used for space group determination (XPREP), direct methods structure solution (XS), and least-squares refinement (XL).[16] The final refinements included anisotropic displacement parameters for all atoms. Secondary extinction was not noted. Some crystallographic details are given in Table 1. Owing to the structure having a β angle of 90.198(3), ADDSYM and NEWSYM, both parts of the PLATON software, were used to search for missed symmetry. Solids that crystallize in a monoclinic setting with a β-angle so close in proximity to 90^{o} typically show pseudo-orthorhombic symmetry or are twinned. Neither case was detected here. Further details of the crystal structure investigation may be obtained from the Fachinformationzentrum Karlsruhe, D-76344 Eggenstein-Leopoldshafen, Germany (Fax: (+49)7247-808-666; Email: crysdata@fiz-karlsruhe.de).

Thermal Analysis. Thermal data for DUP were collected using a TA Instruments, Model 2920 differential scanning calorimter (DSC) and TA Q50 thermogravimetric analyzer (TGA). Samples, 4.90 mg for DSC and 5.38 mg for TGA, were encapsulated in platinum pans and heated under a nitrogen atmosphere at 20 $^{o}C \cdot min^{-1}$ from 50 to 600 ^{o}C (DSC) and at 10 $^{o}C \cdot min^{-1}$ from 25 ^{o}C to 725 ^{o}C (TGA).

Table 6.1: Crystallographic data for $[C_6H_{12}N_2H_2][(UO_2)_4(HPO_4)_2(PO_4)_2(H_2O)]\cdot H_2O$ (DUP)

Compound	DABCO uranyl phosphate
Formula	$[C_6H_{12}N_2H_2][(UO_2)_4(HPO_4)_2(PO_4)_2(H_2O)]\cdot H_2O$
Color and habit	Yellow acicular prism
Crystal system	Monoclinic
Space group	$P2_1/n$ (No. 14)
a (Å)	7.017(1)
b (Å)	21.966(4)
c (Å)	17.619(3)
β (^{o})	90.198(3)
V (Å^3)	2716.03
Z	4
T(K)	193
λ (Å)	0.71073
Maximum 2θ	56.56
R(int)	0.616
Reflections (total)	25301
Reflections (ind.)	6615
Parameters	382
Weighting Scheme	0.0598
Res. electron den. (min., max.)	-3.21, 4.04
ρ_{calcd} (g cm^{-3})	3.928
μ(Mo Kα) (cm^{-1})	241.2
R(F)[a] for $F_o^2 > 2\sigma(F_o^2)$	0.0476
$R_w(F_o^2)$ [b]	0.1363

[a] $R(F) = \sum \left| |F_o| - |F_c| \right| / \sum |F_o|$. [b] $R_w\left(F_o^2\right) = \left[\sum \left[w\left(F_o^2 - F_c^2\right)^2 \right] / \sum wF_o^4 \right]^{1/2}$.

Powder X-Ray Diffraction. Powder X-ray diffraction patterns were collected with a Rigaku Miniflex powder X-ray diffractometer using Cu Kα (λ = 1.54056 Å) radiation.

RESULTS and DISCUSSION

Structure of $[C_6H_{14}N_2][(UO_2)_4(HPO_4)_2(PO_4)_2]\cdot H_2O$. The title compound contains five crystographically unique uranium sites, three of which are seven coordinate pentagonal bipyramids and two that are six coordinate tetragonal bipyramids. In all cases, the uranium sits in the center of a nearly linear uranyl $[O=U=O]^{2+}$ unit, with bond distances ranging from 1.768(10) Å to 1.795(10) Å. A channel structure ultimately forms from parallel one-dimensional chains of edge-sharing pentagonal bipyramids. Each pentagonal bipyramid also edge shares with a phosphate group. The resulting uranyl phosphate units assemble into one-dimensional chains found in the uranophane anion sheet topology (Fig 2a).[17] The chain is composed of U(4) and U(5) wherein O(11), O(14), O(15), and O(16) are all μ_3 bridging oxygen atoms that serve to construct both the edge-sharing uranyl chain and the individual edge-sharing $UO_2PO_4^-$ units (Fig. 1d). These chains are then connected by bridging $UO_2(PO_4)_2^{4-}$ units (Fig. 2b). Here, the two distinct uranium metal centers, U(1) and U(2) (Figures 1a and 1b, respectively), are both six-coordinate and alternate as the bridging uranium metal center. All axially coordinated oxygen atoms on the UO_2^{2+} metal centers bridge to corner-sharing phosphates. It should also be noted that U(1) and U(2) both sit on an inversion center. The $UO_2(PO_4)_2^{4-}$ unit is formed from the square bipyramidal uranium and two corner sharing trans-phosphate units that join the sheets to form jagged columns along the *b* axis

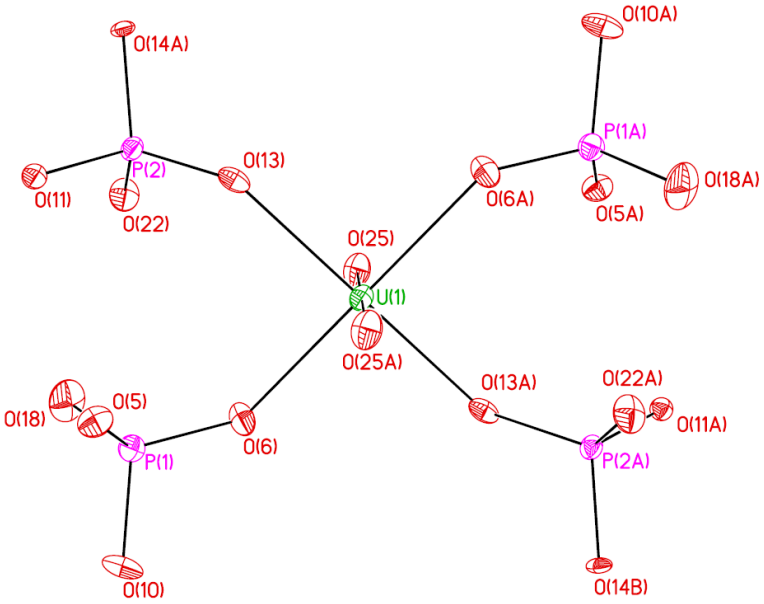

Figure 6.1a. ORTEP of the local environment around U(1). 50% probabilities shown.

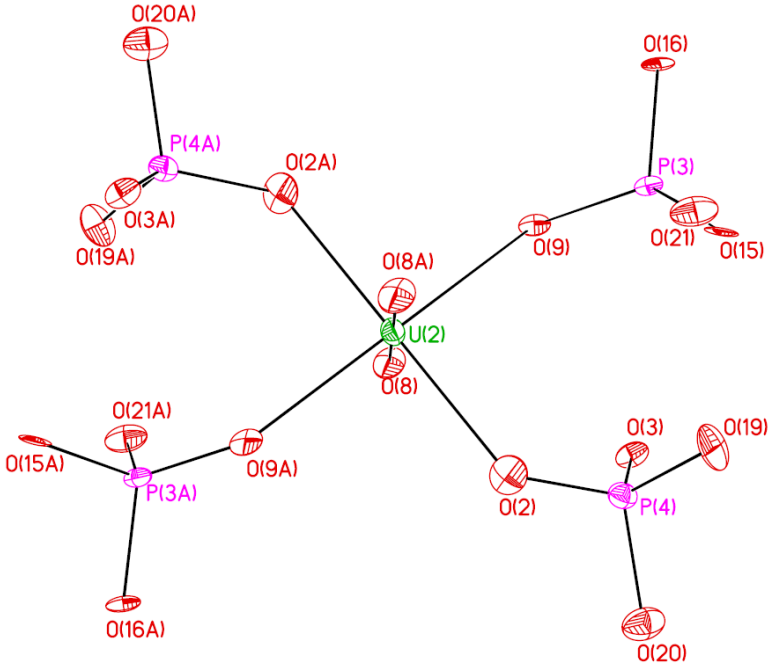

Figure 6.1b. ORTEP of the local environment around U(2). 50% probabilities shown.

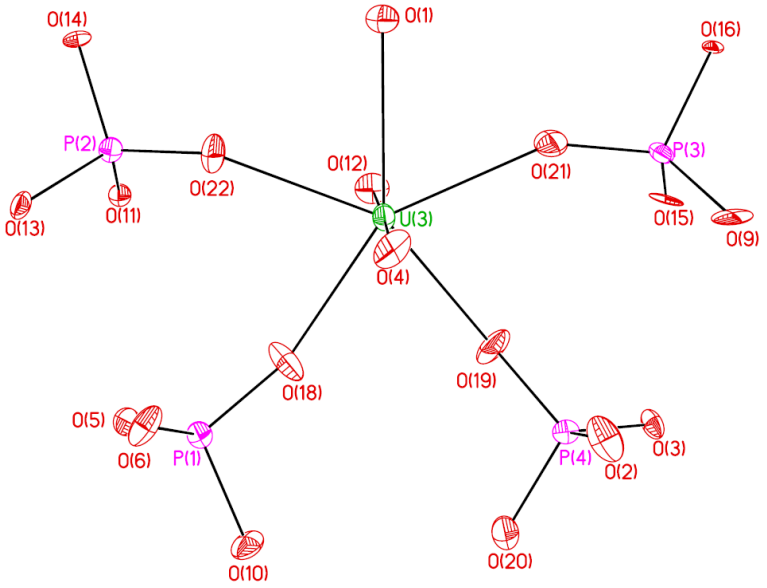

Figure 6.1c. ORTEP of the local environment around U(3). 50% probabilities shown.

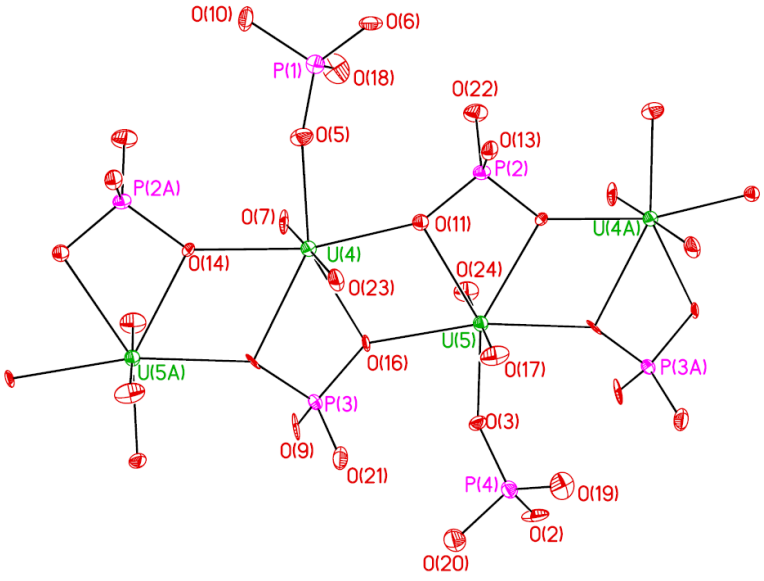

Figure 6.1d. ORTEP of the local environment around the face-sharing U(4) and U(5) metal centers. 50% probabilities shown.

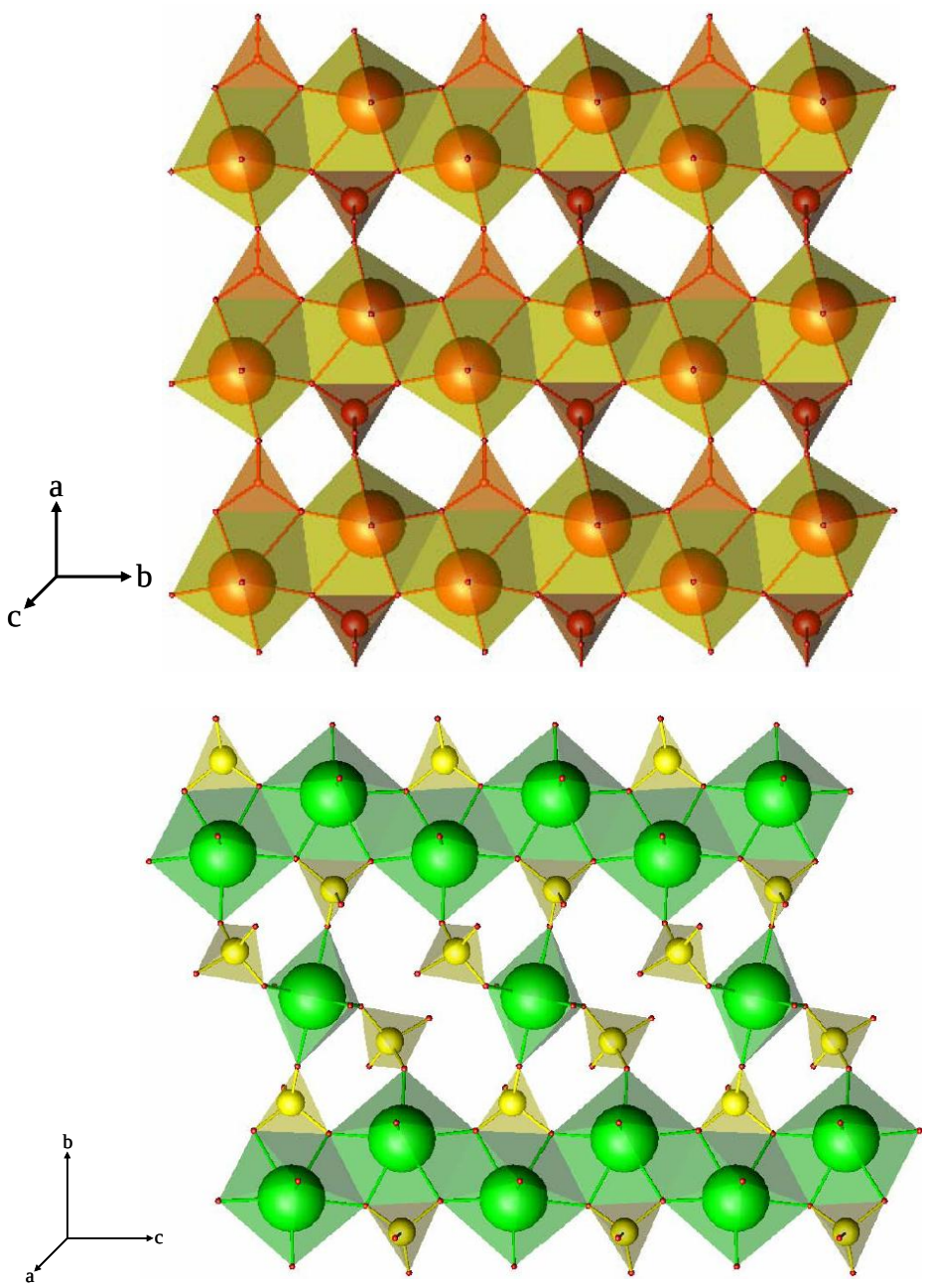

Figure 6.2: View of the (a) β-uranophane sheet topology found in $Ca(H_3O)_2(UO_2)_2(SiO_4)_2(H_2O)_3$ as compared to (b) the delaminated sheets of similar construction found in $[C_6H_{12}N_2H_2][(UO_2)_4(HPO_4)_2(PO_4)_2(H_2O)]\cdot H_2O$

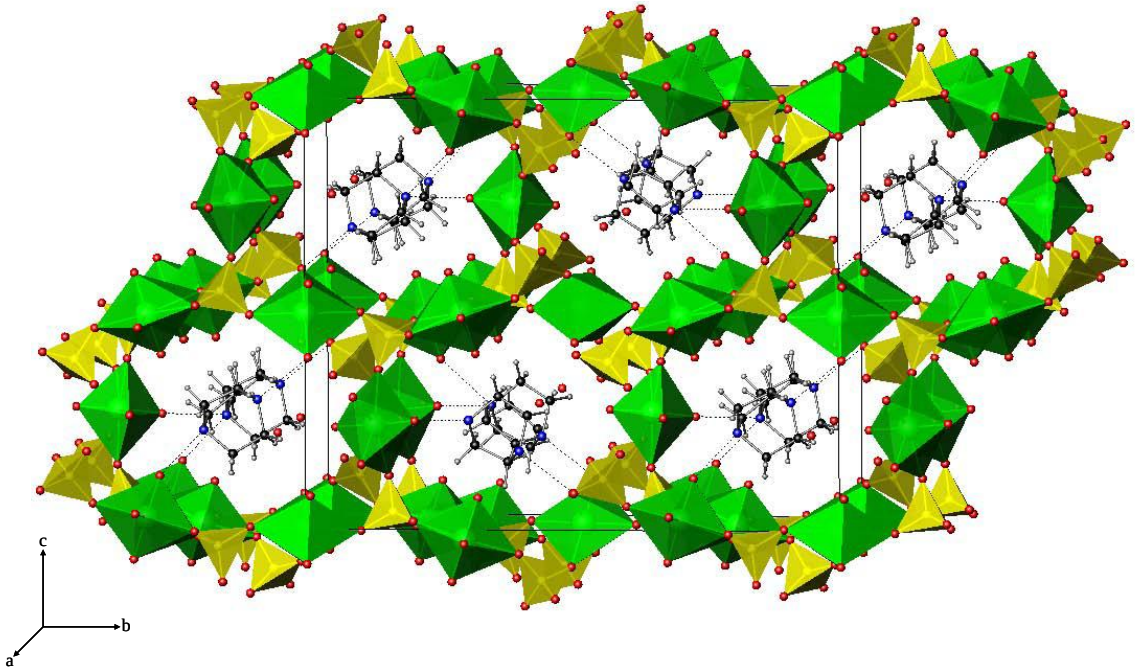

Figure 6.3: Packing diagram of the 3-dimension channels and occluded $DABCOH_2$ and water molecules found in $[C_6H_{12}N_2H_2][(UO_2)_4(HPO_4)_2(PO_4)_2(H_2O)]\cdot H_2O$

(Fig. 2b). As is shown in Figure 3, these constructed layers that extend in the [*ab*] plane are connected by bridging pentagonal bipyramidal unit, formed around the U(3) site (Fig. 1c), to finally produce a three-dimensional structure with channels extending along the *a* axis. Four of the five axial coordination sites for U(3) are used in joining the sheets, while the fifth site is coordinated by a water molecule. This can be confirmed by the lengthened U(3)-O(1) bond length measuring 2.554(10) Å.

The uranyl phosphate lattice is occupied by one crystallograpically unique $DABCOH_2^{2+}$ ($C_6H_{14}N_2$) and an occluded water molecule, both of which are held fixed via hydrogen bonding and shown in the packing diagram. $DABCOH_2^{2+}$ is hydrogen bonded through both ammonium caps. Appropriate hydrogen bond lengths are included in Table 2. The O(26)-O(20) atomic distance of approximately 2.95 Å is of an appropriate length for O(26) to be a water molecule held fast by hydrogen bonding. Based on relative bond lengths, it was determined that two of the four unique phosphates anions are protonated. This is observed in the P(1)-O(21) and the P(4)-O(22) bond lengths.

The three-dimensional channel structure of **DUP-1** can be envisioned as containing the two-dimensional sheets found in uranophane (Fig. 2a),[17] but with delaminated layers spaced by the insertion of $UO_2(PO_4)_2^{4-}$ units. These layers are subsequently joined by the interlaminar pentagonal bipyramids. The resulting pore size of the elliptical three-dimensional channel, created from 12-membered rings laced together by the edge sharing pentagonal bipyramids and measured as the distance between oxygen atoms across the channel, is approx. 5.34 Å x 8.4 Å and extends along the *a* axis. The overall structure is analogous to that found in $[(UO_2)_3(PO_4)_2](H_2O)_4$.[1a]

Table 6.2. Selected bond distances (Å) and angles (^{o}) for $[C_6H_{12}N_2H_2][(UO_2)_4(HPO_4)_2$-$(PO_4)_2(H_2O)]\cdot H_2O$ (DUP).

Distances (Å)			
U(1)–O(6) (× 2)	2.299(10)	P(1)–O(5)	1.505(10)
U(1)–O(13) (× 2)	2.265(10)	P(1)–O(6)	1.526(10)
U(1)–O(25) (× 2)	1.790(10)	P(1)–O(10)	1.569(10)
U(2)–O(2) (× 2)	2.275(10)	P(1)–O(18)	1.492(10)
U(2)–O(8) (× 2)	1.787(10)	P(2)–O(11)	1.561(9)
U(2)–O(9) (× 2)	2.270(10)	P(2)–O(13)	1.523(10)
U(3)–O(1) (H_2O)	2.554(10)	P(2)–O(14)	1.554(9)
U(3)–O(4)	1.768(10)	P(2)–O(22)	1.502(10)
U(3)–O(12)	1.775(10)	P(3)–O(9)	1.517(10)
U(3)–O(18)	2.327(10)	P(3)–O(15)	1.583(9)
U(3)–O(19)	2.320(10)	P(3)–O(16)	1.561(9)
U(3)–O(21)	2.363(10)	P(3)–O(21)	1.493(10)
U(3)–O(22)	2.336(10)	P(4)–O(2)	1.500(10)
U(4)–O(5)	2.277(10)	P(4)–O(3)	1.523(10)
U(4)–O(7)	1.795(10)	P(4)–O(19)	1.495(10)
U(4)–O(11)	2.335(9)	P(4)–O(20)	1.593(11)
U(4)–O(14)	2.349(9)		
U(4)–O(15)	2.476(9)	N(1)–O(6)	2.864(16)

U(4)–O(16)	2.467(9)	N(2)–O(7)	2.914(16)
U(4)–O(23)	1.779(10)	N(2)–O(12)	2.950(17)
U(5)–O(3)	2.241(10)		
U(5)–O(11)	2.511(9)	O(26)–O(20)	2.951(17)
U(5)–O(14)	2.490(9)		
U(5)–O(15)	2.339(9)		
U(5)–O(16)	2.366(8)		
U(5)–O(17)	1.752(9)		
U(5)–O(24)	1.772(10)		

Angles (°)			
O(25)–U(1)–O(25)'	180.0(0)	O(7)–U(4)–O(23)	178.5(5)
O(8)–U(2)–O(8)'	180.0(0)	O(17)–U(5)–O(24)	177.9(5)
O(4)–U(3)–O(12)	177.8(5)		

Phosphuranylite, autunite, and uranophane topologies are very common in the realm of uranyl phosphates.[18] **DUP-1** appears to follow this general motif, but utilizes the different bonding geometries of U(VI) to delaminate and join uranophane sheets resulting in a uranyl phosphate lattice that can encircle the occluded organic ammonium cations. Direct similarities exist between the structure of the title compound presented here and those of $(C_4H_{12}N_2)(UO_2)[(UO_2)(PO_4)]_4(H_2O)_2$,[7] $[(C_2H_5)_2NH_2]_2[(UO_2)_5(PO_4)_4]$,[14] and $[C_6H_{14}N_2]_2[(UO_2)_6(H_2O)_2F_2(PO_4)_2(HPO_4)_4]\cdot 4H_2O$ (**MUPF-1**).[8] In the former two, both structures develop from uranophane sheets with the difference being the coordination environment of the U(VI) metal centers used to fasten the layers together. The latter compound, like **DUP-1**, utilizes DABCO as the structure directing agent but, unlike **DUP**, hydrogen-bonding between layers gives rise to the high-dimensionality. This effect is in striking contrast to those seen in uranyl sulfates, where, upon incremental addition of HF, a zero-dimensional compound first transitions to one-dimensional chains, and ultimately to two-dimensional sheets.[20] Here, we see two compounds synthesized under similar conditions,[21] where the lack of HF results in the crystallization of a three-dimensional uranyl phosphate lattice with enlarged rings and the presence of HF yields a three-dimensional uranyl fluorophosphates with two-dimensional sheets stitched together by hydrogen bonding.

Thermal Behavior. The TGA and DSC thermographs are shown in Figure 4. Monotonic mass loss is seen in the TGA thermal scan until approximately 280 ^{o}C due to steady release of adsorbed water and degassing. Afterwards, a mass loss of 4% correlates with the first significant endotherm centered around 326 ^{o}C, indicative of the release of the interstitial water. Above this temperature exists a double endotherm at 375 ^{o}C and

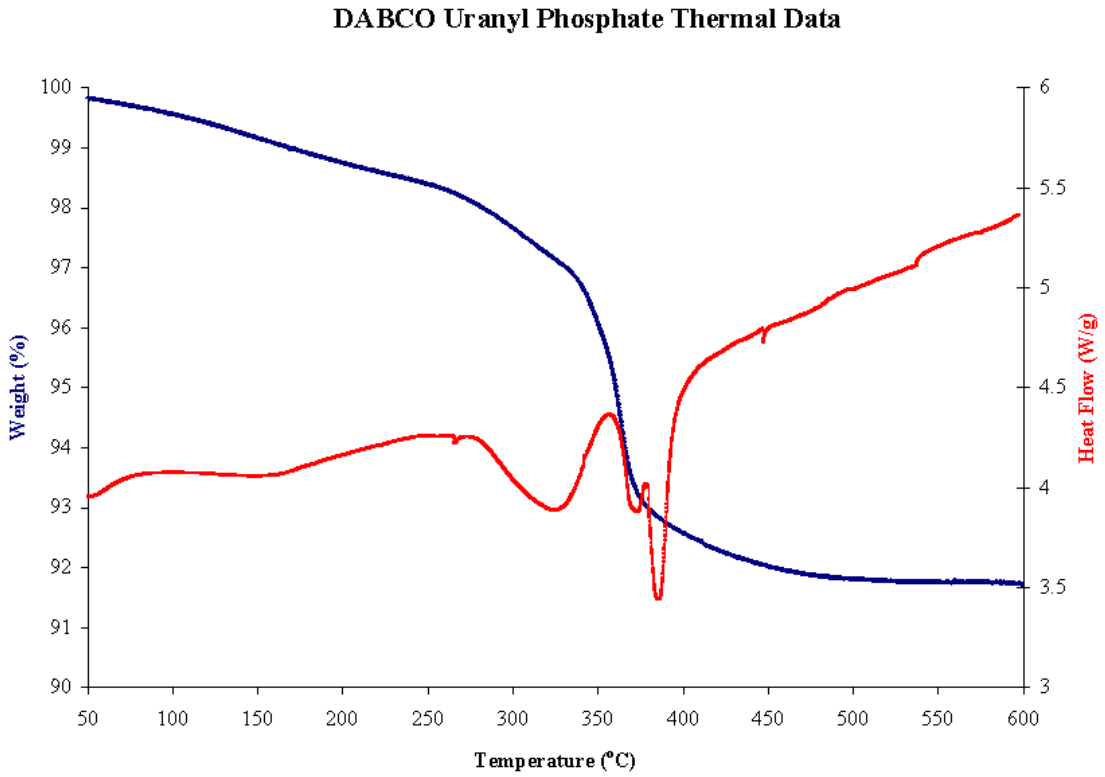

Figure 6.4: TGA and DSC thermograms of $[C_6H_{12}N_2H_2][(UO_2)_4(HPO_4)_2(PO_4)_2\text{-}(H_2O)]\cdot H_2O$

387 ^{o}C, with a larger mass loss, and is realized as a result of the loss of the coordinated water molecule and template degradation. Lattice degeneration may contri-ute to the endotherms in this temperature range as well. These results fit well with published literature.[8,22]

REFERENCES

1) a) Burns, P.C. *Can. Mineral.* **2005**, *43(6)*, 1839. b) Obbade, S.; Dion, C.; Saadi, M.; Yagoubi, S.; Abraham, F. *J. Solid State Chem.* **2004**, *177(11)*, 3909. c) Obbade, S.; Dion, C.; Rivenet, M.; Saadi, M.; Abraham, F. *J. Solid State Chem.* **2004**, *177(6)*, 2098. d) Obbade, S.; Yagoubi, S.; Dion, C.; Saadi, M.; Abraham, F. *J. Solid State Chem.* **2004**, *177(4-5)*, 1681. e) Ok, K.M.; Doran, M.B.; O'Hare, D.; *J. Mat. Chem.* **2006**, *16(33)*, 3366.

2) a) Shvareva, T.Y.; Sullens, T.A.; Shehee, T.C.; Albrecht-Schmitt, T.E. *Inorg. Chem.* **2005**, *44(2)*, 300. b) Shvareva, T. Y.; Skanthakumar, S.; Soderholm, L.; Clearfield, A.; Albrecht-Schmitt, T. E. *Chem. Mat.* **2007**, *19*, 132. c) Ok, K.M.; Doran, M.B.; O'Hare, D. *Dalton Trans.* **2007**, *30*, 3325.

3) Howe, A.T. *Inorg. Ion Exch. Mater.* **1982**, 40.

4) Pozas-Tormo, R.; Moreno-Real, L.; Martinez-Lara, M.; Rodriguez-Castellon, E. *Can. J. Chem*. **1986**, *64(1)*, 35.

5) Paterson-Beedle, M.; Macaskie, L.E.; Lee, C.H.; Hriljac, J.A.; Jee, K.Y.; Kim, W.H. *Hydrometallurgy* **2006**, *83(1-4)*, 141.

6) Halasyamani, P.S.; Walker, S.M.; O'Hare, D. *J. Amer. Chem. Soc.* **1999**, *121(32)*, 7415.

7) Locock, A.J.; Burns, P.C. *J. Solid State Chem.* **2004**, *177(8)*, 2675.

8) Doran, M.B.; Stuart, C.L.; Norquist, A.J.; O'Hare, D. *Chem. Mater.* **2004**, *16(4)*, 565.

9) Danis, A.J.; Runde, W.H.; Scott, B.; Fettinger, J.; Eichhorn, B. *Chem. Comm.* **2001**, *22*, 2378.

10) Krivovichev, S.V.; Burns, P.C.; Armbruster, Th.; Nazarchuk, E.V.; Depmeier, W. *Microporous and Mesoporous Mat.* **2005**, *78(2-3)*, 217.

11) Krivovichev, S.V.; Armbruster, Th.; Chernyshov, D.Y.; Burns, P.C.; Nazarchuk, E.V.; Depmeier, W. *Microporous and Mesoporous Mat.* **2005**, *78(2-3)*, 225.

12) Wang, X.; Huang, J.; Jacobson, A.J. *J. Am. Chem. Soc.* **2002**, *124(51)*, 15190.

13) a) Krivovichev, S. V.; Cahill, C. L.; Burns, P. C. *Inorg. Chem.* **2003**, *42(7)*, 2459. b) Krivovichev, S.V.; Cahill, C.L.; Nazarchuk, E.V.; Burns, P.C.; Armbruster, Th.; Depmeier, W. *Microporous and Mesoporous Mat.* **2005**, *78(2-3)*, 209.

14) Li, Y.; Cahill, C.L.; Burns, P.C. *Chem. Mat.* **2001**, *13(11)*, 4026.

15) Sheldrick, G.M. SADABS 2001, Program for absorption correction using SMART CCD based on the method of Blessing: Blessing, R. H. *Acta Crystallogr.* **1995**, *A51*, 33.

16) Sheldrick, G.M. SHELXTL PC, Version 6.12, An Integrated System for Solving, Refining, and Displaying Crystal Structures from Diffraction Data; Siemens Analytical X-Ray Instruments, Inc.: Madison, WI **2001**.

17) Locock, A.J.; Burns, P.C. *J. Solid State Chem.* **2003**, *176*, 18.

18) Locock, A.J.; Burns, P.C. *J. Solid State Chem.* **2002**, *167*, 226.

20) Doran, M.B.; Cockbain, B.E.; Norquist, A.J.; O'Hare, D. *Dalton Trans.* **2004**, *22*, 3810.

21) Minor differences include the source used for uranium and phosphorous, as well as a difference of 23 ^{o}C in reaction temperatures.

22) Frost, R.L.; Kristóf, J.; Martens, W.N.; Weier, M.L.; Horváth, E. *J. of Therm. Anal. and Calorimetry* **2006**, *83(3)*, 675.

24) Locock, A.J.; Burns, P.C. *Can. Mineral.* **2005**, *43*, 721.

25) Unpublished results.

26) Urbanec, Z.; Mrazek, Z.; Cejka, J. *Thermochimica Acta* **1985**, *93*, 525.

CHAPTER 7

IN SITU HYDROTHERMAL REDUCTION OF Np(VI) AS A ROUTE TO Np(IV) PHOSPHONATE

Reproduced with permission from Bray, Travis H.; Nelson, Anna-Gay D.; Jin, Geng Bang; Haire, Richard G.; Albrecht-Schmitt, Thomas E. *Inorganic Chemistry*, **2007**, *46*, 10959-10961. Copyright 2007 American Chemical Society.

ABSTRACT

A lamellar neptunium(IV) methylphosphonate, $Np(CH_3PO_3)(CH_3PO_3H)(NO_3)$-$(H_2O)\cdot H_2O$, has been prepared under hydrothermal conditions via the *in situ* reduction of Np(VI) to Np(IV). The single crystal structure of this compound shows polar layers that are joined to one another via a hydrogen-bonding network involving interlayer water molecules. The polarity of the orthorhombic space group $Pca2_1$ (a = 10607(3) Å, b = 9.438(3) Å, c = 11.346(4) Å, V (Å^3) = 1135.9(6), Z = 4) found for this compound is consistent with the structure. Magnetic susceptibility measurements demonstrate that the Np(IV) ions are magnetically isolated from one another. Under similar reaction conditions, but with an excess of sodium nitrite, reduction of Np(VI) is impeded and $NpO_2(CH_3PO_3)$ microcrystals precipitate. Crystallographic data: $NpO_2(CH_3PO_3)$, triclinic, space group P-1, a = 6.298(1) Å, b = 6.680(1) Å, c = 7.084(1) Å, α = 90.614(3)^o, β = 99.335(3)^o, γ = 96.500(3)^o, V = 509.0(2) Å^3, Z = 2.

INTRODUCTION

Phosphonates have played a critical role in f-element chemistry primarily from the perspective of their use in separation processes.[1] Many phosphonates have been developed for this purpose including geminally substituted diphosphonic acids that can be grafted to polymer matrixes, e.g. Diphonix resins.[2] Despite the importance of the formation of actinide phosphonates in nuclear waste treatment, little is known about the solid-state structures of these compounds or their physical properties. The only well-developed actinide phosphonate materials are known with thorium[3] and uranium.[4,5] The intricacies of U(VI) phosphonates are aptly illustrated by the uranyl phenylphosphonate system that undergoes a transformation from a *cis* (α-UPP) to *trans* (β-UPP) confirmation at room temperature.[4b,c] Upon exposure to Na^+ or Ca^{2+} cations in an aqueous environment, both of these phases transform from linear chain structures into a hollow nanotubular form, γ-UPP.[4a]

The primary challenge in developing structure-property relationships in actinide phosphonates is that, other than the uranyl compounds, these phases are highly insoluble and generally precipitate as microcrystalline or amorphous powders. As a result, single crystal structure determinations are rare, thus forcing the use of *ab initio* powder diffraction methods when possible.[4h,5] One solution to this conundrum is to utilize reduction processes that transform actinides from the generally more soluble +6 oxidation state to the much less soluble +4 oxidation state. We have discovered that under mild hydrothermal conditions that Np(VI) can be reduced to Np(IV) even in the presence of

certain oxidation agents so long as this process is also driven by the formation of highly insoluble products.[6] We demonstrate that the *in situ* reduction of Np(VI) to Np(IV) can be used to prepare the first well-characterized examples of transuranium phosphonates.

EXPERIMENTAL

General Information. $^{237}NpO_2$ (99.9%, ORNL), methylphosphonate ($CH_3PO_3H_2$ 99.99%, Alfa-Aesar), $NaNO_2$ (98.1%, Fisher) and conc. HNO_3 (conc., Fisher) were used as received. Distilled and Millipore filtered water with a resistance of 18.2 MΩ·cm was used in all syntheses. Reactions were run in Parr 4749 autoclaves with custom-made 10-mL PTFE liners. Np(VI) nitrate stock solution was produced by placing NpO_2 (0.0300 g, 0.111 mmol) and 1000 μL conc. HNO_3 into a 10-mL PTFE-lined autoclave. The autoclave was sealed and placed into a box furnace that had been pre-heated to 180 °C. The reaction vessel was heated for three days and cooled at a rate of 9 °C/h to 23 °C. The resulting nitrate solution was a mixture of Np(V) and Np(VI) salts. All neptunium was oxidized via bubbling with ozone.

All studies were conducted in a laboratory dedicated to studies on transuranium elements using procedures previously described.7 This laboratory is located in a nuclear science facility and is equipped with HEPA-filtered hoods and gloveboxes that are ported directly into the hoods. A series of counters continually monitor radiation levels in the laboratory. The laboratory is licensed by the state of Alabama (a NRC-compliant state) and Auburn University's Radiation Safety Office. All experiments were carried out with approved safety operating procedures. All free-flowing solids are worked with in the

gloveboxes, and solid products are only examined when coated with either water or Krytox oil and water.

$Np(CH_3PO_3)(CH_3PO_3H)(NO_3)(H_2O)\cdot H_2O$ (NpMeP-1) Synthesis. The hydrothermal reaction (180 ºC, autogenously generated pressure, 3 d) of 333 μL of a 0.037 M stock solution of Np(VI) nitrate with methylphosphonic acid results in the formation of clusters of dichroic, pale pink/green crystals of **NpMeP-1** as the only solid product.

$NpO_2(CH_3PO_3)$ (NpMeP-2) Synthesis. The hydrothermal reaction (180 ºC, autogenously generated pressure, 3 d) of 333 μL of a 0.037 M stock solution of Np(VI) nitrate with methylphosphonic acid in the presence of an excess of sodium nitrite results in orange-brown microcrystals.

Crystallographic Studies. Single crystals of NpMeP-1 were selected using a digital microscope with remote viewing capabilities, and were transferred to Krytox oil. Crystals suitable for diffraction studies were mounted on glass fibers with epoxy and optically aligned on a Bruker SMART APEX CCD X-ray diffractometer using a digital camera. Intensity measurements were performed using graphite monochromated MoKα radiation from a sealed tube and monocapillary collimator. SMART (v 5.624) was used for preliminary determination of the cell constants and data collection control. The intensities of reflections of a sphere were collected by a combination of 3 sets of exposures (frames). Each set had a different ϕ angle for the crystal and each exposure covered a range of 0.3° in ω. A total of 1800 frames were collected with an exposure time per frame of 30 s for each compound.

Determination of integrated intensities and global refinement were performed with the Bruker SAINT (v 6.02) software package using a narrow-frame integration algorithm. A face-indexed analytical absorption correction was initially applied using XPREP, where individual shells of unmerged data were corrected analytically. These files were subsequently treated with a semiempirical absorption correction by SADABS.[8] The program suite, SHELXTL (v 6.12), was used for a space group determination (XPREP), direct methods structure solution (XS), and least-squares refinement (XL).[9] The final refinements included anisotropic displacement parameters for all atoms and secondary extinction. Selected crystallographic details are listed in Table 7.1. Atomic coordinates and equivalent isotropic displacement parameters for **NpMeP-1** and **NpMeP-2** are given in Tables 7.2 and 7.3, respectively. X-ray crystallographic files for **NpMeP-1** and **NpMeP-2** in CIF format is available via the Internet at http://pubs3.acs.org/acs/journals/supporting_information.page?in_coden=inocaj&in_volume=46&in_start_page=10959.

Magnetic Susceptibility Measurements. Magnetism data for **NpMeP-1** were measured with a Quantum Design MPMS 7T magnetometer/susceptometer between 5 and 300 K under an applied magnetic field of 0.1 T. Susceptibility values were corrected for the sample diamagnetic contribution according to Pascal's constants,[10] as well as for the sample holder diamagnetism.

Table 7.1. Crystallographic data for $Np(CH_3PO_3)(CH_3PO_3H)(NO_3)(H_2O)\cdot H_2O$ and $NpO_2(CH_3PO_3)$

Formula	$Np(CH_3PO_3)(CH_3PO_3H)(NO_3)(H_2O)\cdot H_2O$	$NpO_2(CH_3PO_3)$
Formula mass (amu)	522.04	363.00
Crystal System	Orthorhombic	Triclinic
Space group	*P*ca2$_1$ (No. 29)	*P*-1 (No. 2)
a (Å)	10.607(3)	6.298(1)
b (Å)	9.438(3)	6.680(1)
c (Å)	11.346(4)	7.084(1)
V (Å^3)	1135.9(6)	292.05(8)
Z	4	2
α (^{o})	90.00	90.614(3)
β (^{o})	90.00	99.335(3)
γ (^{o})	90.00	96.500(3)
T (°C)	-80	-80
λ (Å)	0.71073	0.71073
ρ_{calcd} (g cm^{-3})	3.053	4.128
μ(Mo *K*α) (cm^{-1})	94.82	180.01
R(*F*) for $F_o^2 > 2\sigma(F_o^2)$ [a]	0.0193	0.0469
$R_w(F_o^2)$ [b]	0.0432	0.0683

[a] $R(F) = \sum \left| |F_o| - |F_c| \right| / \sum |F_o|$. [b] $R_w(F_o^2) = \left[\sum \left[w(F_o^2 - F_c^2)^2 \right] / \sum w F_o^4 \right]^{1/2}$.

Table 7.2. Atomic coordinates and equivalent isotropic displacement parameters for $Np(CH_3PO_3)(CH_3PO_3H)(NO_3)(H_2O)\cdot H_2O$.

atom	*x*	*y*	*z*	U_{eq}(Å^2)[a]
Np1	-0.074187(11)	0.047357(12)	1.51479(3)	0.01045(5)
P1	-0.14798(10)	0.11509(11)	1.21053(9)	0.0118(2)
P2	-0.27982(10)	-0.24122(11)	1.43573(10)	0.0148(2)
N1	-0.0941(4)	0.3515(5)	1.5868(4)	0.0198(8)
O1	-0.0302(3)	0.0389(3)	1.1661(3)	0.0195(7)
O2	-0.2615(3)	0.0785(3)	1.1357(3)	0.0183(6)
O3	-0.1739(3)	0.0764(3)	1.3402(3)	0.0142(6)
O4	-0.2988(3)	-0.3910(3)	1.4952(4)	0.0232(9)
O5	-0.4050(3)	-0.1664(4)	1.4434(3)	0.0213(7)
O6	-0.1730(3)	-0.1661(3)	1.4979(3)	0.0178(7)
O7	-0.1068(4)	0.4747(4)	1.6191(4)	0.0275(8)
O8	-0.1424(3)	0.3073(3)	1.4933(3)	0.0217(8)
O9	-0.0327(3)	0.2644(3)	1.6488(3)	0.0222(7)
O10	0.0627(3)	-0.1172(4)	1.4119(3)	0.0204(7)
O1W	0.0405(5)	0.6001(5)	1.3837(4)	0.0360(9)
C1	-0.1188(5)	0.2994(5)	1.2044(4)	0.0239(9)
C2	-0.2446(6)	-0.2718(5)	1.2858(4)	0.0250(12)

[a] U_{eq} is defined as one-third of the trace of the orthogonalized U_{ij} tensor.

Table 7.3. Atomic coordinates and equivalent isotropic displacement parameters for $NpO_2(CH_3PO_3)$.

atom	*x*	*y*	*z*	U_{eq}(Å ^{2})[a]
Np1	Np	0.02107(7)	-0.14268(5)	-0.24778(5)
P1	P	-0.0788(4)	-0.6890(3)	-0.2580(3)
C1	C	-0.3641(18)	-0.6750(16)	-0.2932(19)
O1	O	-0.2599(12)	-0.1942(10)	-0.2934(10)
O2	O	0.3003(12)	-0.0884(10)	-0.2036(10)
O3	O	-0.0183(10)	0.1803(8)	-0.0815(8)
O4	O	0.0247(12)	-0.1783(9)	-0.5795(9)
O5	O	0.0463(11)	-0.4822(9)	-0.2417(9)

[a] U_{eq} is defined as one-third of the trace of the orthogonalized U_{ij} tensor.

RESULTS AND DISCUSSION

Structural Features of $Np(CH_3PO_3)(CH_3PO_3H)(NO_3)(H_2O)\cdot H_2O$.

Single crystal X-ray diffraction studies on **NpMeP-1** reveal a layered structure constructed from corner-sharing NpO_8 distorted dodecahedra that are bridged by $CH_3PO_3^{2-}$ and $CH_3PO_3H^{1-}$ anions. The coordination sphere is completed by a chelating nitrate anion and a coordinating water molecule. These units form layers that extend in the [*ac*] plane. As indicated by the orthorhombic space group $Pca2_1$, the structure is polar. The polarity of **NpMeP-1** is subtle. A portion of the structure of **NpMeP-1** is shown in Figure 7.1. The hydrogen atoms from the interlayer water molecules as well as those on the $CH_3PO_3H^{1-}$ anions were located from difference maps. The nitrate and $CH_3PO_3H^{1-}$ anions form a hydrogen bonding network that stitches the layers together and provides stability for the overall structure. Both the hydrogen bonding network and the tilt of the nitrate anions can be used to visualize the polarity of the structure along the *c* axis. The structure of **NpMeP-1** does not parallel that of other M(IV) phosphonates.

The NpO_8 distorted dodecahedra have Np–O bond distances that range from 2.199(3) to 2.589(3) Å, yielding a bond-valence sum of 4.07, which is consistent with this compound containing Np(IV).[11] The P–O bond distances are normal, and the only one worth mentioning is the longest one of 1.579(4) Å that corresponds to a P–OH moiety in the $CH_3PO_3H^{1-}$ anions. Remaining selected bond distances are listed in Table 7.4.

The beauty of utilizing Np as the core metal ion in phosphonate materials is the ability to tune the oxidation state of the neptunium as demonstrated by the formation of **NpMeP-1**. By using a large excess of nitrite in the aforementioned reaction, the

Table 7.4. Selected bond distances (Å) and angles (^{o}) for $Np(CH_3PO_3)(CH_3PO_3H)$-$(NO_3)(H_2O)\cdot H_2O$.

Distances (Å)			
Np(1)–O(1)	2.199(3)	P(1)–O(1)	1.527(4)
Np(1)–O(2)	2.238(3)	P(1)–O(2)	1.513(3)
Np(1)–O(3)	2.262(3)	P(1)–O(3)	1.541(3)
Np(1)–O(5)	2.267(3)	P(1)–C(1)	1.768(5)
Np(1)–O(6)	2.278(3)	P(2)–O(4)	1.579(4)
Np(1)–O(8)	2.570(3)	P(2)–O(5)	1.506(3)
Np(1)–O(9)	2.589(3)	P(2)–O(6)	1.512(3)
Np(1)–O(10)	2.425(3)	P(2)–C(2)	1.766(5)
		N(1)–O(7)	1.227(5)
		N(1)–O(8)	1.250(5)
		N(1)–O(9)	1.263(5)

Table 7.5. Selected bond distances (Å) and angles (^{o}) for $NpO_2(CH_3PO_3)$.

Distances (Å)			
Np(1)-O(1)	1.740(7)	P(1)-O(3)	1.553(6)
Np(1)-O(2)	1.731(7)	P(1)-O(4)	1.550(6)
Np(1)-O(3)	2.351(6)	P(1)-O(5)	1.505(7)
Np(1)-O(3)	2.503(5)	P(1)-C(1)	1.787(11)
Np(1)-O(4)	2.363(6)		
Np(1)-O(4)	2.502(6)		
Np(1)-O(5)	2.292(6)		

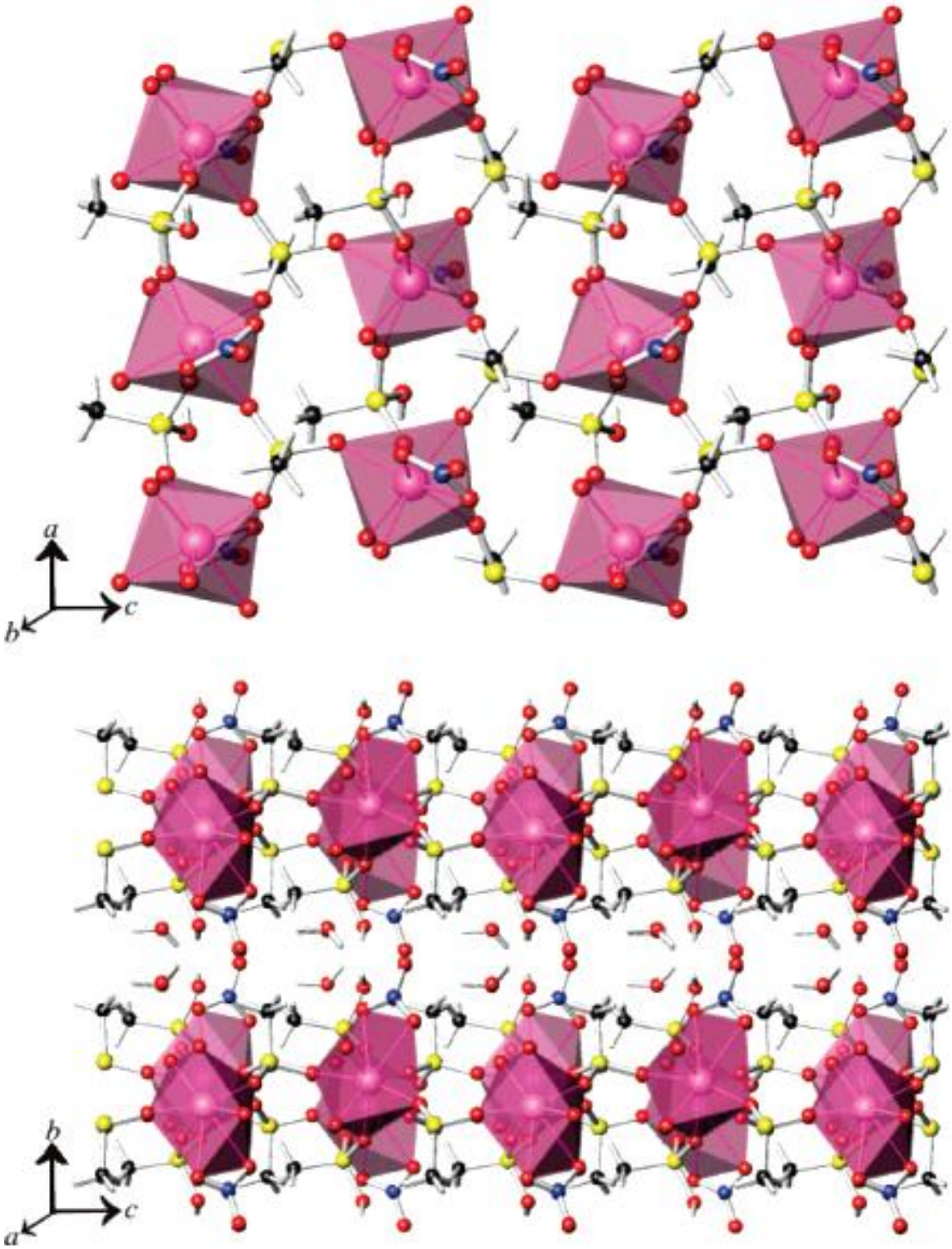

Figure 7.1. Views down the *b* and *a* axes of the polar, lamellar structure of **NpMeP-1**.

Color code: NpO_8, pink; P, yellow; O, red; N, blue; H, white

oxidation state of Np can be maintained at +6,[12] enabling the isolation of the Np(VI) methylphosphonate, $NpO_2(CH_3PO_3)$ (**NpMeP-2**) as orange-brown microcrystals. A view of part of the structure of **NpMeP-2** is shown in Figure 3. This lamellar compound is isostructural with its U(VI) analog.[4h] However, the structure of $UO_2(CH_3PO_3)$ was obtained from high-resolution, powder X-ray diffraction data.[4h] Selected bond distances for NpMeP-2 are listed in Table 7.5.

Despite the very small size (largest dimension ~2 μm) of the crystals of **NpMeP-2**, the use of a single crystal X-ray diffractometer with a CCD detector with long exposure times allowed for the elucidation of a high-resolution structure for **NpMeP-2**. The structure of this compound consists of NpO_7 pentagonal bipyramids containing a nearly linear NpO_2^{2+} neptunyl core. The critical bond distances are the two neptunyl Np=O bonds that average 1.736(7) Å. This distance is statistically shorter than that typically found in uranyl compounds, which averages 1.79(3) Å.[13] The NpO_7 pentagonal bipyramids form one-dimensional chains via edge-sharing, and are in turn bridged by $CH_3PO_3^{2-}$ anions to yield layers that extend in the [*bc*] plane. The methyl groups are oriented approximately perpendicular to this plane and point between the layers, as shown in Figure 7.2.

Magnetic Properties of $Np(CH_3PO_3)(CH_3PO_3H)(NO_3)(H_2O)\cdot H_2O$. The isolation of **NpMeP-1** as a pure crystalline material and subsequent structural characterization allows us to address potential structure-property correlations. In particular the magnetic properties of Np(IV) compounds can be particularly intriguing because of its $5f^3$ electron configuration that has a $^4I_{9/2}$ ground state. The magnetic behavior of Np(IV) compounds sharply contrasts with that of U(IV) ($5f^2$, $^3H_4$)

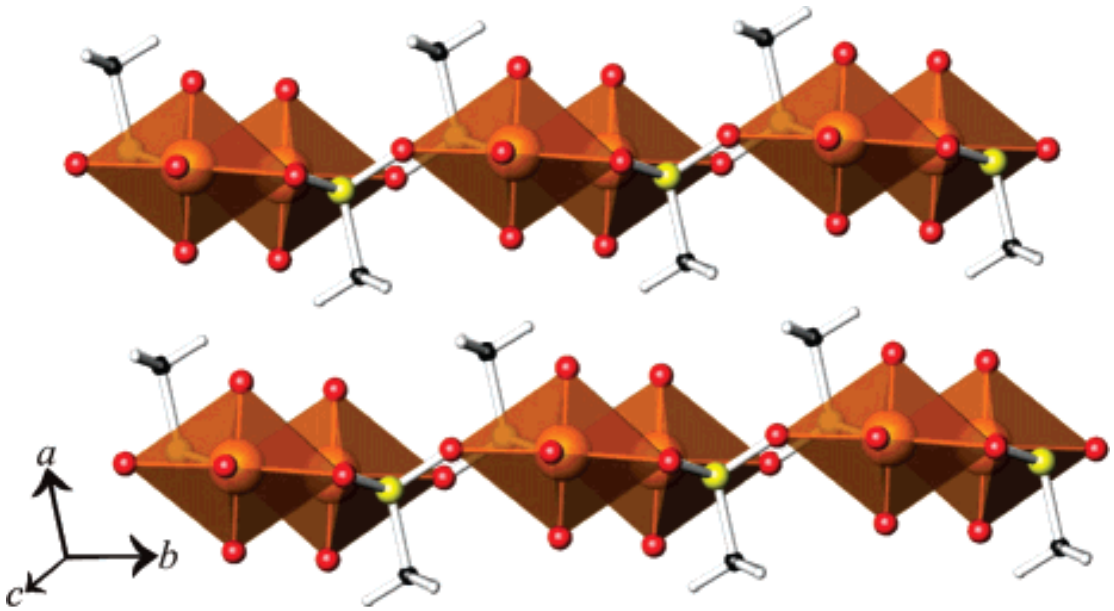

Figure 7.2. View down the *c* axis of the layered structure of the neptunium-(VI) methyl-phosphonate **NpMeP-2**. Color code: NpO7 pentagonal bipyramids,orange; P, yellow; O, red; H, white.

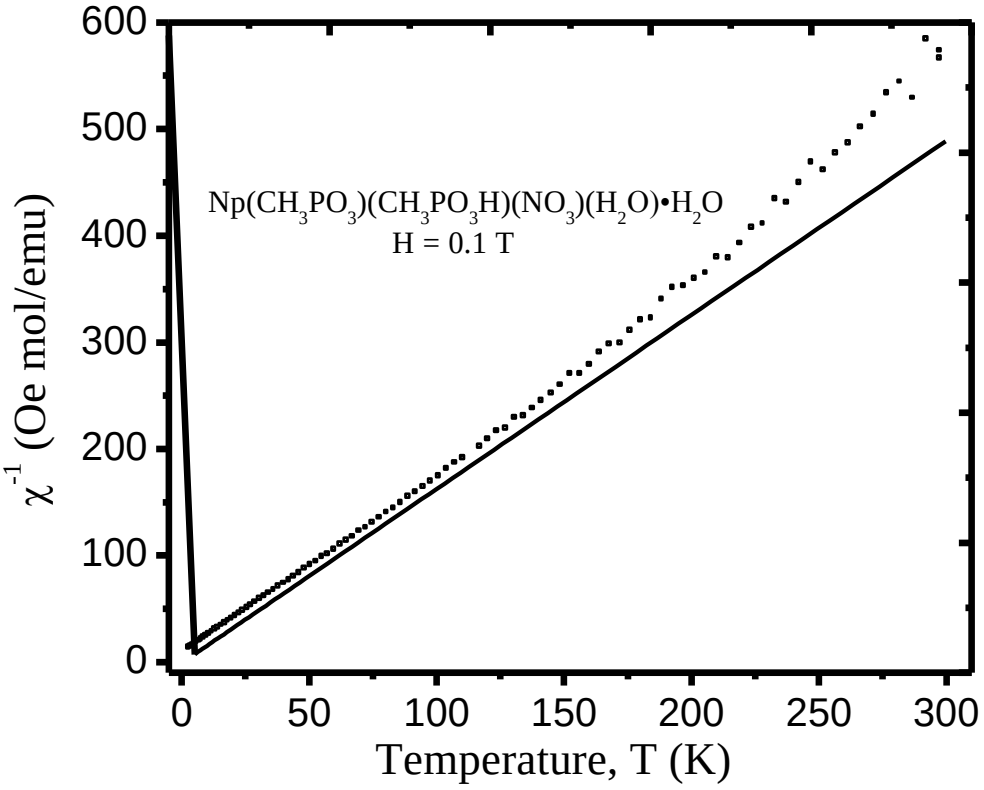

Figure 7.3. Temperature dependence of the reciprocal molar magnetic susceptibility for **NpMeP-1** under an applied magnetic field of 0.1 T between 5 and 300 K. The straight line represents the fit to the Curie-Weiss law in the range of 5-100 K.

compounds that have a tendency of becoming non-magnetic or only exhibiting temperature independent paramagnetism (TIP) at low-temperatures owing to a singlet ground state. The Np···Np distance is greater than 5.3 Å in **NpMeP-1**, and there are no μ_3-oxo groups in the structure, and therefore no opportunity for super-exchange. Therefore, the prediction is that the Np(IV) centers will behave as isolated ions, and Curie-Weiss behavior should be observed without long-range magnetic ordering. The inverse magnetic susceptibility is plotted versus temperature in Figure 7.3. As can be observed from these data, this prediction proves to be true as Curie-Weiss behavior is exhibited at low-temperatures. The susceptibility data were least squares fit to $\chi(T) = C/(T + \theta) + \chi_0$ where C is the Curie constant, θ is the Weiss constant and χ_0 is the temperature independent susceptibility. We have fit the data from 5 to 100 K to arrive at a θ value of 0.53(6) K, indicating no strong interactions between Np(IV) ions. The value of μ_{eff} is 2.213(1) μ_B. While this value is considerably lower than that predicted for the free-ion (3.62 μ_B), it compares well with other Np(IV) compounds such as $Np(IO_3)_4$ (2.22 μ_B).[6] This reduced moment is not a reflection of covalency of the 5f orbitals, but rather arises from crystal-field effects.[6]

REFERENCES

1) a) Nash, K. L. *J. Alloy and Cmpd.* **1997**, *249*, 33. b) Jensen, M. P.; Beitz, J. V.; Rogers, R. D.; Nash, K. L. *J. Chem. Soc., Dalton Trans.* **2000**, *18*, 3058.

2) Chiarizia, R.; Horwitz, E. P.; Alexandratos, S. D.; Gula, M. J. *Sep. Sci. Tech.* **1997**, *32*, 1.

3) Dines, M. B.; DiGiacomo, P. M. *Inorg. Chem.* **1981**, *20*, 92.

4) a) Grohol, D.; Clearfield, A. *J. Am. Chem. Soc.* **1997**, *119*, 9301. b) Grohol, D.; Clearfield, A. *J. Am. Chem. Soc.* **1997**, *119*, 4662. c) Grohol, D.; Subramanian, M. A.; Poojary, D. M.; Clearfield, A. *Inorg. Chem.* **1996**, *35*, 5264. d) Poojary, D. M.; Cabeza, A.; Aranda, M. A. G.; Bruque, S.; Clearfield, A. *Inorg. Chem.* **1996**, *35*, 5603. e) Poojary, D. M.; Grohol, D.; Clearfield, A. *Angew. Chem., Int. Ed. Engl.* **1995**, *34*, 1508. f) Poojary, D. M.; Grohol, D.; Clearfield, A. *J. Phys. Chem. Solids* **1995**, *56*, 1383. g) Britel, A.; Wozniak, M.; Boivin, J. C.; Nowogrocki, G.; Thomas, D. *Acta Crystallogr.* **1986**, *C42*, 1502. h) Grohol, D.; Clearfield, A. *Inorg. Chem.* **1999**, *38*, 751. i) Doran, M. B.; Norquist, A. J.; O'Hare, D. *Chem. Mater.* **2003**, *15*, 1449.

5) Cabeza, A.; Aranda, M. A. G.; Cantero, F. M.; Lozano, D.; Martínez-Lara, Bruque, S. *J. Solid State Chem.* **1996**, *121*, 181.

6) Bray, T. H.; Ling, J.; Choi, E.-S.; Brooks, J. S.; Beitz, J. V.; Sykora, R. E.; Haire, R. G.; Stanbury, D. M.; Albrecht-Schmitt, T. E. *Inorg. Chem.* **2007**, *46*, 3663.

7) a) Almond, P. M.; Sykora, R. E.; Skanthakumar, S.; Soderholm, L.; Albrecht-Schmitt, T. E. *Inorg. Chem.* **2004**, *43*, 958. b) Sykora, R. E.; Bean, A. C.; Scott, B. L.; Runde, W.; Albrecht-Schmitt, T. E. *J. Solid State Chem.* **2004**, *177*, 725.

c) Bean, A. C.; Scott, B. L.; Albrecht-Schmitt, T. E.; Runde, W. *Inorg. Chem.* **2003**, *42*, 5632. d) Albrecht-Schmitt, T. E.; Almond, P. M.; Sykora, R. E. *Inorg. Chem.* **2003**, *42*, 3788.

8) Sheldrick, G. M. SADABS **2001**, Program for absorption correction using SMART CCD based on the method of Blessing, R. H. *Acta Crystallogr.* **1995**, *A51*, 33.

9) Sheldrick, G. M. SHELXTL PC, Version 6.12, An Integrated System for Solving, Refining, and Displaying Crystal Structures from Diffraction Data; Siemens Analytical X-Ray Instruments, Inc.: Madison, WI **2001**.

10) Mulay, L. N.; Boudreaux, E. A. *Theory and Applications of Molecular Diamagnetism*; Wiley–Interscience: New York, 1976.

11) a) Brese, N. E.; O'Keeffe, M. *Acta Crystallogr.* **1991**, *B47*, 192. b) Brown, I. D. *The Chemical Bond in Inorganic Chemistry: The Bond Valence Model*; Oxford University Press, 2002.

12) Nagasaki, S.; Kinoshita, K.; Wisnubroto, D. S.; Enokida, Y.; Suzuki, A. *J. Nucl. Sci. Tech.* **1992**, *29*, 671.

13) Burns, P. C. *Can. Mineral.* **2005**, *43*, 1839.

CHAPTER 8

SUMMARY

In chapter two, the preparation and crystallization, in high yield, of the first molecular uranyl iodate is demonstrated. This is also the first reported polar uranyl iodate. Concomitant formation of intermolecular hydrogen bonds and iodate···iodate interactions align the lone-pair of electrons on the iodate anions to yield a polar structure. One key issue that this and previous studies[1] indicates is that the alkali metals influence what kind of products can be isolated, *i.e.* they play different structure-directing roles despite all having the same shape. While K^+, Rb^+, and Tl^+ all yield the same uranyl iodate architecture in $A_2[(UO_2)_3(IO_3)_4O_2]$ (A = K, Rb, Tl),[1f,1g] the Cs^+ analog of these compounds has yet to be isolated, despite repeated attempts over the years. Instead $Cs_2[(UO_2)_3Cl_2(IO_3)(OH)O_2]\cdot 2H_2O$ is crystallized from reactions with high CsCl concentrations.[1c] Here, we see that the presence of the small Na^+ cation, in conjunction with the ability of the iodate anion to reduce the overall dimensionality of a solid structure, allows for the isolation of a uranyl iodate anion, which has yet to be isolated from reactions with different cations.

Chapter three presents synthetic and structural data for $An(IO_3)_4$ (An = Np, Pu) and $Np(IO_3)_4\cdot nH_2O\cdot nHIO_3$, as well as the magnetic data for $Np(IO_3)_4$, through which new avenues for addressing the reactivity, structures, and properties of transuranic compounds are provided. The use of hydrothermal conditions with smaller amounts of water than

that typically employed gives access to pure compounds in the form of single crystals that have not been previously available from nonhydrothermal synthetic techniques. In a general sense, the actinide chemistry presented here can be considered as being a part of a larger synthetic methodology wherein redox reactions are used to control the introduction of ions that lead to the slow crystallization of highly insoluble products.[2] This gradual introduction of reactants facilitates crystal growth of compounds that normally only form microcrystalline or amorphous powders and yields the first reaction schemes to systematically precipitate neptunium iodate compounds in a specific oxidation state. In addition, the conditions under which these reactions were performed more closely relate to those that may be found in the immediate vicinity of compromised storage vessel cladding.

The first Pu^{4+} selenite, $Pu(SeO_3)_2$, is reported in chapter four. We demonstrate that its overall structure is isotypic with its Ce^{4+} analog and can be described as one-dimensional chains of edge-sharing $[PuO_8]$ units extending down the *a* axis, interconnected by selenite anions to form a dense, three-dimensional structure. The local symmetry around the Pu^{4+} cations, which is crystallographically C_1, is most closely approximated by an idealized C_{2v} bicapped trigonal prism.

The magnetic susceptibility of $Pu(SeO_3)_2$ is complex and not consistent with the predicted singlet, crystal-field ground state but rather by a degenerate ground state. The combined structural and effective moment data are consistent with Pu^{4+}. An intriguing feature of several Pu^{4+} compounds is their rather large Weiss constants that argue in favor of strong magnetic correlations without any indication of long-range magnetic ordering

down to the lowest temperatures studied. This lack of ordering might be ascribed to the long Pu···Pu distance of 3.9723(7) Å in $Pu(SeO_3)_2$.[3]

The purpose of the work discussed in chapter five is not only to report the synthesis and structure of two new Np(IV) fluorophosphates, but also to use these compounds as a way to new synthetic and structural chemistry motifs with Np(IV). There are only a handful of reported single crystal structures for Np(IV) compounds, and there may be problems with the metrics in some of the previously reported systems given these valence band considerations. These compounds provide standards for Np(IV)–O and Np(IV)–F bond distances that should be useful in future work. The work here provides insight into *in-situ* product evolution that transpires under hydrothermal conditions.[4]

The vast majority of uranyl phosphates and arsenates crystallize with topologies based on autunite or uranophane-type sheets, primarily due to the thermostability inherent in these systems. This is especially true when +2 cations are incorporated into these matrices, as Ca^{2+}, Sr^{2+}, and Ba^{2+} all yield autunite-type sheet structures.[5] In fact, both 2,2'- and 4,4'-bipyridyl uranyl phosphate show the same trend as the alkaline earth metal uranyl phosphates.[6] In chapter six that the structure-directing ability of DABCO is shown to differ. While $(C_6H_{14}N_2)(UO_2)(AsO_4)_2(H_2O)_3$ precipitates as autunite-type sheets with interlamellar $DABCOH_2^{2+}$ units, in basically the same way as AE^{2+} (AE = Ca, Sr, Ba, 2,2'- and 4,4'-bipyridyl) uranyl phosphates, we see a distinction made here in that **DUP-1** and MUFP-1 both utilize a uranyl phosphate anionic lattice to encapsulate the protonated DABCO units rather than simply intercalate the organic amine cations. Regardless, as a testament to its stability, the β-uranophane-type sheet is the basic

building block for the **DUP-1** 3-D channel-structure. Comparison of the thermal analyses of **DUP-1** with those of β-uranophane reveals similar characteristics in both the TGA and the DSC. Not surprisingly, due to the interstitching of layers, the endotherms seen in the DSC scan of **DUP-1** come at higher temperatures than in that of β-uranophane.[7]

Chapter seven provides the first report on structure-property relationships in transuranium phosphonates. The redox demonstrated capabilities of neptunium, which are *not* paralleled by uranium or other lighter actinides, provide access to new Np(IV) and Np(VI) phosphonates. Np(V) phosphonates should also be available in the near future. The high coordination numbers of Np in these compounds provide access to structural motifs not available from transition metal phosphonate materials.[8]

General conclusions can be made regarding the chemistry presented here. Hydrothermal synthesis proves to be an excellent method to produce single crystals of actinide compounds while minimizing exposure to radioactive chemicals. Selenite, iodate, and phosphonate anions have a tendency to form compounds of low dimensionality. Also, solubility driven reduction of hexavalent Np and Pu to the tetravalent oxidation state proves to be a consistent method to control precipitation in order to attain single crystals.

REFERENCES

1) a) Weigel, F.; Engelhardt, L. W. H. *J. Less-Common Met.* **1983**, *91*, 339. b) Bean, A. C.; Peper, S. M.; Albrecht-Schmitt, T. E. *Chem.Mater.* **2001**, *13*, 1266. c) Bean, A. C.; Xu, Y.; Danis, J. A.; Albrecht-Schmitt, T. E.; Runde, W. *Inorg. Chem.* **2002**, *41*, 6775. d) Sykora, R. E.; McDaniel, S. M.; Wells, D. M.; Albrecht-Schmitt, T. E. *Inorg.Chem.* **2002**, *41*, 5126. e) Sykora, R. E.; Wells, D. M.; Albrecht-Schmitt, T. E. *Inorg. Chem.* **2002**, *41*, 2304. f) Bean, A. C.; Albrecht-Schmitt, T. E. *J. Solid State Chem*. **2001**, *161*, 416. g) Bean, A. C.; Ruf, M.; Albrecht-Schmitt, T. E. *Inorg. Chem.* **2001**, *40*, 3959. h) Sykora, R. E.; Bean, A. C.; Scott, B. L. Runde, W.; Albrecht-Schmitt, T. E. *J. Solid State Chem.* **2004**, *177*, 725. i) Bean, A. C.; Campana, C. F.; Kwon, O.; Albrecht-Schmitt, T. E. *J. Am. Chem. Soc.* **2001**, *123*, 8806. j) Shvareva, T. Y.; Almond, P. M.; Albrecht-Schmitt, T. E. *J. Solid State Chem.* **2005**, *178*, 499.

2) Nocera, D. G.; Lee, Y. S. *Nat. Mater.* **2005**, *4*, 323.

3) Bray, T. H.; Skanthakumar, S.; Soderholm, L.; Sykora, R. E.; Haire, R. G.; Albrecht-Schmitt, T. E. *J. Solid State Chem.* **2008**, *181(3)*, 493.

4) Bray, T. H.; Sullens, T. A.; Shvareva, T. Y.; Sykora, R. E.; Haire, R. G.; Albrecht-Schmitt, T. E. *J. Solid State Chem.*, **2007**, *180*, 70-74.

5) Locock, A.J., Burns, P.C., *The Canadian Mineralogist* **2005**, *43*, 721-733.

6) Unpublished results.

7) Urbanec, Z.; Mrazek, Z.; Cejka, J. *Thermochimica Acta* **1985**, *93*, 525-528.

8) a) Clearfield, A. *Prog. Inorg. Chem.* **1998**, *47*, 371. b) Clearfield, A. *Curr. Opin. Solid State Mater. Sci.* **2003**, *6*, 495. c) Mao, J.-G. *Coord. Chem. Rev.* **2007**, *251*, 1493.